UC Berkeley
UC Berkeley Electronic Theses and Dissertations

Title

Vehicle Parameter Identification and its Use in Control for Safe Path Following

Permalink

https://escholarship.org/uc/item/95g4f274

Author

HONG, SANGHYUN

Publication Date

2014

Peer reviewed|Thesis/dissertation

Vehicle Parameter Identification and its Use in Control for Safe Path Following

by

Sanghyun Hong

A dissertation submitted in partial satisfaction of the
requirements for the degree of
Doctor of Philosophy

in

Engineering – Mechanical Engineering

in the

Graduate Division

of the

University of California, Berkeley

Committee in charge:

Professor John Karl Hedrick, Chair
Professor Francesco Borrelli
Professor Shmuel S. Oren

Spring 2014

Vehicle Parameter Identification and its Use in Control for Safe Path Following

Abstract

Vehicle Parameter Identification and its Use in Control for Safe Path Following

by

Sanghyun Hong

Doctor of Philosophy in Engineering – Mechanical Engineering

University of California, Berkeley

Professor John Karl Hedrick, Chair

This thesis develops vehicle parameter identification algorithms, and applies identified parameters to a controller designed for safe path following.

A tire-road friction coefficient is estimated using an in-tire accelerometer to measure acceleration signals directly from the tires. The proposed algorithm first determines a tire-road contact patch with a radial acceleration profile. The estimation algorithm is based on tire lateral deflections obtained from lateral acceleration measurements only inside the contact patch. A new model is derived for the lateral deflection profiles, which provides robustness to orientation-variation of the accelerometer body frame during tire rotation.

A novel algorithm is developed to identify three inertial parameters: sprung mass, yaw moment of inertia, and longitudinal position of the center of gravity. A correlation of inertial parameters is derived and is used for the identification algorithm. Inertial parameters and vehicle states are simultaneously estimated with a dual unscented Kalman filter based on a nonlinear vehicle model. In order to activate and de-activate different modes of the proposed algorithm, a local observability analysis is performed with the nonlinear vehicle model. The performance and robustness of the proposed approach are demonstrated with extensive CarSim simulations and experimental tests on a flat road with a constant tire-road friction coefficient.

Following a curved road can be dangerous if autonomous vehicles do not take roll motion into consideration. A control algorithm is designed to prevent a dangerous vehicle state induced by roll motion while following a curved road. Roll motion is suppressed throughout cornering with model predictive control. A four-wheel nonlinear vehicle model with roll dynamics and a tire brush model are utilized for the prediction of the vehicle state. An optimal balance in the trade-off between vehicle speed and roll motion is achieved with full braking as a control actuator. Identified vehicle inertial parameters are incorporated into the designed controller. CarSim simulations illustrate the performance of the proposed controller and the effect of the vehicle parameter estimator.

Contents

List of Figures

List of Tables

Acknowledgments

I would like to express heartfelt thanks to my advisor, Prof. J. Karl Hedrick, for his warm guidance, continuous support and encouragement during my doctoral study. Without him, I would not have been able to pursue the doctoral degree. I also express sincere thanks to my co-advisor, Prof. Francesco Borrelli, for his valuable advice and support on my research. In addition, I thank Prof. Andrew Packard and Prof. Fai Ma for serving as committee members in my qualifying examination, and thank Prof. Shmuel S. Oren for serving as a dissertation committee member and a qualifying examination committee member.

I am thankful to all of my friends and colleagues in the Vehicle Dynamics & Control Laboratory and the Model Predictive Control Laboratory. They have provided great opportunities to discuss academic thoughts and share joy in Berkeley life. I also express my gratitude to the *National Science Foundation*, the *Tyre Systems & Vehicle Dynamics Division of Pirelli Tyres SpA*, the *Research and Innovation Center of Ford Motor Company*, and the *Hyundai-Kia Motor Company* for their support of my research.

I owe special thanks to my parents who have been supportive of my doctoral study. I also deeply thank my wife, Seo Hee Kang, for being my pillar that encourages me to overcome hardships.

Chapter 1

Introduction

1.1 Safety of Passenger Vehicles

Vehicle control systems have been an important research subject for enhancing safety and comfort over the last few decades. Active safety systems, such as electronic yaw stability control, adaptive cruise control, and lane-keeping systems, are designed for driving more comfortably and safely. Furthermore, much attention has been paid to (semi-)autonomous vehicles as future technologies which plan a path to a destination and follow the planned path automatically.

Active safety systems and (semi-)autonomous vehicles use various vehicle parameters, e.g. a tire-road friction coefficient, a sprung mass, position of the center of gravity (CoG), and yaw moment of inertia, to produce control signals. Most of vehicle control systems, however, assume vehicle parameters to be fixed. If vehicle parameters were identified accurately, the performance of vehicle control systems could be improved.

Roll motion of vehicles has a significant influence on the safety of occupants. According to the National Highway Traffic Safety Administration (NHTSA), in the United States (US), 34.7 % of the total fatalities were due to rollover accidents in 2011, although the rollover accidents constituted only 2.1 % of all vehicles involved in crashes [1]. In addition, it is startling that 38.5 % of occupants killed by rollover were driving passenger cars. In order to reduce fatalities, roll dynamics should be taken into consideration in vehicle control systems. Particularly, lane-keeping systems and (semi-)autonomous vehicles need to consider roll dynamics to safely travel on a curved road.

1.2 Vehicle Parameter Identification

1.2.1 Tire-Road Friction Coefficient

Tire forces generated between tires and a road are necessary to maintain stability and controllability of vehicle dynamic motion. A tire-road friction coefficient accounts for the maximal

tire forces available to control vehicle motion. Therefore, the estimation of a tire-road friction coefficient is of fundamental importance in vehicle control systems.

Many of the existing estimation algorithms are based on measurements from vehicle sensors, such as a yaw rate sensor and wheel speed sensors. Furthermore, they need unsteady state driving conditions, e.g. acceleration or deceleration, to estimate a friction coefficient [23, 24, 35, 38, 43, 55], and hence a tire-road friction coefficient cannot be estimated under steady state driving conditions, e.g. traveling ahead at a constant vehicle speed.

Lateral deflection of a tire results from tire lateral forces generated by steering. If an estimation algorithm uses the lateral deflection, a tire-road friction coefficient can be identified without acceleration and deceleration. This approach has been applied to the tire-road friction coefficient estimation, and the potential is demonstrated with finite element model (FEM) simulations in [18].

This thesis extends the lateral deflection-based framework to identify the tire-road friction coefficient with a test vehicle in steady state driving. The lateral deflection is obtained with the double integration of lateral acceleration measured by an in-tire 3D wireless accelerometer, as proposed in [8, 10, 11, 46, 47].

1.2.2 Inertial Parameters

Vehicle control systems, e.g. active safety systems and (semi-)autonomous vehicles, compute control signals based on vehicle models, and therefore the closed-loop behavior depends on vehicle inertial parameters, such as a sprung mass, moment of inertia, and position of the center of gravity (CoG). Most vehicle control systems use robust control strategies with constant vehicle inertial parameters assumed [14]. Vehicle inertial parameters, however, vary under different driving conditions, e.g. the number of passengers and seating arrangement.

A variety of approaches have been applied to identify vehicle inertial parameters. Bae et al. [5], Winstead et al. [54], and Vahidi et al. [51] identify a vehicle mass and road grade based on vehicle longitudinal dynamics. Fathy et al. [20] also uses a vehicle longitudinal model to identify a vehicle mass. Bruyne et al. [14], Zarringhalam et al. [58], and Rajamani et al. [41] estimate a vehicle mass, moment of inertia and the CoG position with vehicle vertical dynamics. Wenzel et al. [53] and Best et al. [7] use lateral/yaw dynamics to identify a vehicle sprung mass, yaw moment of inertia, and position of the CoG. Hong and Smith et al. [32] also identify a sprung mass and yaw moment of inertia based on lateral/yaw dynamics.

Yaw moment of inertia has been identified in fewer studies. Bruyne et al. [14] identifies yaw moment of inertia with a test rig, where suspension displacement sensors are assumed to be available. Wenzel et al. [53] and Hong and Smith et al. [32] use a four-wheel vehicle model for the estimation of yaw moment of inertia, and the algorithm is tested with simulations under a single driving condition. Best et al. [7] identifies yaw moment of inertia based on a simple bicycle model, and validates experimentally under a single driving condition.

Inertial parameters are correlated each other. If additional masses, such as passengers and luggage, are loaded on a vehicle, the position of the CoG is changed. Then, the yaw

moment of inertia is also changed as a result of the changed sprung mass and position of the CoG. Most existing algorithms, however, identify the inertial parameters individually without taking the correlation into consideration.

This thesis presents a novel approach to identify a vehicle sprung mass, position of the CoG, and yaw moment of inertia under different driving conditions. A correlation of inertial parameters is applied to the identification algorithm using measurements from commonly used vehicle sensors.

1.3   Path Following of an Autonomous Vehicle

Unintentional lane departure is dangerous for passengers while traveling on a freeway. Lane keeping systems [13, 36] and (semi-)autonomous vehicles [2, 3, 19, 37, 22] provide a vehicle with control signals so that the vehicle can stay within a lane while following a planned path. When following a curved path, roll motion is generated due to vehicle lateral acceleration. However, most vehicle control systems for path-following do not take roll dynamics into consideration.

Roll motion alters contact conditions between rubber tires and a road. Tire lateral forces that enable a vehicle to corner are influenced by the change of tire-road contact conditions. A suspension is designed to generate camber angles when it is vertically displaced due to roll motion. The changed contact conditions can be compensated for with tire lateral forces which are induced by the camber angles [40, 42]. Nevertheless, an aim of suspension designers is to suppress roll motion [42].

Various control strategies have been proposed to prevent extreme roll motion, i.e. rollover. Roll angle is constrained with lower and upper bounds, and control signals are fed into a vehicle only if the roll angle violates the bounded constraints [9, 12, 48, 49, 50, 57]. That is, the rollover prevention controllers are activated only when rollover is imminent.

Many rollover prevention controllers have used differential braking as a control actuator [9, 12, 48, 50, 56]. In order to prevent rollover, differential braking forces a vehicle into understeer by producing yaw moment. Although the understeer is effective in preventing rollover, it is unfavorable in achieving yaw rate required to follow a curved road [12]. This causes a vehicle to deviate from a planned path [48].

This thesis designs an optimal controller to follow a curved path while simultaneously preventing rollover, and the controller is incorporated with the vehicle parameter identification algorithm.

1.4   Contribution and Outlines

In Chapter 2, an estimation algorithm for a tire-road friction coefficient is developed based on tire lateral deflections and an in-tire 3D wireless accelerometer. The estimation algorithm:

- Proposes a method to determine the tire-road contact patch with radial acceleration measurements, which is used to extract lateral acceleration only inside the contact patch.

- Presents lateral deflection models corresponding to the lateral deflections obtained from the lateral acceleration only inside the contact patch.

- Involves vehicle steering in the estimation to achieve consistency of estimation results under large steering maneuvers.

- Validates experimentally the effectiveness and performance of the proposed algorithm with small and large tire slip angles on icy, snowy, and asphalt roads.

In Chapter 3, vehicle inertial parameters, including a vehicle sprung mass, longitudinal position of the CoG, and yaw moment of inertia, are identified with a novel algorithm. The identification algorithm:

- Performs a local observability analysis for vehicle inertial parameters with a four-wheel nonlinear vehicle model. Most existing algorithms have identified the inertial parameters without demonstrating the observability of inertial parameters.

- Determines a vehicle sprung mass m_s by estimating an additional mass m_a, such as passengers and luggage.

- Reduces the complexity of the algorithm by deriving yaw moment of inertia I_z as a function of m_a and l_f.

- Applies a dual unscented Kalman filter framework to estimate simultaneously the inertial parameters and the vehicle state variables.

- Illustrates the capability of the algorithm to differentiate two driving conditions with extensive simulations and experiments.

In Chapter 4, an optimal controller is designed for safe path following of autonomous vehicles. The controller seeks to follow a curved path while simultaneously preventing rollover. The optimal controller:

- Utilizes a receding horizon optimal control technique to minimize the roll motion throughout cornering, which is more aggressive than other rollover prevention controllers which take an action only when rollover is imminent.

- Provides control signals with full braking rather than differential braking since differential braking impedes following a curved path.

- Suppresses excessive reduction of vehicle speed to avoid rear-end collisions by cars following on a freeway.

- Incorporates the vehicle inertial parameter and state estimation algorithm into computing control actions.

- Verifies the performance of the proposed control algorithm with extensive simulations.

Chapter 2

Estimation of Tire-Road Friction Coefficient using Lateral Deflection and a Tire sensor

2.1 Introduction

This thesis develops an algorithm to estimate a tire-road friction coefficient in steady state driving conditions. The algorithm to be proposed is based on an in-tire 3D accelerometer [8, 10, 11, 46, 47] and tire lateral deflection [16]. A tire lateral axis is perpendicular to the wheel vertical plane on which a tire longitudinal axis lies. The fact that a tire has small stiffness in the lateral direction is the basis for the proposed approach.

The potential of the proposed approach is demonstrated in [18] with Finite Element Model (FEM) simulations. This thesis modifies the algorithm proposed in [18] in order to estimate the tire-road friction coefficient with measurements from wireless 3D accelerometers in a test vehicle. The tire-road contact patch is first determined, which is used to extract acceleration measurements only inside the contact patch. A lateral deflection profile is obtained with the lateral acceleration measurements inside the contact patch. Lateral deflection models are derived to describe the lateral deflection profiles. The proposed algorithm is experimentally validated with small and large tire slip angles on icy, snowy, and asphalt roads. Note that the contents of this chapter have been published in [29, 31].

2.2 Lateral Deflection-based Framework for Tire-Road Friction Coefficient Estimation

The new algorithm for the tire-road friction coefficient estimation builds on the lateral deflection-based framework proposed in [18]. The main steps of the lateral deflection-based framework is listed in the following Table 2.1.

Table 2.1: Lateral Deflection-based Framework [31] ©2013 Taylor & Francis

---

Input: Lateral acceleration during tire rotation
Output: Tire-road friction coefficient μ
Begin
  1: De-trend the lateral acceleration profile by subtracting its mean value.
  2: Double integrate the lateral acceleration profile to obtain
     the lateral deflection profile.
  3: Estimate α $(:= -\frac{F_y}{2c_{bend}})$ and β $(:= \frac{M_z}{c_{yaw}})$ of a parabolic lateral-
     deflection model $y = \alpha x^2 + \beta x + \gamma$ in [40] by using a curve-fitting technique,
     where y is the lateral deflection and x is the coordinates in the tire-
     longitudinal direction.
  4: Estimate the lateral force F_y and the aligning moment M_z:
     $F_y = -2c_{bend}\alpha$, $M_z = c_{yaw}\beta$,
     where the stiffness parameters c_{bend} and c_{yaw} are assumed to be known.
  5: Estimate the tire-road friction coefficient μ by using a tire brush model
     and the estimated F_y and M_z.
End

Although the basic approach of the algorithm in [18], including the use of simple physics-based models and measured lateral acceleration, is maintained, the new algorithm uses the different lateral deflection model, acceleration signals and estimation techniques. These changes to be proposed are fundamental in order to apply the lateral deflection-based friction coefficient estimation algorithm to experimental tests. In particular, the new algorithm first determines the tire-road contact patch with radial accelerations. Then, it uses the lateral acceleration profile only inside the contact patch, which ensures robustness to orientation-variation of accelerometer body frame. Using the lateral acceleration only inside the contact patch requires a new form of lateral deflection model to be derived. All the steps are detailed in the subsequent sections.

2.3   Determination of Tire-Road Contact Patch

A tire interacts with a road through the tire-road contact patch. The tire-road contact patch is defined as the region of a tire that contacts with a road [42]. In this section, a radial acceleration profile is used to determine the tire-road contact patch. The approach to be proposed is different than those proposed in [8, 46, 59] that utilize zero, maximum and minimum radial acceleration values.

The contact patch of a tire circumferential center line is identified by locating the leading and trailing edges, as shown in Fig. 2.1. The leading and trailing edges are the foremost

and rearmost edges of the contact patch, respectively. A side view of a Simple Tire Model
(STM) is shown in Fig. 2.1, which provides the theoretical basis to locate the leading and
trailing edges. The accelerometers at two different time instants are indicated as dots. An
angular position θ starts from the top of the tire, whereas another angular position ϕ starts
from the center of the contact patch; $\theta = \pi - \phi$.
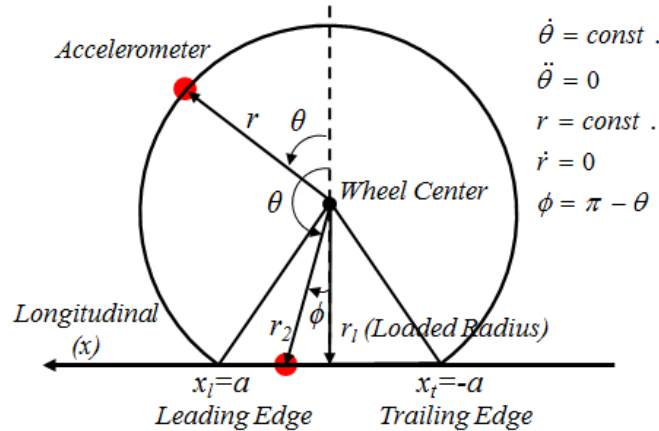
Figure 2.1: Simple Tire Model (STM) [31] ©2013 Taylor & Francis

The simple tire model is constructed based on the following assumptions:

Assumption 1 *On the circumferential line, the deformation of a tire material element does
not affect a neighboring material element. As a result, the simple tire model has sharp corners
at both the leading x_l and trailing x_t edges. In addition, the simple tire model is in a perfect
circular shape with a constant radius r outside the contact patch.*

Assumption 2 *The accelerometer, attached on the center line of the tire inner liner, re-
volves around the wheel-center at a constant angular velocity $\dot{\theta}$.*

Based on the simple tire model with the above assumptions, the kinematics of the ac-
celerometer is investigated to determine the contact patch. The radial acceleration outside
the contact patch is expressed as $\ddot{r} - r\dot{\theta}^2$, which is the radial component of $\ddot{\vec{r}} = \frac{d^2(r\vec{e}_r)}{dt^2} =
(\ddot{r} - r\dot{\theta}^2)\vec{e}_r + (r\ddot{\theta} + 2\dot{r}\dot{\theta})\vec{e}_\theta$, where $\vec{e}_r$ and $\vec{e}_\theta$ are the unit vectors in the radial and tangential di-
rections, respectively. Due to the assumption of the constant radius r, the radial acceleration
outside the contact patch $a_{r,o}$ becomes the centripetal acceleration:

$$a_{r,o} = -r\dot{\theta}^2. \tag{2.1}$$

As shown in Fig. 2.1, the radius inside the contact patch r_2 is a function of the angular
position θ: $r_2 = -r_l \sec\theta$, where r_l is a constant loaded radius of the tire, i.e. distance
between the wheel-center and the center of the contact patch. The radial acceleration inside

the contact patch $a_{r,i}$ is the radial component of the second derivative of $\vec{r_2} = r_2\vec{e_r}$, i.e.
$\ddot{\vec{r_2}} = (\ddot{r_2} - r_2\dot{\theta}^2)\vec{e_r} + (r_2\ddot{\theta} + 2\dot{r_2}\dot{\theta})\vec{e_\theta}$. Since $\ddot{r_2} = -r_l\dot{\theta}^2 \sec\theta(\tan^2\theta + \sec^2\theta)$, the radial acceleration
inside the contact patch $a_{r,i}$ is:

$$a_{r,i} = -2r_l\dot{\theta}^2 \sec\theta\tan^2\theta. \tag{2.2}$$

The accelerations, $a_{r,o}$ in (2.1) and $a_{r,i}$ in (2.2), are drawn against the angular position θ
ranging from 0° through 360° in Fig. 2.2. The radial acceleration in Fig. 2.2 is drawn with a
simulation where the angular velocity $\dot{\theta}$ is 33.9685 rad/s, the angular position at the leading
edge ϕ_l is 15°, the unloaded radius r is 0.3322 m, and the loaded radius r_l is 0.3222 m.
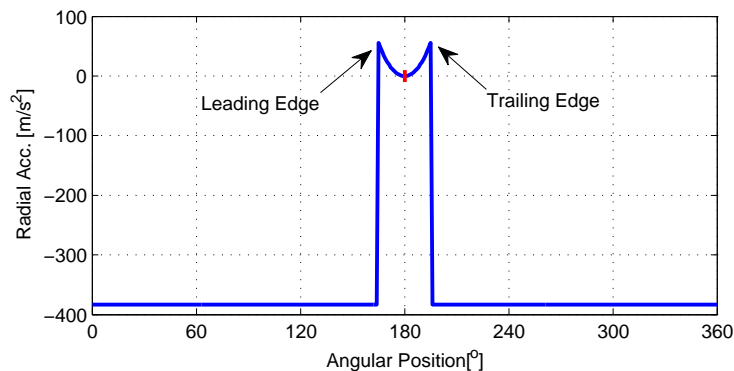
Figure 2.2: [STM] Radial Acceleration from STM [31] ©2013 Taylor & Francis

Note that the radial acceleration has abrupt changes at the leading and trailing edges,
and also has a convex shape inside the contact patch, as shown in Fig. 2.2. The convex
shape is also observed in the radial acceleration profiles collected from the experiments, as
shown in Fig. 2.3. A set of measured radial acceleration profiles are presented in Fig. 2.3
(details of the experimental set-up will be explained later). Since the assumptions in the
STM do not hold in a real tire, the experimental radial acceleration profiles are not identical
to those in Fig. 2.2. Nevertheless, the abrupt changes in the radial acceleration occur at the
leading and trailing edges.

The abrupt changes observed in Fig. 2.2 and Fig. 2.3 implies that the derivative of the
radial acceleration, i.e. radial jerk, has two large absolute values at the leading and trailing
edges. Therefore, the contact patch is determined by locating the two large absolute values
in the derivative of the radial acceleration. A simulation result of a tire Finite Element Model
(FEM) is presented in Fig. 2.4. The solid line in Fig. 2.4a represents the radial acceleration
profile, and the dashed line in Fig. 2.4b represents the magnitude of the derivative. The
leading and trailing edges are located by the positions of the two peaks in Fig. 2.4b.

In the tire FEM simulations, a tire rolls freely on a flat road surface with a given tire slip
angle. For the sake of brevity, the most important features of the tire FEM are only presented
as follows (all details on the tire FEM can be found in [18]). The tire FEM is constructed
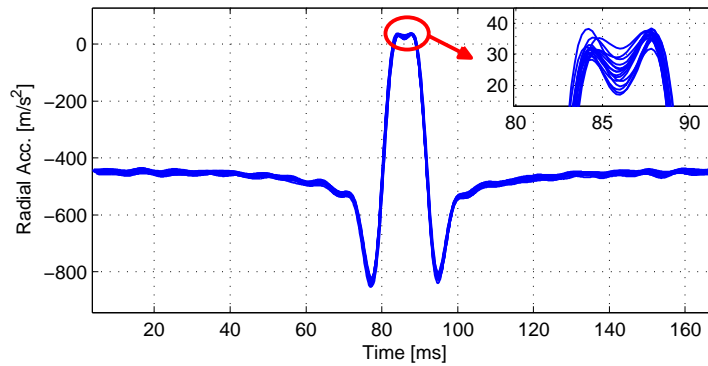
Figure 2.3: [Exp.] Radial Acceleration from an Experiment [31] ©2013 Taylor & Francis
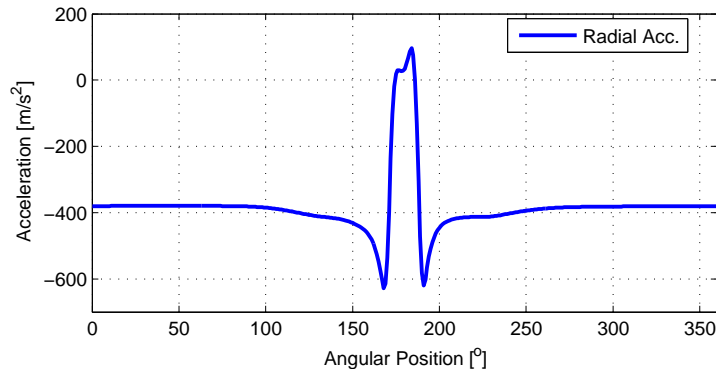
(a) Radial Acceleration
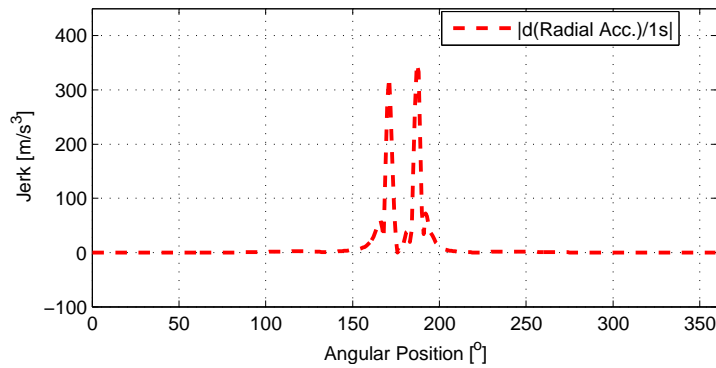
(b) Magnitude of Derivative of Radial Acceleration

Figure 2.4: [FEM] Radial Acceleration and Magnitude of its Derivative [31] ©2013 Taylor &
Francis

with a rubber body, an inner-liner, two layers of belts and a rigid bead. The geometry
of all the tire components is symmetric with respect to the wheel vertical plane. The tire

body is modeled with the rubber materials that have both hyperelastic and viscoelastic characteristics. The rolling on a flat road surface, the tire inflation, the tire normal load, and the translational velocity are all the same as those in [18]. One difference is that the mesh is uniformly distributed every one degree throughout the tire circumference as shown in Fig. 2.5a, whereas the tire FEM in [18] uses the reduced mesh density in the upper half of the tire. The uniform mesh density facilitates in building a more realistic set-up for the accelerometer with a constant sampling frequency.

It should be noted that the radial jerk is used to estimate the contact patch rather than the radial acceleration itself. If the assumptions of the STM do not hold, the two peaks in Fig. 2.2 might not be clearly observed, and therefore the localization of them might not be easy as shown in Fig. 2.4a. In the magnitude of the radial jerk, however, the two peaks are clearly identifiable as shown in Fig. 2.4b.

Table 2.2: Angular Positions θ at Leading and Trailing Edges [31] ©2013 Taylor & Francis

Normal Force [N]	Leading Edge (Proposed/Pressure)	Trailing Edge (Proposed/Pressure)
3800	$173^o/172^o$	$187^o/188^o$
4500	$172^o/171^o$	$188^o/189^o$
6000	$170^o/169^o$	$191^o/192^o$

As presented in Table 2.2, the effectiveness of the proposed methodology is demonstrated through the tire FEM simulations. The leading and trailing edges are estimated by two different approaches. One is the proposed approach, and the other one is an approach to use contact pressures on elements of the tire FEM. The contact pressure values are reported from the FEM simulation software. The angular positions, θ, corresponding to the estimated leading and trailing edges are presented in Table 2.2.

2.4   Orientation-Variation of Accelerometer Body Frame

The lateral acceleration profile is integrated twice to obtain the lateral deflection profile. As a tire rotates, however, the lateral axis of the accelerometer body frame is not always pointed at the actual lateral direction that is perpendicular to the wheel vertical plane. Therefore, the measured lateral acceleration is different from the actual lateral acceleration, which violates the assumption in [18].

Fig. 2.5b presents a lateral deflection profile from the bottom view of the tire FEM in Fig. 2.5a. The translational velocity of the tire FEM is indicated as V, and the tire slip angle is $\alpha = 2.0^o$. The angular position in Fig. 2.5b starts from the top position of the tire and ends at the same top position. The accelerometer in Fig. 2.5a follows the tire circumferential

(a) Tire FEM

(b) Lateral Deflection
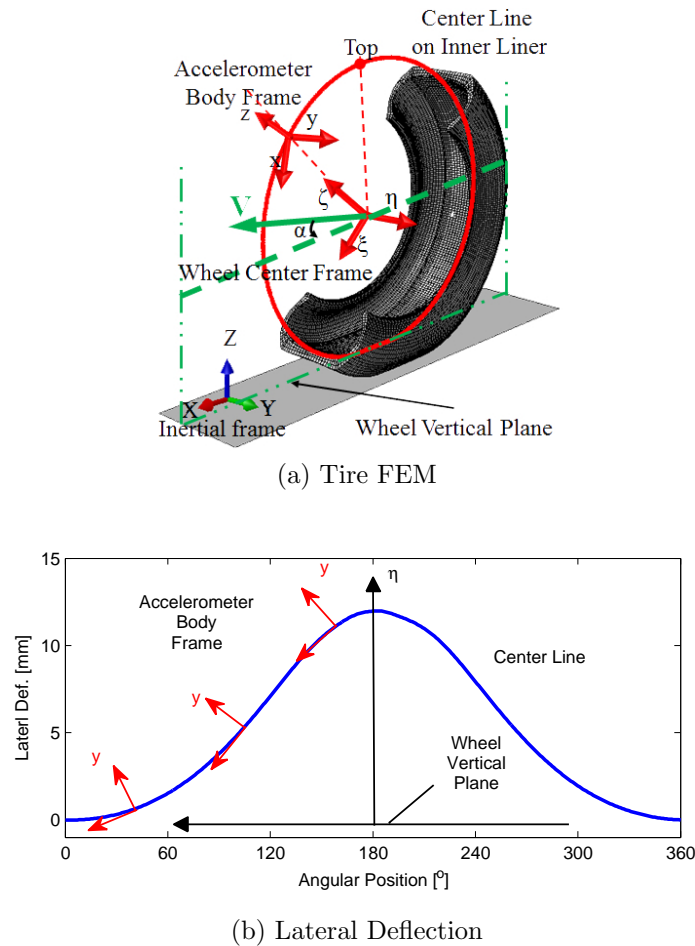
Figure 2.5: Orientation-Variation of Accelerometer Body Frame [31] ©2013 Taylor & Francis

inner center line as the tire rotates. If the tire is steered and have the tire slip angle α, a friction force is generated inside the contact patch. Then, the tire deforms in the direction of the friction force vector, and the tire inner center line also deforms in the same direction. Consequently, the orientation of the accelerometer body frame continues to vary while the accelerometer follows the deformed circumferential inner center line. As shown in Fig. 2.5b, the lateral axis (y) of the accelerometer body frame is not parallel to the actual lateral axis (η) which is perpendicular to the wheel vertical plane. Note that the orientation-variation of the accelerometer body frame occurs in the entire 3D space, although Fig. 2.5b only presents the bottom view.

Due to the orientation-variation, the accelerometer does not measure the actual lateral acceleration that is necessary for the lateral deflection-based framework in Table 2.1. Two lateral acceleration profiles of the tire FEM are presented in Fig. 2.6a, where L indicates the leading edge and T indicates the trailing edge. The dashed line represents the acceleration profile measured by the lateral axis of the wheel-center frame, η-axis in Fig. 2.5, whereas
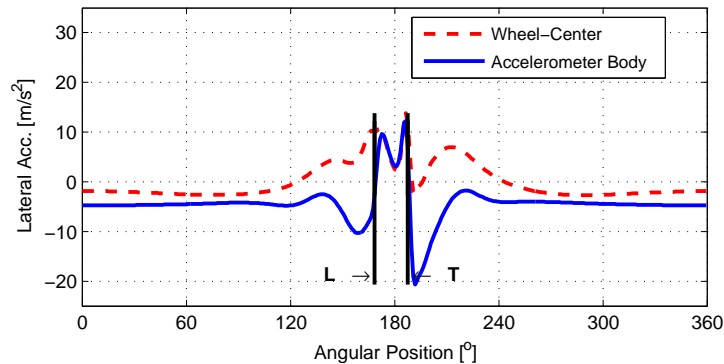
(a) [FEM] Lateral Acceleration with respect to Wheel-Center and Accelerometer Body Frames
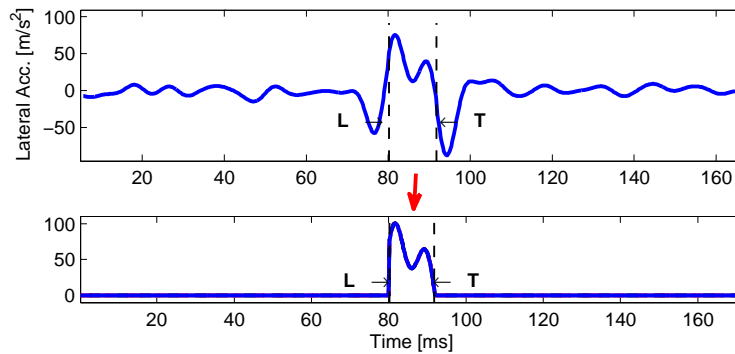
(b) [Exp.] Lateral Acceleration Inside Contact Patch

Figure 2.6: Lateral Acceleration [31] ©2013 Taylor & Francis

the solid line represents that measured by the lateral axis of the accelerometer body frame, y-axis in Fig. 2.5. The wheel-center frame rotates with its lateral axis η pointed at the direction perpendicular to the wheel vertical plane, i.e. actual lateral direction. The lateral acceleration measured by the accelerometer, solid line, is different from the actual one, dashed line, as shown in Fig. 2.6a.

However, the orientation-variation of the accelerometer body frame is negligible inside the contact patch. There is little discrepancy between two lateral acceleration profiles inside the contact patch, as shown in Fig. 2.6a.

Therefore, the new tire-road friction coefficient estimation algorithm uses the lateral acceleration profile only inside the contact patch. Once the contact patch is determined with the methodology proposed in the previous section, the lateral accelerations outside the contact patch are set to zero, as shown in Fig. 2.6b and Fig. 2.7a. Then, the lateral deflection is obtained through the double integration of the lateral acceleration only inside the contact patch, as shown in Fig. 2.7. Note that the mean value of the lateral acceleration is not subtracted before the double integration, which is different from the framework of
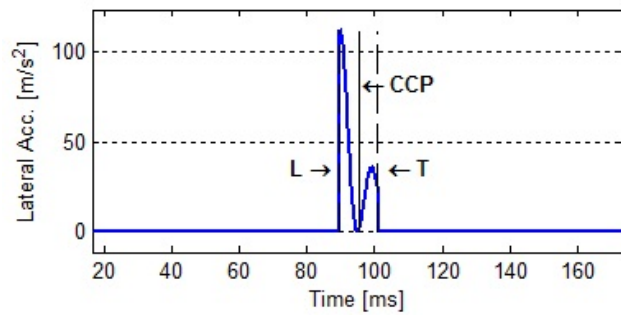
(a) Lateral Acceleration Inside Contact Patch
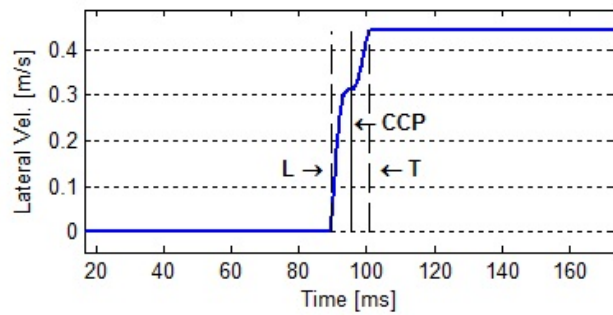
(b) Integration
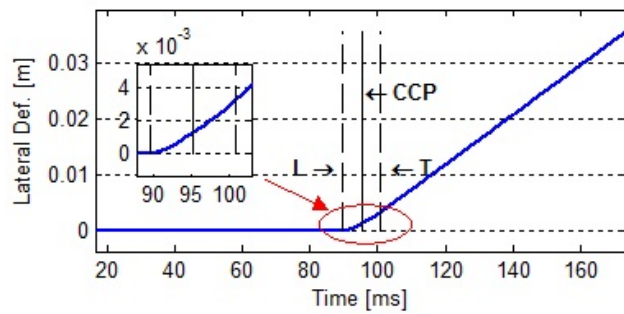
(c) Double Integration

Figure 2.7: Integrations of Lateral Acceleration [29] ©2013 IEEE

Table 2.1 proposed in [18].

2.5 New Form of Lateral Deflection Model

The lateral deflection of the inner center line has been modeled as a parabolic polynomial in [40] as follows:

$$y = \alpha x^2 + \beta x + \gamma, \quad \left(\alpha := -\frac{F_y}{2c_{bend}}, \ \beta := \frac{M_z}{c_{yaw}}, \ \gamma := \frac{F_y}{c_{lat}} \right), \tag{2.3}$$

where x indicates the coordinate value in the tire longitudinal direction and y indicates the coordinate value in the tire lateral direction, as shown in Fig. 2.8. This model, however, should be modified since only the lateral acceleration inside the contact patch will be used to estimate the tire-road friction coefficient.
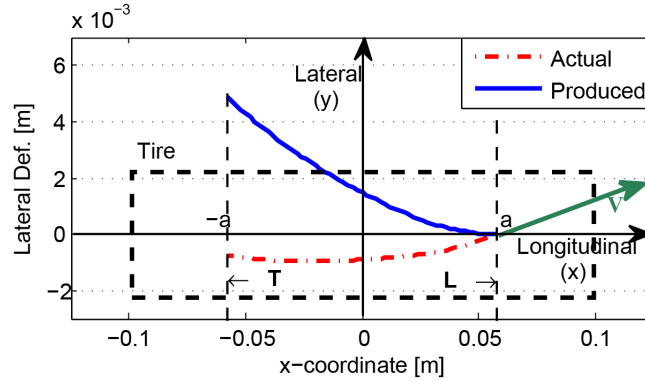
Figure 2.8: [Exp.] Produced Lateral Deflection Inside Contact Patch [31] ©2013 Taylor & Francis

2.5.1 Lateral Deflection Produced by Lateral Acceleration Only Inside Contact Patch

The dashed-dotted line in Fig. 2.8 represents an actual lateral deflection, which can be obtained from the lateral acceleration measured with *no* orientation-variation of the accelerometer body frame. The solid line in Fig. 2.8 represents the lateral deflection produced by the lateral acceleration only inside the contact patch. The difference between the dashed-dotted line and the solid line results from the zero lateral acceleration outside the contact patch and zero boundary conditions for double integration at the leading edge (time $t = t_l$), i.e. zero lateral velocity $v_y(t_l) = 0$ and zero lateral deflection $y_l = 0$.

The key idea for the modification of (2.3) is to take double integration of the lateral acceleration model. The lateral acceleration is expressed as a differential form of the parabolic lateral deflection model, i.e. the double derivative of (2.3):

$$\frac{d^2y}{dt^2} = 2\alpha \left(\frac{dx}{dt} \right)^2 + (2\alpha x + \beta) \frac{d^2x}{dt^2} \tag{2.4}$$

2.5.2 Classification of Lateral Acceleration Profiles

If the lateral acceleration is measured on a high friction road, e.g. asphalt road, it will be handled differently for double integration than that on a low friction road, e.g. icy road. In order to classify roughly whether or not the lateral acceleration is measured on a road with high friction coefficient, simple criteria are established in this section.

2.5.2.1 Compressive Lateral Deflection

The criteria are based on the observation that a small lateral deflection is produced inside the contact patch even at a zero tire slip angle. Fig. 2.9a presents the lateral deflections from bottom view of the tire FEM with different friction coefficient μ and tire slip angle α conditions. The changes of the lateral deflections at different friction coefficient and tire slip angle conditions have also been experimentally validated in [16]. The contact patches of the lateral deflections in Fig. 2.9a are magnified in Fig. 2.9b, Fig. 2.9c, and Fig. 2.9d, respectively.

(a) Lateral Deflections

(b) Friction CoefficFent μ: 0.1, Tire Slip Angle α: 0.0^o

(c) Friction Coefficient μ: 0.1, Tire Slip Angle α: 2.0^o(d) Friction Coefficient μ: 0.9, Tire Slip Angle α: 2.0^o
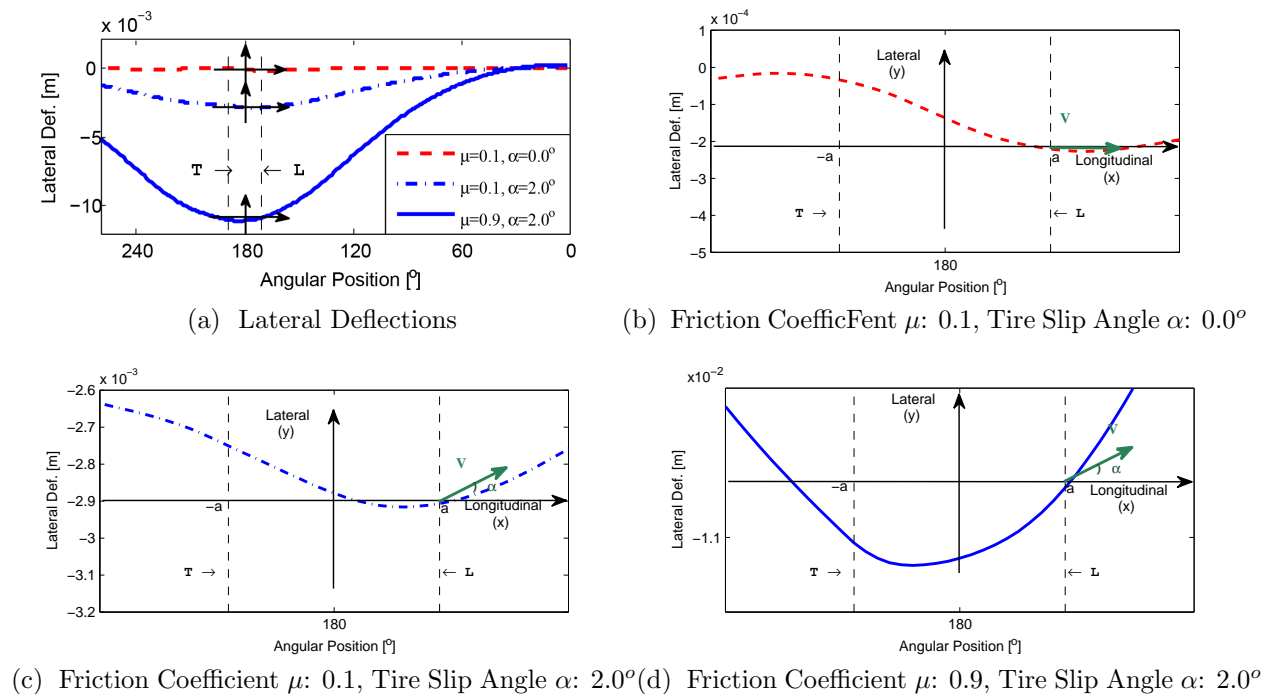
Figure 2.9: [FEM] Lateral Deflections by Compressive Force and Friction Force [31] ©2013 Taylor & Francis

As shown in Fig. 2.9b, the lateral deflection profile at a zero tire slip angle is a curve rather than a straight line parallel to the longitudinal axis, which results from the tire vertical deflection. Due to the normal load, the tire deforms vertically, and, as a result, a compressive force is generated inside the contact patch [33]. The small lateral deflection inside the contact

patch even at the zero tire slip angle is attributed to the compressive force. Note that this
kind of lateral deflection is different from the lateral deflection created by the friction force
at a non-zero tire slip angle.

Many tire properties can affect the lateral deflection induced by the compressive force
inside the contact patch. For instance, tire manufacturing elements, such as a radial body
ply and a bias ply, affect the tire vertical stiffness, and can also result in the anisotropic
characteristics of the stiffness. Different tire tread designs lead to different lateral deflections
at the zero tire slip angle. Furthermore, the hyperelasticity of the tire rubber body has
a significant influence on the compressive lateral deflection. The hyperelasticity prevents
the tire circumferential line from being compressed axially, and therefore the center line is
shaped into a curve by the compressive force.

The compressive component of the lateral deflection provides a clue to establish the
criteria for the rough classification of the lateral accelerations. On a low friction road, e.g.
icy road, the lateral deflection by the compressive force still remains dominantly even at a
non-zero tire slip angle as shown in Fig. 2.9c, in which the dashed-dotted line represents the
lateral deflection profile of the tire FEM at the tire slip angle $\alpha = 2.0^o$ on a road with the
friction coefficient $\mu = 0.1$. However, on a high friction road, e.g. asphalt, the compressive
lateral deflection component vanishes, whereas the frictional lateral deflection component
is dominant as shown in Fig. 2.9d, in which the solid line represents the lateral deflection
profile at the tire slip angle $\alpha = 2.0^o$ on a road with the friction coefficient $\mu = 0.9$.

Therefore, the lateral accelerations will be classified into two categories:

Category 1 - lateral accelerations *without* compressive lateral deflection component

Category 2 - lateral accelerations *with* compressive lateral deflection component.

2.5.2.2   Lateral Acceleration on a Road with a High Friction

The reason for classifying the lateral accelerations (rather than deflection) is that the lateral
acceleration in the category 1 might include a random and persistent acceleration. The lat-
eral accelerations only inside the contact patch, which are experimentally measured on an
asphalt road, are presented in Fig. 2.10. As shown in Fig. 2.10, all the lateral acceleration
profiles have similar dominant curves. However, those are shifted by random and constant
accelerations; the shifts are exaggerated for visibility. It is presumed that the random and
constant shifting is a consequence of the tire deformation; this phenomenon is under inves-
tigation. The random shift at each tire rotation does not affect the fundamental profile of
the lateral acceleration as shown in Fig. 2.10. However, when taking double integration to
obtain the lateral deflection, the effect of the random shift is amplified, as will be illustrated
in the *Experimental Results* section.
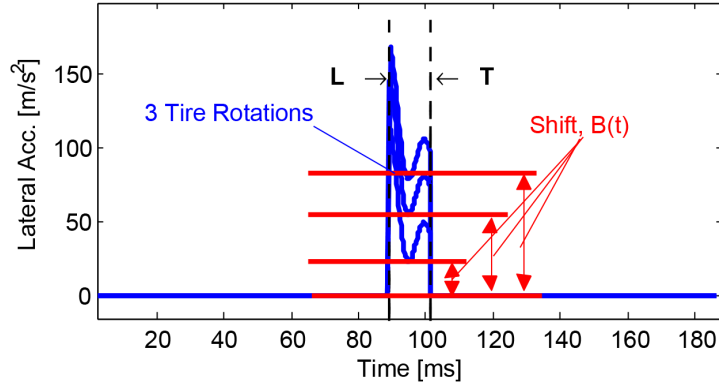
Figure 2.10: [Exp.] Shifted Lateral Accelerations Inside Contact Patch [31] ©2013 Taylor & Francis

2.5.2.3   Criteria for the Classification

The criteria for the classification is established by combining (2.4) with the simple tire model in Fig. 2.1. The longitudinal acceleration inside the contact patch is expressed as $a_x = \frac{d^2 x}{dt^2}$ in (2.4), and it can be approximated as the negated tangential acceleration inside the contact patch, $-a_\theta$, based on the simple tire model (STM) in Fig. 2.1. The tangential acceleration a_θ is the coefficient of $\vec{e}_\theta$ in $\ddot{\vec{r}}_2 = (\ddot{r}_2 - r_2 \dot{\theta}^2)\vec{e}_r + (r_2 \ddot{\theta} + 2\dot{r}_2 \dot{\theta})\vec{e}_\theta$, where $\dot{r}_2 = -r_l \dot{\theta} \sec\theta \tan\theta$ and $\dot{\theta}$ is a constant. Therefore, the longitudinal acceleration a_x is:

$$a_x \approx -a_\theta = 2 r_l \dot{\theta}^2 \sec\theta \tan\theta. \tag{2.5}$$

Note that the longitudinal acceleration is positive and decreases to zero as shown in Fig. 2.11 over the leading region, i.e. from the leading edge to the center of the contact patch: $a \geq x \geq 0$. The longitudinal velocity $v_x = \frac{dx}{dt}$ in (2.4) is also approximated as the negated
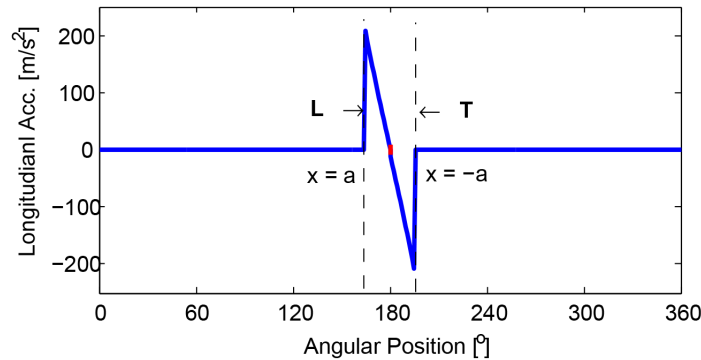
Figure 2.11: [STM] Longitudinal Acceleration ($a_x \approx -a_\theta$) [31] ©2013 Taylor & Francis

tangential velocity v_θ in the STM, which is the coefficient of $\vec{e}_\theta$ in $\dot{\vec{r}}_2 = \dot{r}_2 \vec{e}_r + r_2 \dot{\theta} \vec{e}_\theta$, where

$r_2 = -r_l \sec\theta$ and $\dot\theta$ is a constant. The longitudinal velocity v_x is modeled as:

$$v_x \approx -v_\theta = r_l \dot\theta \sec\theta. \tag{2.6}$$

Substituting (2.5) and (2.6) into (2.4) yields the lateral acceleration model which is a function of the angular position θ and the angular velocity $\dot\theta$. This lateral acceleration model describes the lateral acceleration in category 1. Fig. 2.12 presents the lateral acceleration of
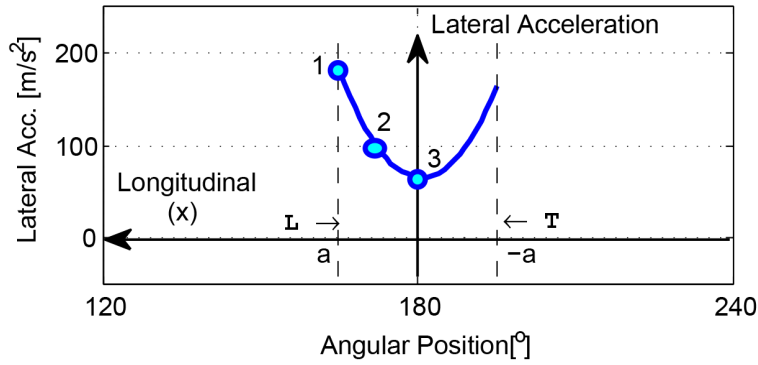
Figure 2.12: Lateral Acceleration corresponding to Lateral Deflection without Component from Compressive Force [31] ©2013 Taylor & Francis

the category 1 that corresponds to the lateral deflection on the negative side of the lateral axis, as the solid line in Fig. 2.9d with no compressive deflection component. Note that both the curvature α and the slope β of the parabolic lateral deflection model in (2.3) have positive signs for the lateral deflection on the negative side of the lateral axis. The lateral acceleration in Fig. 2.12 is a result of the angular velocity $\dot\theta = 33.9685$ rad/s, the angular position at the leading edge $\phi_l = 15^o$, the unloaded radius $r = 0.3322$ m, the loaded radius $r_l = 0.3222$ m, $\alpha = 3$, and $\beta = 0.05$. The lateral acceleration decreases over the leading region, while its maximum value is at the leading edge, as shown in Fig. 2.12.

Fig. 2.12 provides the criteria to classify the lateral accelerations, as listed in Table 2.3, where Acc(k) indicates the lateral acceleration at the kth point in Fig. 2.12. The same criteria in Table 2.3 are applied after inverting the lateral acceleration and deflection profiles, if the lateral deflection is on the positive side of the lateral axis.

2.5.3   A New Form of Lateral Deflection Model

In order to derive the new form of lateral deflection model, the classified lateral accelerations are integrated twice. If the lateral acceleration belongs to category 1, i.e. it corresponds to the lateral deflection without compressive component, the lateral acceleration model is:

$$\frac{d^2 y}{dt^2} = 2\alpha\left(\frac{dx}{dt}\right)^2 + (2\alpha x + \beta)\frac{d^2 x}{dt^2} + B(t). \tag{2.7}$$

Table 2.3: Classification of Lateral Acceleration [31] ©2013 Taylor & Francis

---

If
  $\text{Acc}(1) > \text{Acc}(2) > \text{Acc}(3)$ AND $\text{Mean}(\text{Acc}(2) : \text{Acc}(3)) > 0$
Then
  Category 1: Lateral acceleration corresponding to lateral deflection
  without deflection component from compressive force
Else
  Category 2: Lateral acceleration corresponding to lateral deflection
  with deflection component from compressive force
End

Note that the random shift in the lateral acceleration is expressed as the shift term $B(t)$, which is assumed to be a constant value B.

The term B is a random constant number, and therefore it should be removed. The longitudinal acceleration at the center of the contact patch (time $t = t_c$), i.e. $\frac{d^2x}{dt^2}\big|_{t_c}$, is zero as shown in Fig. 2.11. Therefore, the lateral acceleration at the center of the contact patch is: $\frac{d^2y}{dt^2}\big|_{t_c} = 2\alpha\left(\frac{dx}{dt}\right)_{t_c}^2 + B$. Then, subtracting the lateral acceleration at the center of the contact patch, $\frac{d^2y}{dt^2}\big|_{t_c}$, from (2.7) removes the term B as follows:

$$h(t) := \frac{d^2y}{dt^2} - \frac{d^2y}{dt^2}\bigg|_{t_c} = 2\alpha\left\{\left(\frac{dx}{dt}\right)^2 - \left(\frac{dx}{dt}\right)_{t_c}^2\right\} + (2\alpha x + \beta)\frac{d^2x}{dt^2}. \tag{2.8}$$

The lateral deflection model is derived by taking double integration of (2.8). The integration of $h(t)$ in (2.8) is:

$$\int_{t_l}^{t} h(t)dt := H(t) \tag{2.9}$$

$$= (2\alpha x + \beta)\frac{dx}{dt} - v_y(t_l) - 2\alpha\tau\left(\frac{dx}{dt}\bigg|_{t_c}\right)^2,$$

where $v_y(t_l) = (2\alpha x_l + \beta)\frac{dx}{dt}\big|_{t_l}$, and the double integration of $h(t)$ is:

$$\int_{t_l}^{t} H(t)dt = \alpha(x^2 - x_l^2) + \beta(x - x_l) - (2\alpha x_l + \beta)\tau\frac{dx}{dt}\bigg|_{t_l} - \alpha\tau^2\left(\frac{dx}{dt}\bigg|_{t_c}\right)^2. \tag{2.10}$$

In (2.9) and (2.10), τ denotes the time difference between the leading edge x_l and a position x inside the contact patch, $\tau := t - t_l = \frac{\phi_l - \phi}{\dot{\theta}}$, where $\dot{\theta}$ is the constant angular velocity.

Since the lateral acceleration outside the contact patch is set to zero as shown in Fig. 2.7a, the lateral velocity at the leading edge is zero in Fig 2.7b, i.e. $v_y(t_l) = (2\alpha x_l + \beta)v_x(t_l) = 0$. This implies $2\alpha x_l + \beta = 0$ since the longitudinal velocity at the leading edge $v_x(t_l)$ is not zero. Note that the boundary condition, $v_y(t_l) = (2\alpha x_l + \beta)v_x(t_l) = 0$, is used for the second integration in (2.10). Then, the lateral deflection model is re-written as follows:

$$\iint_{t_l}^{t} \frac{d^2y}{dt^2} - \frac{d^2y}{dt^2}\bigg|_{t_c} dtdt = \alpha\left\{1 - \left(\frac{v_x(t_c)}{\bar{v}_x}\right)^2\right\}(x - x_l)^2, \qquad (2.11)$$

where $v_x(t_c)$ is the longitudinal velocity at the center of the contact patch and $\bar{v}_x$ is the average longitudinal velocity over the contact patch, i.e. $\bar{v}_x = \frac{x - x_l}{\tau}$.

The longitudinal velocity v_x is approximated as the negated tangential velocity, i.e. $v_x \approx -v_\theta = r_l\dot{\theta}\sec\theta$, as discussed previously. When considering $\theta_c = \pi$ at the center of the contact patch, the longitudinal velocity $v_x(t_c)$ is:

$$v_x(t_c) = -r_l\dot{\theta}. \qquad (2.12)$$

Note that the longitudinal speed at the center of the contact patch $|v_x(t_c)|$ is not close to zero, although it is the smallest inside the contact patch. Furthermore, the difference between the longitudinal velocity at the leading edge $v_x(t_l)$ and at the center of the contact patch $v_x(t_c)$ is not large. This is because the coordinate frame in Fig. 2.9 is fixed at the *center of contact patch* and under the *translational* motion in the direction of the velocity V. If the coordinate frame is fixed at the *ground*, $v_x(t_c)$ would be almost zero since the tire material element in the inner center line is close to the instantaneous center of rotation.

Since the difference in $v_x(t)$ over the contact patch is not large, the average longitudinal velocity $\bar{v}_x$ is approximated to be the longitudinal velocity at the leading edge, $\bar{v}_x \approx v_x(t_l)$. Another reason for this approximation is that it is hard to measure $v_x(t)$ throughout the contact patch for calculating the average longitudinal velocity $\bar{v}_x$. Therefore, the average longitudinal velocity $\bar{v}_x$ is:

$$\bar{v}_x = r_l\dot{\theta}\sec\theta_l = -r_l\dot{\theta}\sec\phi_l, \qquad (2.13)$$

where the angular position at the leading edge in the STM is $\theta_l = \pi - \phi_l$. The angular position ϕ starts from the center of the contact patch, and therefore $\phi_l = \sin^{-1}\frac{x_l}{r_{unloaded}}$.

Finally, the model for the lateral deflection with no compressive component is obtained by substituting (2.12) and (2.13) into (2.11) as follows:

$$y = \iint_{t_l}^{t} \frac{d^2y}{dt^2} - \frac{d^2y}{dt^2}\bigg|_{t_c} dtdt = \alpha\left(\frac{x_l}{r_{unloaded}}\right)^2(x - x_l)^2. \qquad (2.14)$$

Note that the lateral acceleration at the center of the contact patch should be subtracted to obtain the lateral deflection profile which is described by the lateral deflection model in (2.14). The model in (2.14) contains the longitudinal coordinate inside the contact patch, x, and the unloaded radius $r_{unloaded}$, which are parameters that can be estimated more

accurately and easily than the longitudinal velocity at the center of the contact patch $v_x(t_c)$ and the average longitudinal velocity $\bar{v}_x$ in (2.11).

On the other hand, in order to derive the model for the lateral deflection with a compressive component, the original lateral acceleration model in (2.4) is integrated twice with the same boundary conditions as follows:

$$y = \iint_{t_l}^{t} \frac{d^2y}{dt^2} dt dt = \alpha(x - x_l)^2. \tag{2.15}$$

2.6   Estimation of Lateral Force and Aligning Moment

The lateral force F_y, included in $\alpha := -\frac{1}{2}\frac{F_y}{c_{bend}}$ in (2.14) and (2.15), is estimated by applying a least squares curve-fitting technique to the lateral deflections. In the curve-fitting technique, the lateral deflection model in (2.14) and (2.15) are used depending on the criteria defined in Table 2.3. Note that the lateral deflection is produced from the lateral acceleration only inside the contact patch. Furthermore, if the lateral acceleration belongs to category 1, the lateral acceleration at the center of the contact patch is subtracted from the original one before double integration.
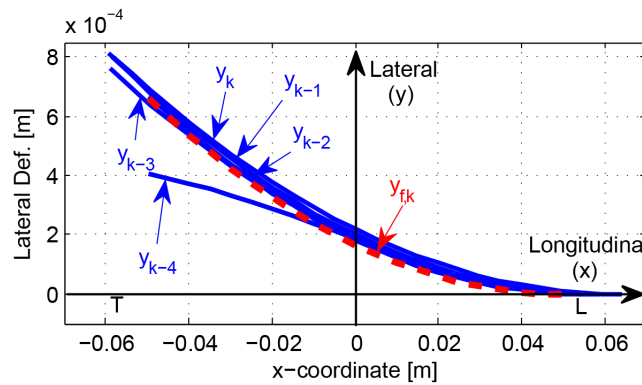
Figure 2.13: [Exp.] Curve-Fitting for α [31] ©2013 Taylor & Francis

In order to reduce a statistical deviation in the lateral force F_y estimates, the lateral deflections for n tire rotations are used for the curve-fitting technique. If $n = 5$, for example, the lateral deflection profiles for $(k-4)^{th}$, ..., k^{th} tire rotations, i.e. solid lines y_{k-4}, ..., y_k in Fig. 2.13, are used in the curve-fitting to estimate α_k for the kth tire rotation. If the lateral acceleration belongs to category 1, α_k is estimated by solving an optimization problem for

the curve-fitting with the model (2.14) as follows:

$$
\alpha_k = arg \min_{\alpha} \left\| \begin{array}{c} \alpha \left(\frac{x_{k,l}}{r_{unloaded}} \right)^2 \left(\left[\begin{array}{c} x_{k,l} \\ \vdots \\ x_{k,t} \end{array} \right] - \underline{1} \cdot x_{k,l} \right)^2 - \left[\begin{array}{c} y_{k,l} \\ \vdots \\ y_{k,t} \end{array} \right] \\ \vdots \\ \alpha \left(\frac{x_{k-n+1,l}}{r_{unloaded}} \right)^2 \left(\left[\begin{array}{c} x_{k-n+1,l} \\ \vdots \\ x_{k-n+1,t} \end{array} \right] - \underline{1} \cdot x_{k-n+1,l} \right)^2 - \left[\begin{array}{c} y_{k-n+1,l} \\ \vdots \\ y_{k-n+1,t} \end{array} \right] \end{array} \right\|^2 , \quad (2.16)
$$

where $x_k = [x_{k,l} \; ; \; \cdots \; ; \; x_{k,t}]$ represents a column vector whose elements are the longitudinal coordinate values from the leading edge $x_{k,l}$ through the trailing edge $x_{k,t}$ for the kth tire rotation and $\underline{1}$ represents a column vector whose elements are one and size is the same as x_k. The square symbol in $\left(\left[\begin{array}{c} x_{k,l} \\ \vdots \\ x_{k,t} \end{array} \right] - \underline{1} \cdot x_{k,l} \right)^2$ refers to the element-wise square. The estimated α_k yields the estimated lateral deflection $y_{f,k}$ for the kth tire rotation, the dashed line in Fig. 2.13, as follows:

$$
y_{f,k} = \alpha_k \left(\frac{x_{k,l}}{r_{unloaded}} \right)^2 \left(\left[\begin{array}{c} x_{k,l} \\ \vdots \\ x_{k,t} \end{array} \right] - \underline{1} \cdot x_{k,l} \right)^2 . \quad (2.17)
$$

The new lateral deflection profile $y_{f,k}$ replaces the original lateral deflection profile y_k so that it can be used for the future curve-fitting at $(k+1)^{th}$, $(k+2)^{th}$, ... tire rotations.

The lateral force F_y is calculated with the estimated α as follows:

$$
F_y = -2\alpha c_{bend}, \quad (2.18)
$$

where c_{bend} is a given bending stiffness.

The aligning moment M_z, which is contained in $\beta := \frac{M_z}{c_{yaw}}$, is not included in the lateral deflection models in (2.14) and (2.15). Therefore, M_z cannot be estimated with the curve-fitting. The aligning moment M_z is estimated using a pneumatic trail. The pneumatic trail t is defined as the relationship between F_y and M_z:

$$
t = -\frac{M_z}{F_y} = \eta x_l, \; (0 \leq \eta \leq 1). \quad (2.19)
$$

This implies that t is the distance between the center of the contact patch and the position where F_y is applied to generate M_z. Therefore, η in (2.19) should be in the range $0 \leq \eta \leq 1$, and it can be any value between 0 and 1 as long as the nonlinear equations to be discussed in

the next section can converge to a solution; η is a tuning parameter in the tire-road friction coefficient estimation algorithm. Then, the aligning moment M_z is estimated as follows:

$$M_z = -\eta x_l F_y. \tag{2.20}$$

2.7 Estimation of Friction Coefficient

The tire-road friction coefficient is estimated through the tire brush model, which correlates the tire-road friction coefficient μ, the tire slip angle α, and the normal force F_z with the lateral force F_y and the aligning moment M_z in [40]. This section introduces the tire brush model briefly, and presents how the friction coefficient μ is estimated.

2.7.1 Tire Brush Model

The tire brush model assumes a tire consists of tread elements, whose tips contact with the road surface inside the tire-road contact patch. The deflection of the tread elements inside the contact patch is described by the tire brush model, as shown in Fig. 2.14.
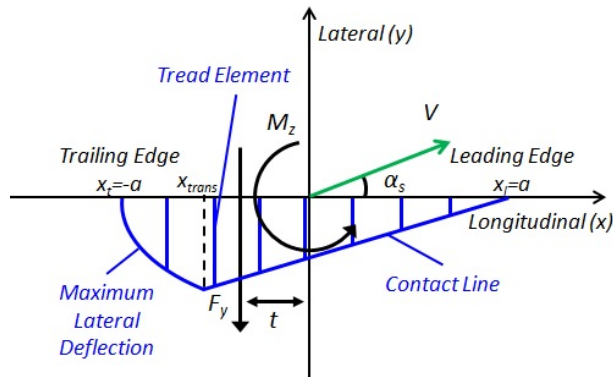
Figure 2.14: Tire Brush Model [29] ©2013 IEEE

If a tire has a tire slip angle α_s between the translational velocity V and the longitudinal (x) axis, the tread elements deform in the lateral (y) direction, as shown in Fig. 2.14. Then, the contact line is drawn by connecting the tip of each tread element. The contact line is parallel to the wheel velocity vector V. As the tire rotates, the tip of the tread element follows the contact line. If the tip of tread element reaches the maximum possible lateral deflection at x_{trans} in Fig. 2.14, it loses adhesion to the ground and starts to slide.

The distance from the leading edge $x_l = a$ to x_{trans} is calculated as:

$$a - x_{trans} = 2a\lambda, \tag{2.21}$$

where λ is a non-dimensional quantity between 0 and 1 derived as (see [40] for details on the derivation):

$$\lambda = 1 - \theta_y |\sigma_y|. \tag{2.22}$$

In (2.22), θ_y is called the composite tire model parameter and defined as:

$$\theta_y \quad := \quad \frac{2c_{py}a^2}{3\mu F_z},$$

(2.23)

where c_{py} is a given lateral stiffness of tread elements, F_z is the normal force on the tire, and μ is the tire-road friction coefficient. In (2.22), σ_y denotes the tire lateral slip [42]:

$$\sigma_y \quad := \quad \tan\alpha_s,$$

(2.24)

where the tire slip angle α_s is defined as

$$\alpha_s \quad := \quad \delta_{steer} - \delta_{wheel}.$$

(2.25)

The steering angle δ_{steer} is the angle between the vehicle longitudinal axis and the tire longitudinal (x) axis, while δ_{wheel} denotes the angle between the vehicle longitudinal axis and the wheel velocity V. Note that the tire slip angle α_s is linearly correlated with δ_{steer}.

The lateral force F_y and the aligning moment M_z are calculated as follows:

$$F_y \quad = \quad \mu F_z(1 - \lambda^3)sgn(\alpha_s)$$

(2.26)

$$M_z \quad = \quad -\mu F_z a\lambda^3(1 - \lambda)sgn(\alpha_s).$$

(2.27)

The ratio of M_z to F_y is referred to as the pneumatic trail t:

$$t \quad = \quad -\frac{M_z}{F_y} = a\frac{\lambda^3}{1 + \lambda + \lambda^2}.$$

(2.28)

2.7.2   Friction Coefficient

The friction coefficient μ is estimated by solving the nonlinear equations in (2.26) and (2.27), where the unknown variables are θ_y and σ_y due to λ in (2.22). If a solution of θ_y is converged, the friction coefficient μ is calculated as:

$$\mu = \frac{2c_{py}a^2}{3F_z\theta y}.$$

(2.29)

2.8   Incorporation of Vehicle Steering

All the steps for the proposed algorithm have been presented in the previous sections. The proposed algorithm yields acceptable estimation results with small steering maneuvers, as will be shown in the *Experimental Results*.

The proposed algorithm, however, does not take into account the vehicle steering. Therefore, the estimation results degrade in maneuvers with large steering, as will be illustrated in the *Experimental Results* section. According to (2.22)-(2.25), λ is a function of the steering angle δ_{steer}. The pneumatic trail t in (2.28) is also a function of δ_{steer} since it is a function of λ. However, the algorithm proposed in the previous sections sets t to be a fixed value as a tuning parameter in (2.19), which cannot account for the vehicle steering. This section presents an alternative algorithm adapted for large steering maneuvers.

2.8.1 Models for Lateral Deflection and Change of Lateral Velocity

In order to incorporate the steering angle, the change of lateral velocity as well as the lateral deflection is used.

2.8.1.1 Longitudinal Kinematics Inside the Contact Patch

Based on the STM in Fig. 2.1, the longitudinal kinematics is derived for the lateral deflection and the change of lateral velocity models.

The longitudinal coordinate x is a function of angular positions θ and ϕ inside the contact patch:

$$x = -r_{loaded}\tan\theta = r_{loaded}\tan\phi. \tag{2.30}$$

The time-derivative of (2.30) is the longitudinal velocity:

$$\begin{aligned} v_x(t) = \frac{dx}{dt} &= -r_{loaded}\dot\theta\sec^2\theta \\ &= -r_{loaded}\dot\theta\sec^2\phi. \end{aligned} \tag{2.31}$$

The longitudinal velocities at the center of the contact patch and the leading edge are computed as:

$$v_x(t_c) = -r_{loaded}\dot\theta = r_{loaded}\dot\phi \tag{2.32}$$
$$v_x(t_l) = -r_{loaded}\dot\theta\sec^2\phi_l. \tag{2.33}$$

The angular position ϕ at the leading edge is determined as:

$$\phi_l = \sin^{-1}(\frac{x_l}{r_{unloaded}}). \tag{2.34}$$

The loaded radius r_{loaded} is calculated as a function of the unloaded radius $r_{unloaded}$:

$$r_{loaded} = r_{unloaded}\cos\phi_l. \tag{2.35}$$

Since $r_{unloaded}$ can be calibrated off-line and is easier to be estimated than r_{loaded}, using $r_{unloaded}$ is advantageous in implementing the friction coefficient estimation algorithm. The angular position ϕ through the contact patch is a function of the unloaded radius:

$$\begin{aligned} \phi &= \tan^{-1}(\frac{x}{r_{loaded}}) \\ &= \tan^{-1}\left(\frac{x}{r_{unloaded}\cos\left(\sin^{-1}(\frac{x_l}{r_{unloaded}})\right)}\right). \end{aligned} \tag{2.36}$$

The time difference between the leading edge x_l and a position x inside the contact patch is calculated as:

$$\tau \;\; := \;\; t - t_l = \frac{\phi_l - \phi}{\dot{\theta}}, \tag{2.37}$$

where $\dot{\theta}$ is the constant angular velocity.

2.8.1.2 Lateral Deflection Inside the Contact Patch

If $v(t_c)$ in (2.32) and the time difference $\tau = t - t_l$ in (2.37) are substituted into (2.10) with the boundary condition $v_y(t_l) = (2\alpha x_l + \beta)v_x(t_l) = 0$, a new form of the lateral deflection model is written as:

$$
\begin{aligned}
\int_{t_l}^{t} H(t)dt \;\; &= \;\; \int_{t_l}^{t} \int_{t_l}^{t} \left\{ \frac{d^2 y}{dt^2} - \frac{d^2 y}{dt^2}\bigg|_{t_c} \right\} dt dt \tag{2.38} \\
&= \;\; \alpha(x^2 - x_l^2) + \beta(x - x_l) - \alpha\tau^2 \left(\frac{dx}{dt}\bigg|_{t_c} \right)^2 \\
&= \;\; \alpha[(x - x_l)^2 - \{r_{unloaded}(\phi_l - \phi)\cos\phi_l\}^2].
\end{aligned}
$$

Note that the time difference τ in (2.37) is used instead of introducing the average longitudinal velocity, i.e. $\tau = \frac{x - x_l}{\overline{v}_x}$, which is used in the previously proposed algorithm. Since the lateral deflection model in (2.38) does not contain $\overline{v}_x$ to be approximated, it is more accurate than that in (2.14). However, it has more nonlinearity since ϕ is computed by (2.36). Choosing the lateral deflection model between (2.14) and (2.38) relies on circumstances, e.g. computational capability. The steering angle δ_{steer} is included through F_y in $\alpha := -\frac{F_y}{2c_{bend}}$ which is a function of δ_{steer}, as derived in (2.26) by the tire brush model.

If the measured lateral acceleration belongs to category 2, the term $\{r_{unloaded}(\phi_l - \phi)\cos\phi_l\}^2$ is eliminated from (2.38) to be the same as (2.15).

2.8.1.3 Change of Lateral Velocity Inside the Contact Patch

Both the lateral force F_y in (2.26) and the aligning moment M_z in (2.27) are functions of the vehicle steering δ_{steer}. Including both F_y and M_z in the estimation algorithm would be advantageous to account for the influence of the vehicle steering.

The aligning moment M_z is not contained in the lateral deflection model in (2.38). It can be incorporated into the algorithm through the model in the lateral acceleration model in (2.8) or the integration in (2.9). Since an integrator acts as a low-pass filter, this thesis uses the integration model in (2.9) rather than the model in (2.8). Taking integration is equivalent to removing high frequency noises, and therefore the model in (2.9) yields more robustness to uncertainties in a test vehicle.

Note that the integration model in (2.9) describes the change of lateral velocity from the leading edge x_l throughout a position x corresponding to t. Therefore, $H(t)$ in (2.9) becomes

zero at the leading edge $t = t_l$: $H(t_l) = 0$. The change of lateral velocity model is re-written by substituting (2.31), (2.32), (2.33) and (2.37) into (2.9) as follows:

$$
\begin{aligned}
H(t) & = \int_{t_l}^{t} \left(\frac{d^2y}{dt^2} - \frac{d^2y}{dt^2}\bigg|_{t_c} \right) dt \\
& = r_{unloaded}\dot{\theta}\cos\phi_l \\
& \quad \times \{-(2\alpha x + \beta)\sec^2\phi + (2\alpha x_l + \beta)\sec^2\phi_l - 2\alpha r_{unloaded}(\phi_l - \phi)\cos\phi_l\},
\end{aligned}
\tag{2.39}
$$

where the angular positions ϕ_l and ϕ are calculated with (2.34) and (2.36). Note that the term $2\alpha r_{unloaded}(\phi_l - \phi)\cos\phi_l$ is eliminated if the measured lateral acceleration belongs to category 2.

2.8.1.4 Tire Slip Angle

As presented in (2.25), the tire slip angle α_s contains the steering angle δ_{steer}, and therefore the vehicle steering can be taken into consideration through α_s. The tire slip angle α_s^i of the ith tire is approximated as a linear function of the built-in toe angle δ_{toe}^i and the steering angle δ_{steer}^i as follows:

$$
\alpha_s^i = S_{toe}^i \delta_{toe}^i + S_{steer}^i \delta_{steer}^i,
\tag{2.40}
$$

where S_{toe}^i and S_{steer}^i are scaling factors which are tuned for individual vehicles.

2.8.1.5 Normal Force

The lateral force F_y and the aligning moment M_z are affected by the normal force F_z, as presented in (2.26) and (2.27), and therefore F_z influences the tire-road friction coefficient estimation.

The length of the contact patch in the STM in Fig. 2.1 is used to estimate F_z. If the effect of the tire slip angle and the camber angle is neglected, the contact patch length $A = 2a$ is determined by the normal force [8].

Assume the normal force F_z has a linear relationship with the vertical tire deflection, $r_{unloaded} - r_{loaded}$ as $F_z = c_{rad}(r_{unloaded} - r_{loaded})$, where c_{rad} is a known tire radial stiffness and $r_{loaded} = \sqrt{r_{unloaded}^2 - a^2}$. Then, the normal force F_z is derived as a nonlinear function of the contact patch length A [17]:

$$
F_z = c_{rad}\left(r_{unloaded} - \sqrt{r_{unloaded}^2 - \frac{A^2}{4}}\right),
\tag{2.41}
$$

where the length of the contact patch A is estimated using the radial acceleration, as proposed previously.

2.8.1.6 Friction Coefficient

As presented in (2.26) and (2.27), F_y and M_z are determined by λ which is a function of the composite tire model parameter θ_y. Therefore, θ_y is estimated by applying the least-square curve-fitting technique based on the models in (2.38) and (2.39) to the integration and the double integration of the lateral acceleration only inside the contact patch in Fig. 2.7. Then, the friction coefficient μ is calculated with θ_y, as presented in (2.29).

2.9 Experimental Results

The effectiveness of the new tire-road friction coefficient estimation algorithm is validated with experimental tests to differentiate three road surface conditions, i.e. icy, snowy, and asphalt roads. Three classes of experimental maneuvers are performed at different vehicle speeds and at small and large tire slip angles. One class is a slow lane change, in which the steering wheel is turned by around $\pm 5^o$, and the vehicle speeds are 32, 48, 64, 80, 96 kph ($= 20, 30, 40, 50, 60$ mph). The other class is a steady-state surface transition, in which the vehicle travels straight on a road with successive different road surface conditions: asphalt-ice. The last one is a sinusoidal steering, in which a driver keeps steering to the left and the right with different vehicle speeds: 48, 64, 80 kph.

Among all four tires, two proposed friction coefficient estimation algorithms are applied to a rear-left (RL) tire which has a toe angle, i.e. built-in tire slip angle, of 0.15^o. Front tires can be steered unintentionally during driving, whereas rear tires are fixed. Therefore, the front tires have more noise than the rear ones.

2.9.1 Experiment Setup

Experimental tests were conducted at the *Smithers Winter Test Center* with the support by the *Tyre Systems & Vehicle Dynamics Division of Pirelli Tyres SpA* and the *Research and Innovation Center of Ford Motor Company*.

A test vehicle, Volvo XC90, is equipped with Pirelli Scorpion Ice & Snow tires ($235/60R18$) with 2.3 bar air pressure. Two data acquisition (DAQ) systems are constructed in the test vehicle. One is for the acceleration measurement from the tire sensors, i.e. 3D wireless accelerometers attached on the center line of the tire inner liner. The other is for the measurements from the vehicle sensors, e.g. steering angles and wheel angular velocities, and those from GPS/IMU, e.g. yaw-rate, a forward vehicle velocity, and traveled distance.

Time-synchronization is required in storing the measurement data, as shown in Fig. 2.15. The acceleration data collected from four tires are sent to a computer. The data from GPS/IMU are collected along with the data from other vehicle sensors transmitted via CAN bus, and then those are sent to the computer. An impulse signal is used for the time-synchronization between the acceleration data and the data from GPS/IMU and other vehicle sensors.

The acceleration data from tires and vehicle velocity data are used in the friction coefficient estimation algorithm, whereas the measurements from other vehicle sensors and GPS/IMU are used to check and understand what is happening on the test vehicle.

2.9.2 Algorithm 1 - Vehicle Steering Not Incorporated

In this section, the measurement data are applied to the first friction coefficient estimation algorithm which does not incorporate the vehicle steering.
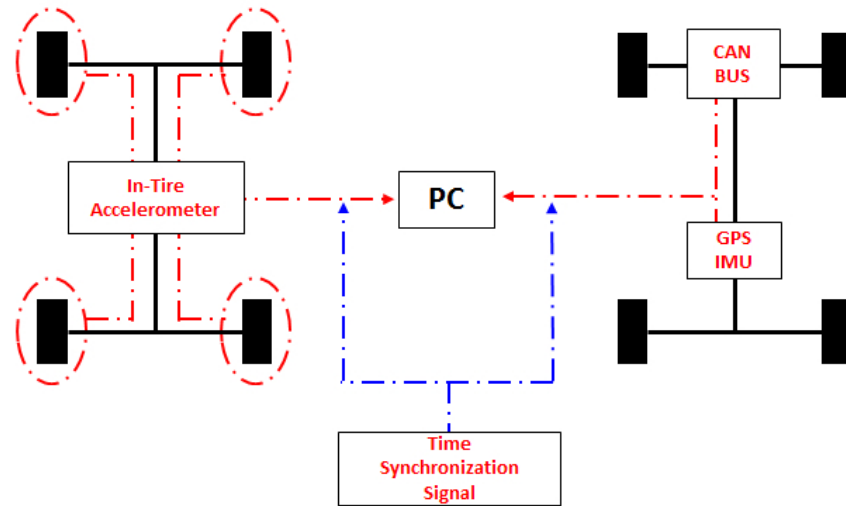
Figure 2.15: Experiment Setup [31] ©2013 Taylor & Francis

2.9.2.1   Slow Lane Change

The steering wheel is turned by around $\pm 5^o$ in most experimental tests of the slow lane change
maneuver. This means the front wheels are steered by around $\pm 0.31^o$ since the steering ratio
of the test vehicle is known to be 15.9. Absolute values of the front wheel steering angle for
all experiments in the slow lane change maneuver are presented in Fig. 2.16. The circle point
at the center represents the mean value, while the dark and light colored bands indicate σ
(standard deviation) and 2σ which covers 68.2 % and 95.4 % of samples, respectively, under
the assumption of a normal distribution. The front wheel steering angle is less than 1°, as
shown in Fig. 2.16, which implies that tires of the test vehicle have the small tire slip angles
in the slow lane change maneuver.
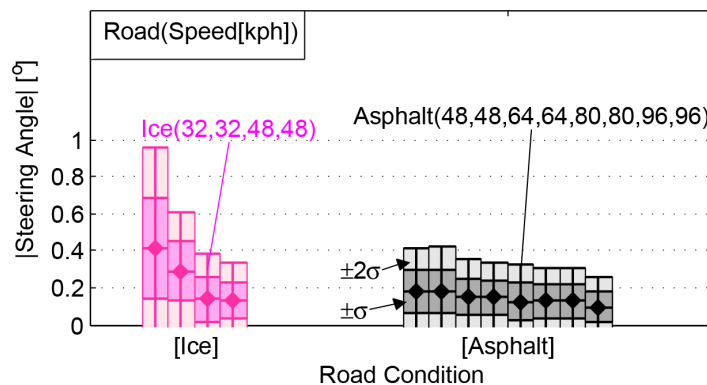
Figure 2.16: Front Wheel Steering Angle [31] ©2013 Taylor & Francis

The new algorithm is motivated by the existing algorithm in [18] that could not dif-
ferentiate the road surface conditions between asphalt and icy roads with the test vehicle.

Table 2.4: Mean and Standard Deviation of Front Wheel Steering Angle [31] ©2013 Taylor & Francis

	Ice							
Speed	32	32	48	48				
Mean	0.41	0.29	0.41	0.13				
σ	0.27	0.16	0.12	0.10				
	Asphalt							
Speed	48	48	64	64	80	80	96	96
Mean	0.18	0.18	0.15	0.15	0.12	0.13	0.13	0.09
σ	0.12	0.12	0.10	0.10	0.10	0.09	0.09	0.08

The friction coefficient estimation results of the existing algorithm is presented in Fig. 2.17, where the vehicle speed is 48 kph ($\approx$ 30 mph). The horizontal lines indicate the mean values of the estimated friction coefficients. Note that most estimated friction coefficients on the icy road are greater than those on the asphalt road. Furthermore, some friction coefficient estimates coincide.
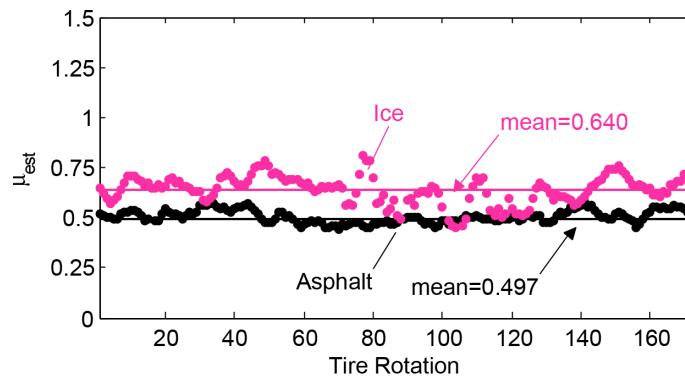
Figure 2.17: Existing Friction Coefficient Estimation Algorithm [31] ©2013 Taylor & Francis

The first tire-road friction coefficient estimation algorithm successfully differentiate the road surface conditions, as shown in Fig. 2.18, where the vehicle speed is 48 kph ($\approx$ 30 mph). The mean value of the estimated friction coefficients are denoted as the horizontal lines. The dark and light colored bands indicate σ(standard deviation) and 2σ which covers 68.2 % and 95.4 % of the estimated friction coefficients, respectively, under the assumption of a normal distribution. As shown in Fig. 2.18a and Table 2.5, the friction coefficient estimates on the asphalt road are greater than those on the icy road, and the gap between two road surface conditions is large enough to clearly differentiate.

As discussed previously, η in the estimation of the aligning moment M_z in (2.20) is

(a) $\eta = 0.25$

(b) $\eta = 0.1$
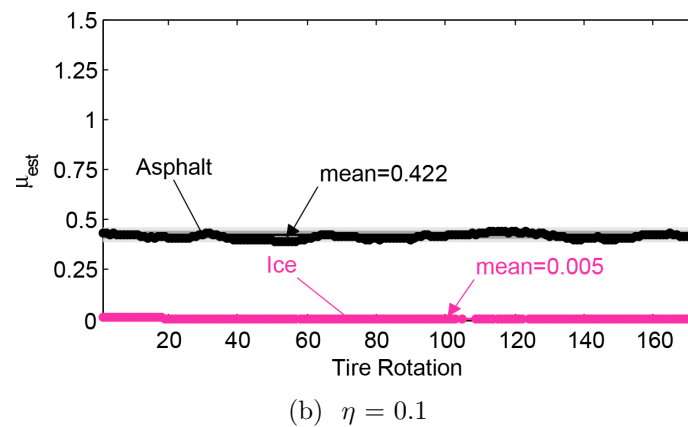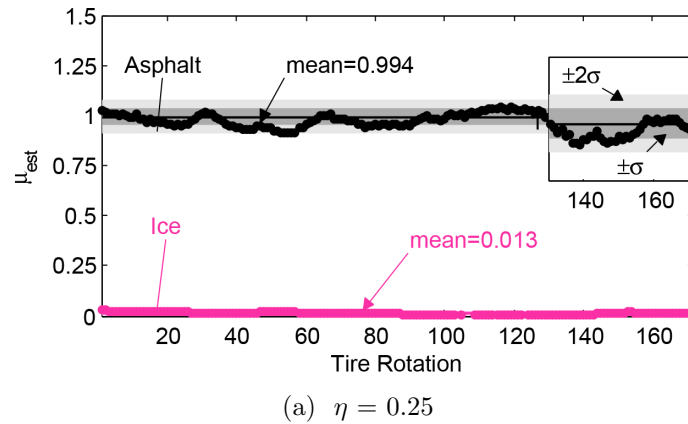
Figure 2.18: Estimated Friction Coefficient for Slow Lane Change (Asphalt and Ice) [31]
©2013 Taylor & Francis

Table 2.5: Mean and Standard Deviation of Estimated Friction Coefficient for Slow Lane
Change (Asphalt and Ice) [31] ©2013 Taylor & Francis

		Ice	Asphalt
(a) $\eta = 0.25$	Mean	0.013	0.994
	σ	0.006	0.040
(b) $\eta = 0.1$	Mean	0.005	0.442
	σ	0.003	0.017

a tuning parameter, for which any value between 0 and 1 can be chosen as long as the
nonlinear equations from the tire brush model converge to a solution for the friction coefficient
estimation. The estimation results with the different choice of η are presented in Fig. 2.18b.
The different values of η affect the order of the magnitude of the friction coefficient estimates.

However, the road surface conditions are still differentiated as shown in Fig. 2.18a and 2.18b.
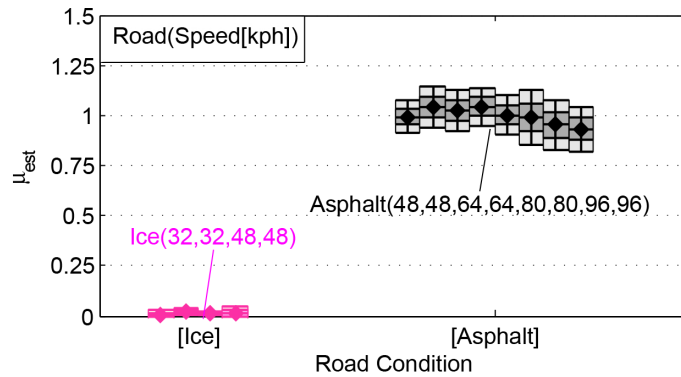
(a) Removing Shift
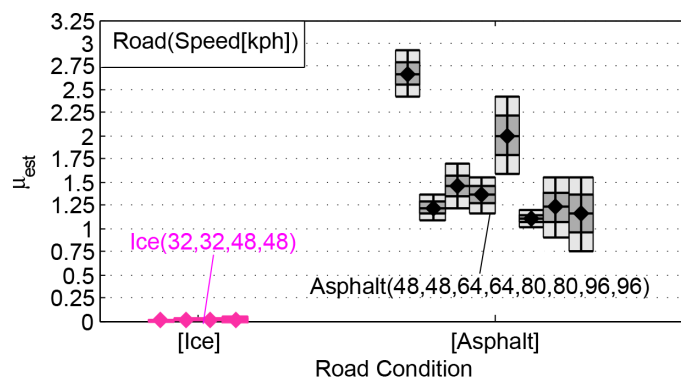
(b) No Removnig Shift

Figure 2.19: Estimated Friction Coefficients for Slow Lane Change (All Experiments), $\eta = 0.25$ [31] ©2013 Taylor & Francis

All experimental results for the friction coefficient estimation are presented in Fig. 2.19a with different vehicle speeds. Each block represents an experiment at a certain vehicle speed. The circle point at the center indicates the mean value, while the dark and light colored bands for each block indicate σ and 2σ. As shown in Fig. 2.19a and Table 2.6, the road surfaces between asphalt and icy roads are differentiated for all the experimental tests.

The robustness of the proposed estimation algorithm is demonstrated through Fig. 2.19b and Table 2.7, in which the friction coefficients were estimated without removing the shift in the lateral acceleration corresponding to the lateral deflection without compressive component, i.e. category 1. The mean value and the deviation are random for every experiment on the asphalt road as shown in Fig. 2.19b and Table 2.7, whereas those are consistent in Fig. 2.19a.

Table 2.6: Mean and Standard Deviation of Estimated Friction Coefficients for Slow Lane Change (All Experiments) : $\eta = 0.25$ [31] ©2013 Taylor & Francis

Removing Shift							
			Ice				
Speed	32	32	48	48			
Mean	0.004	0.018	0.013	0.013			
σ	0.012	0.008	0.006	0.017			
			Asphalt				
Speed	48	48	64	64	80	80	96	96
Mean	0.99	1.04	1.02	1.04	1.00	0.99	0.95	0.93
σ	0.04	0.05	0.05	0.05	0.05	0.07	0.06	0.06

Table 2.7: Mean and Standard Deviation of Estimated Friction Coefficients for Slow Lane Change (All Experiments) : $\eta = 0.25$ [31] ©2013 Taylor & Francis

No Removing Shift							
			Ice				
Speed	32	32	48	48			
Mean	0.004	0.018	0.013	0.014			
σ	0.006	0.008	0.006	0.020			
			Asphalt				
Speed	48	48	64	64	80	80	96	96
Mean	2.67	1.22	1.46	1.36	2.01	1.10	1.23	1.16
σ	0.13	0.07	0.12	0.10	0.20	0.05	0.16	0.20

2.9.2.2 Steady-State Surface Transition

When traveling straight with no steering on successive road surfaces, i.e. asphalt and icy roads, at a constant vehicle speed 48 kph ($\approx$ 30 mph), the friction coefficient estimation results are degraded, as shown in Fig. 2.20. The mean value of the measured front wheel steering angle is $\pm 0.041^o$ for this maneuver, which is smaller than those for the slow lane change maneuver in Table 2.4. This implies that the tire slip angle is mainly due to the toe angle 0.15^o in the steady-state surface transition maneuver.

Since the proposed estimation algorithm is based on the lateral deflection, the proposed estimation algorithm cannot differentiate the road surface conditions when traveling straight, i.e. at very small tire slip angle, as shown in Fig. 2.20. In Fig. 2.20, two horizontal solid lines indicate the mean values of the estimated friction coefficients for each road surface

condition, respectively. The mean value on the asphalt road, 0.544, is smaller than that on
the icy road, 0.843. However, the slow lane change maneuver is even closer to the normal
driving in real life than the maneuver of traveling ahead with no steering. Therefore, the
lateral deflection-based friction coefficient estimation algorithm is still a promising way to
identify the road surface conditions.
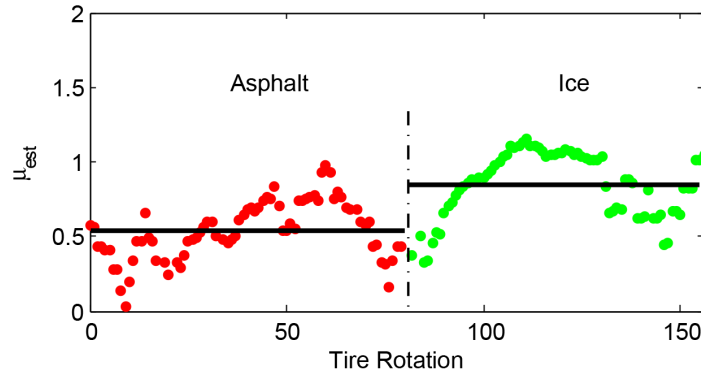
Figure 2.20: Estimated Friction Coefficient for Steady-State Surface Transition [31] ©2013
Taylor & Francis

2.9.3   Algorithm 2 - Vehicle Steering Incorporated

In this section, the measurement data are applied to the second friction coefficient estimation
algorithm which incorporates the vehicle steering.

2.9.3.1   Sinusoidal Steering

Large steering maneuvers are performed at constant vehicle speeds: 48, 64 and 80 kph.
When driving with a vehicle speed of 48 kph, the steering wheel is turned by about $\pm 20^o$
which corresponds to the steering angle of the front wheel turned by around $\pm 1.26^o$ since
the steering ratio of the test vehicle is known to be 15.9. If the vehicle steering is not
included in the estimation algorithm, the friction coefficient estimates change along with the
steering wheel angle, as shown in Fig. 2.21a. The solid line represents the steering wheel
angle, and each dot represents the friction coefficient estimates for one tire rotation. The
horizontal line is the mean value of the friction coefficient estimates. The dark and light
colored bands indicate σ (standard deviation) and 2σ which covers 68.2 % and 95.4 % of
samples, respectively, under the assumption of a normal distribution.

Fig. 2.21a manifests that the first proposed algorithm cannot estimate the friction coeffi-
cient with the large steering maneuvers. The second proposed algorithm, however, incorpo-
rates the vehicle steering, and significantly diminishes the influence of the vehicle steering,
as shown in Fig. 2.21b. Little change is observed in the friction coefficient estimates in Fig.
2.21b while turning the steering wheel. Fig. 2.22 presents the friction coefficient estimation
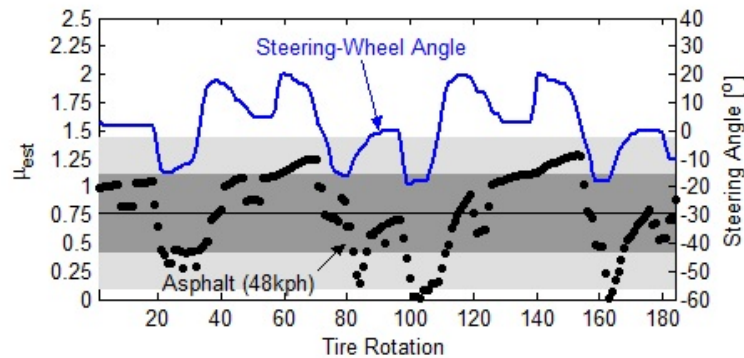
(a) Not Incorporating δ_{steer} ($mean = 0.77$, $\sigma = 0.34$)
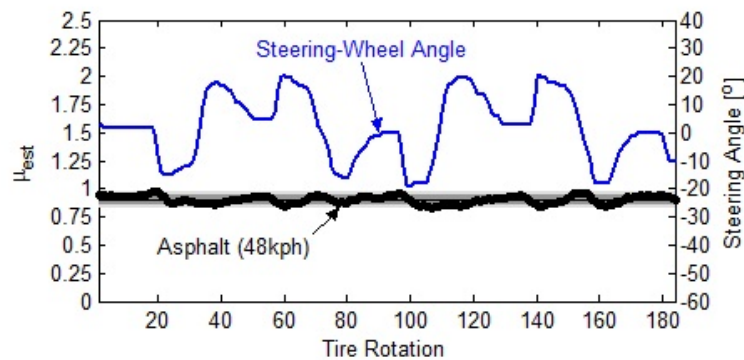
(b) Incorporating δ_{steer} ($mean = 0.90$, $\sigma = 0.03$)

Figure 2.21: Friction Coefficient Estimation on Asphalt at 48 kph (Steering Wheel $\simeq \pm 20^o$)
[29] ©2013 IEEE

results for driving with a vehicle speed of 64 kph, which shows the diminished influence of
the vehicle steering.

If the vehicle is driven with 80 kph, some influence of the vehicle steering is observed,
as shown in Fig. 2.23b. However, the change of μ estimates is reduced compared to that in
Fig. 2.23a. Furthermore, the steering wheel is turned by around $\pm 13^o$, which is considerably
intense driving maneuver with the vehicle speed 80 kph. This is not close to normal driving.
Therefore, the second proposed friction coefficient estimation algorithm is still promising for
large steering maneuvers.

2.9.3.2   Slow Lane Change - Ice, Snow, and Asphalt

If the experimental measurements in the slow lane change maneuver is applied to the esti-
mation algorithm, three road surface conditions are mostly differentiated, as shown in Fig.
2.24.

Note that an additional signal processing is used to obtain smoother estimation results;
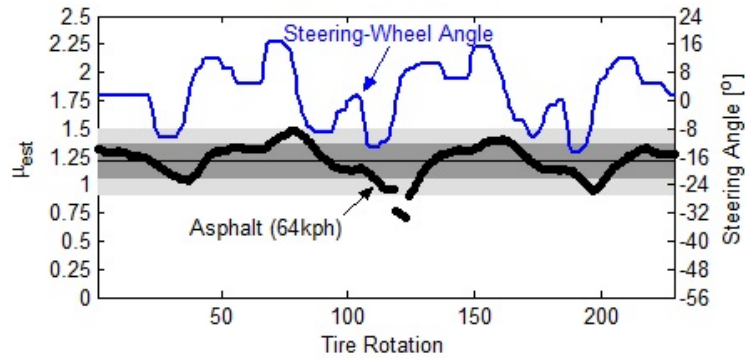
(a) Not Incorporating δ_{steer} ($mean = 1.21$, $\sigma = 0.15$)
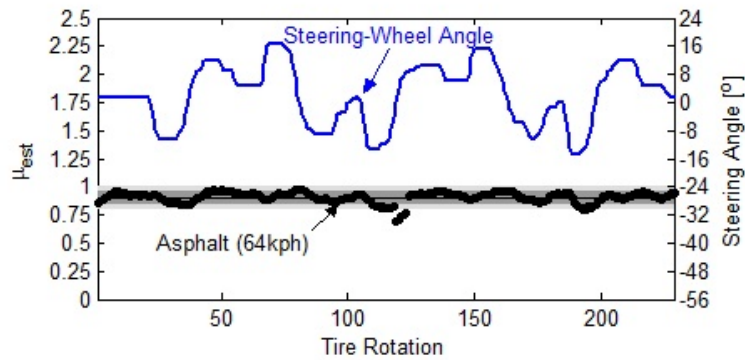
(b) Incorporating δ_{steer} ($mean = 0.91$, $\sigma = 0.05$)

Figure 2.22: Friction Coefficient Estimation on Asphalt at 64 kph (Steering Wheel $\simeq \pm 16^o$)
[29] ©2013 IEEE

this will be illustrated in detail in the *Experimental Results* section of Chapter 3. In order to
obtain the smoother estimation results, the Kalman Filter is used based on the state-space
model written as:

$$\bar{\mu}(k) = \bar{\mu}(k-1) \tag{2.42}$$
$$\bar{d}(k) = \mu(k) = \bar{\mu}(k) + \bar{e}(k). \tag{2.43}$$

The estimate before the additional processing is denoted as $\mu(k)$, which is the measurement
for the system in (2.42)-(2.43). The estimate after the additional processing is denoted as
$\bar{\mu}(k)$. The noise $\bar{e}$ in (2.43) is assumed to be white, stationary, and normally distributed
with zero mean.
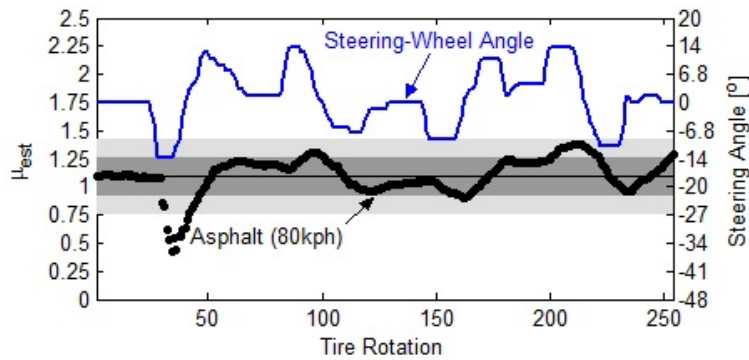
(a)   Not Incorporating δ_{steer} $(mean = 1.10, \sigma = 0.17)$
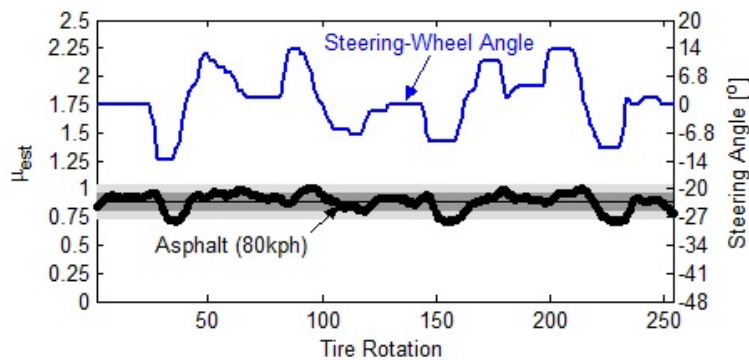
(b)   Incorporating δ_{steer} $(mean = 0.89, \sigma = 0.08)$

Figure 2.23: Friction Coefficient Estimation on Asphalt at 80 kph (Steering Wheel $\simeq \pm 13^{o}$)
[29] ©2013 IEEE
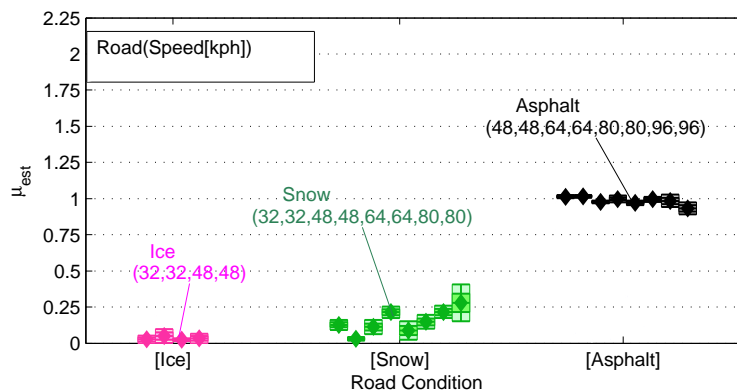
Figure 2.24: Friction Coefficient Estimation on Icy, Snowy, and Asphalt Roads

2.10   Conclusion

Two tire-road friction coefficient estimation algorithms are proposed in this chapter. The lat-
eral acceleration only inside the contact patch is used in the algorithms to ensure robustness

to the orientation-variation of the accelerometer body frame. The first algorithm is based
on the lateral deflection, and the second one is based on the change of lateral velocity as
well as the lateral deflection. The proposed algorithms are validated with three experimental
maneuvers.

Chapter 3

A Novel Algorithm for Vehicle Inertial Parameter Identification based on a Dual Unscented Kalman Filter

3.1   Introduction

This thesis proposes a novel approach to identify vehicle inertial parameters of a passenger car: a vehicle sprung mass (m_s), yaw moment of inertia (I_z), and longitudinal position of the CoG (l_f). These parameters affect the closed-loop behaviors of vehicle control systems

The proposed identification algorithm is based on a four-wheel nonlinear vehicle model with roll dynamics. In order to provides a theoretical background to establish criteria for the activation of the algorithm, a local observability analysis for the inertial parameter identification is performed with the nonlinear vehicle model. The vehicle sprung mass m_s is determined by estimating the additional mass m_a loaded on the empty sprung mass. A relationship between m_a, I_z, and l_f is derived by using the *Parallel-Axis Theorem*, which allows a reduction in complexity of the identification algorithm. As an estimation technique, a dual unscented Kalman filter framework is used for the simultaneous estimation of the inertial parameters and the vehicle state variables. Standard vehicle sensors, such as accelerometers and a gyroscope, are used for the identification, whereas more advanced equipment, e.g. a Global Positioning System (GPS) and suspension displacement sensors, are assumed to be unavailable. Extensive simulations and experimental tests illustrate the capability of the algorithm to differentiate between two driving conditions on a flat road with a constant tire-road friction coefficient. Note that the contents of this chapter have been published in a journal [30].

3.2 Vehicle Model

The identification algorithm to be developed in this chapter uses the four-wheel vehicle model which has four degree-of-freedom: longitudinal (x) and lateral (y) translational motion, yaw (ψ) rotation about the z-axis, and roll (ϕ) rotation about the x-axis in Fig. 3.1.

The vehicle state vector is defined as $s := [s_1,\ s_2,\ s_3,\ s_4,\ s_5]^\top = [v_x,\ v_y,\ \dot{\psi},\ \phi,\ \dot{\phi}]^\top$, and the dynamic equations are:

$$\dot{s}_1 = \dot{v}_x = a_x + v_y\dot{\psi} \tag{3.1}$$

$$\dot{s}_2 = \dot{v}_y = a_y - v_x\dot{\psi} \tag{3.2}$$

$$\dot{s}_3 = \ddot{\psi} = \frac{1}{I_z}\{l_w(F_x^{fr} + F_x^{rr}) - l_w^l F_x \tag{3.3}$$

$$+ l_f F_y - l(F_y^{rl} + F_y^{rr})\}$$

$$\dot{s}_4 = \dot{\phi} = \dot{\phi} \tag{3.4}$$

$$\dot{s}_5 = \ddot{\phi} = \frac{1}{I_x}\left\{m_s h_s(a_y + g\phi) - k_\phi\phi - c_\phi\dot{\phi}\right\}. \tag{3.5}$$

The track widths on the front and rear axles in Fig. 3.1 are assumed to be the same: $l_w = l_w^f = l_w^r$. The portion of l_w to the left of the center of gravity (CoG) is denoted as l_w^l in (3.3). In (3.5), m_s indicates the vehicle sprung mass, h_s indicates the height from the roll center to the CoG of sprung mass, and k_ϕ and c_ϕ denote the rolling stiffness and damping, respectively.
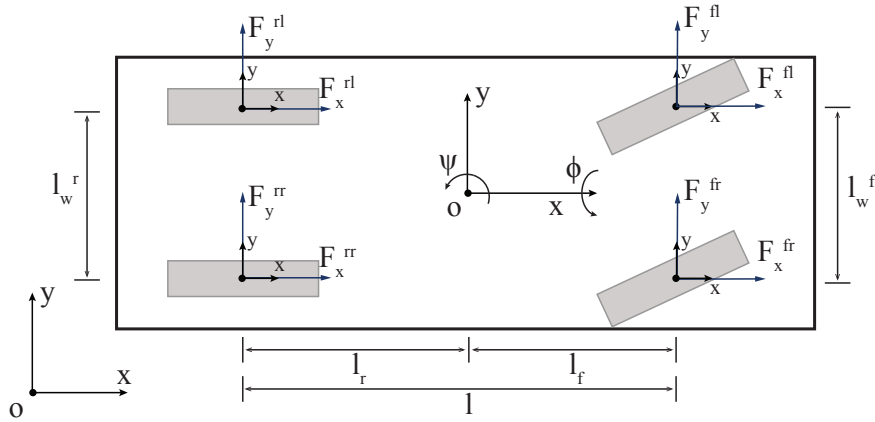
Figure 3.1: 4-Wheel Vehicle Model with Roll Dynamics [30] ©2014 IEEE

In the above equations, F_x^i and F_y^i indicate the tire forces in the vehicle longitudinal (x) and lateral (y) directions, respectively, at the ith wheel in Fig. 3.1. The column vector u is defined to contain the tire forces as follows:

$$u := [\{F_x^i\}_{i\in\mathcal{I}},\ \{F_y^i\}_{i\in\mathcal{I}}]^\top,$$

where $\mathcal{I} = \{fl, \ fr, \ rl, \ rr\}$ is a set indicating front-left, front-right, rear-left, and rear-right wheels.

The vehicle longitudinal acceleration a_x in (3.1) and lateral acceleration a_y in (3.2) are calculated as:

$$a_x = \frac{F_x - F_{aero}}{m} \tag{3.6}$$

$$a_y = \frac{F_y}{m}, \tag{3.7}$$

where F_x and F_y indicate the total vehicle longitudinal and lateral forces, respectively, and they are computed as $F_x = \sum_{i \in \mathcal{I}}\{F_x^i\}$ and $F_y = \sum_{i \in \mathcal{I}}\{F_y^i\}$. The aerodynamic drag force F_{aero} in (3.6) is computed as $F_{aero} = \frac{1}{2}\rho C_d A_f v_x^2$ with the mass density of air ρ, the aerodynamic drag coefficient C_d, and the frontal area of a vehicle A_f (see [42]). The total vehicle mass, i.e. the sum of the sprung mass m_s and the mass of all wheels m_t, is denoted as m in (3.6) and (3.7). Note that the vehicle longitudinal force F_x in (3.6) contains the rolling resistance force [32].
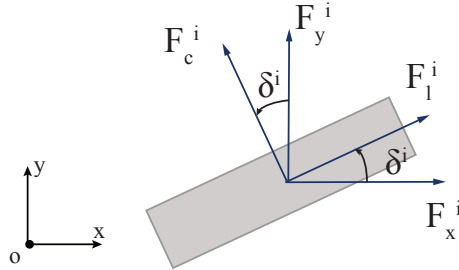
Figure 3.2: Tire Longitudinal and Lateral Forces [30] ©2014 IEEE

The vehicle longitudinal and lateral forces at the ith wheel, F_x^i and F_y^i, are calculated with the tire longitudinal and lateral forces, F_l^i and F_c^i, as shown in Fig. 3.2:

$$F_x^i = F_l^i \cos \delta^i - F_c^i \sin \delta^i, \ (i \in \mathcal{I}) \tag{3.8}$$
$$F_y^i = F_l^i \sin \delta^i + F_c^i \cos \delta^i, \ (i \in \mathcal{I}), \tag{3.9}$$

where δ^i denotes the steering angle of the ith wheel. Note that the steering angles are zero for the rear wheels. The calculation of the tire longitudinal and lateral forces, F_l^i and F_c^i, will be discussed in detail in the *Tire Forces* section.

The lateral acceleration $a_{y,sensor}$, the longitudinal velocity v_x, the yaw rate $\dot{\psi}$, and the longitudinal acceleration a_x constitute the measurement vector d. Due to the roll dynamics about the longitudinal x-axis, the measured lateral acceleration $a_{y,sensor}$ in [53] is modeled as:

$$a_{y,sensor} = a_y - h_{acc}\ddot{\phi} - g\phi,$$

where the height from the roll center to the accelerometer h_{acc} is assumed to be the same as h_s. The measurement vector d is expressed as a function of s and $\dot{s}$ using (3.1)-(3.5):

$$d \quad := \quad \begin{bmatrix} a_{y,sensor}, & v_x, & \dot{\psi}, & a_x \end{bmatrix}^\top \tag{3.10}$$

$$= \quad G(s, \ \dot{s}) = \begin{bmatrix} \dot{s}_2 + s_1 s_3 - h_{acc}\dot{s}_5 - g s_4 \\ s_1 \\ s_3 \\ \dot{s}_1 - s_2 s_3 \end{bmatrix}.$$

The vehicle sprung mass m_s is the sum of the additional sprung mass m_a, such as passengers and luggage, and the empty vehicle sprung mass $m_{s,emp}$ specified by automobile manufacturers. The algorithm to be proposed will identify the additional sprung mass, m_a, and the longitudinal position of the CoG, l_f. Therefore, the vehicle inertial parameter vector is defined as:

$$w := [m_a, \ l_f]^\top. \tag{3.11}$$

The yaw moment of inertia I_z is identified with the estimated m_a and l_f, as will be discussed in the next section.

Equations (3.1)-(3.11) is compactly written as the continuous state-space model:

$$\dot{s}(t) \quad = \quad F(w(t), \ s(t), \ u(t)) \tag{3.12}$$

$$\dot{w}(t) \quad = \quad 0 \tag{3.13}$$

$$d(t) \quad = \quad G(s(t), \ \dot{s}(t)). \tag{3.14}$$

Note that the time-derivative of w is zero since the inertial parameters are assumed to be constant while driving a passenger vehicle.

When using Euler forward discretization, the discretized state-space representation for (3.12)-(3.14) is:

$$s(k+1) \quad = \quad s(k) + \tau_s F(w(k), \ s(k), \ u(k)) + v(k) \tag{3.15}$$

$$= \quad T(w(k), \ s(k), \ u(k)) + v(k)$$

$$w(k+1) \quad = \quad w(k) + r(k) \tag{3.16}$$

$$d(k) \quad = \quad G(s(k), \ \dot{s}(k)) + e(k), \tag{3.17}$$

where τ_s is the sampling time, v in (3.15) and r in (3.16) are the process noises, and e in (3.17) is the measurement noise. The noises v, r, and e are assumed to be white, stationary, and normally distributed with zero mean. Note that the inertial parameter dynamic model in (3.16) has the identity transition matrix since the time-derivative $\dot{w}$ is zero in (3.13). The state-space equations (3.15) and (3.17) are used for the estimation of the vehicle state s, and the equations (3.16) and (3.17) are used in identifying the inertial parameter w.

3.3 The relationship between I_z, m_a, and l_f

The yaw moment of inertia I_z and the position of the vehicle sprung mass CoG change if additional masses, such as fuel tank, passengers, or luggage, are loaded on the empty vehicle. The CoG position is located by the distance from the front axle l_f and the distance from the left edge l_w^l as denoted in Fig. 3.3.
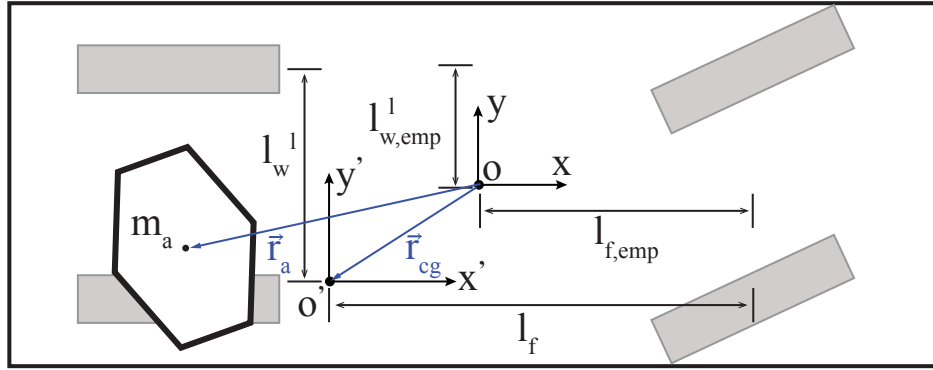
Figure 3.3: Vehicle with an Additional Mass [30] ©2014 IEEE

Assume a rigid body of mass m_a is added to the empty vehicle in Fig. 3.3. Then, the vehicle sprung mass m_s is the sum of the empty vehicle sprung mass $m_{s,emp}$ and the additional mass m_a: $m_s = m_{s,emp} + m_a$. Note that the coordinate frame oxy is at the CoG of the empty vehicle sprung mass $m_{s,emp}$, and the coordinate frame $o'x'y'$ is at the new CoG of the sprung mass after loading the additional mass m_a.

The new CoG position vector of the vehicle sprung mass m_s in the oxy frame is indicated as $\vec{r}_{cg}$, as shown in Fig. 3.3. The position vector of the CoG of m_a is $\vec{r}_a$ in the frame oxy, and it is expressed as:

$$
\begin{aligned}
m_s\vec{r}_{cg} &= m_{s,emp}\vec{0} + m_a\vec{r}_a \\
\Rightarrow \vec{r}_a &= \frac{m_s}{m_a}\vec{r}_{cg}.
\end{aligned}
\tag{3.18}
$$

The new yaw moment of inertia in the oxy frame, I_z^{oxy}, is calculated as:

$$
I_z^{oxy} = I_{z,emp} + m_a\|\vec{r}_a\|_2^2,
\tag{3.19}
$$

where $I_{z,emp}$ is the yaw moment of inertia of the empty vehicle sprung mass $m_{s,emp}$. Note that m_a is assumed to be a point mass when calculating the yaw moment of inertia in (3.19), i.e. the yaw moment of inertia of m_a with respect to its own CoG is neglected. Using the *Parallel-Axis Theorem* [6], I_z^{oxy} is expressed as:

$$
I_z^{oxy} = I_z^{o'x'y'} + m_s\|\vec{r}_{cg}\|_2^2,
\tag{3.20}
$$

where $I_z^{o'x'y'}$ represents the new yaw moment of inertia in the $o'x'y'$ frame, and this is the yaw moment of inertia to be estimated. When combining (3.19) and (3.20), the new yaw moment of inertia in the $o'x'y'$ frame is:

$$I_z^{o'x'y'} \quad = \quad I_{z,emp} + m_a\|\vec{r}_a\|_2^2 - m_s\|\vec{r}_{cg}\|_2^2. \tag{3.21}$$

If $\vec{r}_a = \frac{m_s}{m_a}\vec{r}_{cg}$ in (3.18) is substituted into (3.21), the yaw moment of inertia after loading the additional mass m_a is written as:

$$I_z^{o'x'y'} \quad = \quad I_{z,emp} + m_s \left(\frac{m_s}{m_a} - 1 \right) \|\vec{r}_{cg}\|_2^2, \tag{3.22}$$

where $m_s = m_{s,emp} + m_a$.

Note that the position vector $\vec{r}_{cg}$ is expressed as $\vec{r}_{cg} = (l_{f,emp} - l_f)\vec{e}_x + (l_{wl,emp} - l_w^l)\vec{e}_y$, as shown in Fig. 3.3, where $\vec{e}_x$ and $\vec{e}_y$ are the unit vectors in the x and y directions, respectively. Furthermore, $I_z^{o'x'y'}$ in (3.22) is the same as the yaw moment of inertia I_z in (3.3). Therefore, the yaw moment of inertia after loading the additional mass m_a is expressed as a function of m_a, l_f, and l_w^l:

$$\begin{aligned} I_z \quad &= \quad I_z^{o'x'y'} \\ &= \quad I_{z,emp} + (m_{s,emp} + m_a) \left(\frac{m_{s,emp} + m_a}{m_a} - 1 \right) \\ &\quad \times \{(l_{f,emp} - l_f)^2 + (l_{w,emp}^l - l_w^l)^2\}, \end{aligned} \tag{3.23}$$

where the empty vehicle parameters, $I_{z,emp}$, $m_{s,emp}$, $l_{f,emp}$, and $l_{w,emp}^l$ are assumed to be known.

This thesis will not identify the transverse CoG position l_w^l, and therefore $l_w^l = l_{w,emp}^l$. The inertial parameter $w = [m_a, \ l_f]^\top$ is first identified by substituting (3.23) for I_z in the yaw dynamics in (3.3). Then, the yaw moment of inertia I_z is calculated with the identified m_a, l_f, and the relationship in (3.23). Using this approach, the proposed identification algorithm has less complexity than when m_a, l_f, and I_z are estimated individually.

3.4   Local Observability Analysis

This section demonstrates that the inertial parameter w can be uniquely determined with the measurement d, which is necessary to identify the inertial parameter, $w = [m_a, \ l_f]^\top$. Since the state-space model in (3.15)-(3.17) is a nonlinear function in terms of w, it will be presented that w is locally observable with the measurement $d = G(s, \ \dot{s})$ in (3.10).

By investigating the rank of an observability codistribution matrix, the local observability can be proven, as described in [27][39]. If the observability codistribution matrix has full column rank, w is said to be locally observable.

Define a vector $\mathcal{O}$ consisting of the measurement vector d and its time-derivative $\dot{d}$:

$$\mathcal{O} := \begin{bmatrix} G \\ \dot{G} \end{bmatrix} = \begin{bmatrix} g_1 \\ g_2 \\ g_3 \\ g_4 \\ \dot{g}_1 \\ \dot{g}_2 \\ \dot{g}_3 \\ \dot{g}_4 \end{bmatrix} = \begin{bmatrix} a_y - h_{acc}\ddot{\phi} - g\phi \\ v_x \\ \dot{\psi} \\ a_x \\ \dot{a}_y - h_{acc}\dddot{\phi} - g\dot{\phi} \\ \dot{v}_x \\ \ddot{\psi} \\ \dot{a}_x \end{bmatrix},$$

where d is expressed with a_y, v_x, $\dot{\psi}$, and a_x. The observability codistribution matrix is defined as the Jacobian of $\mathcal{O}$ with respect to the parameter vector w: $\nabla\mathcal{O} = [\partial\mathcal{O}/\partial m_a, \; \partial\mathcal{O}/\partial l_f]$, whose size is 8×2. The partial derivatives of g_1, g_4, and $\dot{g}_3$ with respect to m_a and l_f are derived as follows:

$$\frac{\partial g_1}{\partial m_a} = \sum_{i=5}^{8} u_i \left(\frac{-1}{m^2} + \frac{m_s h_{acc} h_s}{m^2 I_x} - \frac{h_{acc} h_s}{m I_x} \right) - \frac{h_{acc} h_s}{I_x} g s_4$$
$$\frac{\partial g_1}{\partial l_f} = 0$$

$$\frac{\partial g_4}{\partial m_a} = -\frac{1}{m^2} \left(\sum_{i=1}^{4} u_i - \frac{1}{2}\rho C_d A_f s_1^2 \right)$$
$$\frac{\partial g_4}{\partial l_f} = 0$$

$$\frac{\partial \dot{g}_3}{\partial m_a} = 0$$
$$\frac{\partial \dot{g}_3}{\partial l_f} = \frac{-1}{I_z^2} \frac{\partial I_z}{\partial l_f} \left\{ l_w(u_2 + u_4) - l_w^l \sum_{i=1}^{4} u_i + l_f \sum_{i=5}^{8} u_i - l(u_7 + u_8) \right\} + \frac{1}{I_z} \sum_{i=5}^{8} u_i.$$

If the vector $u = [u_1, \; \ldots, \; u_8]$ is not zero, the above partial derivatives of g_1, g_4, and $\dot{g}_3$ ensure the full column rank of the matrix $\nabla\mathcal{O}$. This proves the local observability of w based on the measurement d.

According to this analysis, the identification algorithm pauses to avoid malfunctions if neither the longitudinal excitation $\{u_i\}_{i=1}^{4}$ nor the lateral excitation $\{u_i\}_{i=5}^{8}$ is observed.

3.5 Tire Forces

As computed in (3.8)-(3.9) previously, the vehicle longitudinal and lateral forces at the ith wheel, F_x^i and F_y^i, are determined by the tire longitudinal and lateral forces at the ith wheel, F_l^i and F_c^i. While the tire brush model is used to estimate the tire lateral force F_c^i, the engine torque map and gear ratios are used to estimate the tire longitudinal force F_l^i. Note that the change of tire pressure, temperature, and tire wear are assumed to be negligible.

3.5.1 Tire Lateral Force

The tire lateral force F_y is calculated using the tire brush model which accounts for the non-linear tire characteristics during a normal driving. The tire brush model has been presented in Chapter 2, and therefore equations for the model are briefly reviewed here; refer to the Chapter 2 for details.

The tire lateral force F_c^i of the ith wheel is computed as:

$$F_c^i = \mu F_z^i \{1 - (1 - \theta_y^i |\sigma_y^i|)^3\} sgn(\alpha_s^i), \tag{3.24}$$

where F_z^i indicates the normal force at the ith wheel to be discussed later and μ indicates a known tire-road friction coefficient. Note that the pure lateral tire slip is taken into consideration, and the longitudinal tire slip is neglected.

The composite tire model parameter θ_y^i in (3.24) is defined as:

$$\theta_y^i := \frac{2c_{py}(a^i)^2}{3\mu F_z^i},$$

where c_{py} is the known lateral stiffness of the tread elements and a^i is the half length of the tire-road contact patch. If in-tire accelerometers are available, an approach proposed in Chapter 2 can be applied to estimate a^i. This chapter, however, uses the following relationship:

$$a^i = \sqrt{(r_{unload}^i)^2 - (r_{unload}^i - \frac{F_z^i}{c_{rad}})^2}, \tag{3.25}$$

where c_{rad} is the known tire radial stiffness, and r_{unload} is an unloaded tire radius. The relationship in (3.25) is derived based on the assumption that the vertical tire deflection is linearly proportional to the normal force [29]. Note that a^i of the front tire is assumed to remain constant. If the engine is mounted on the front of a vehicle, additional masses on a passenger vehicle are mostly loaded behind the CoG, e.g. at a trunk and passenger seats. Therefore, the change in a^i of the front tire is negligible.

The tire lateral slip σ_y^i in (3.24) is defined as:

$$\sigma_y^i := \tan \alpha_s^i.$$

The tire slip angle α_s^i is the difference between the steering angle δ^i and the wheel velocity angle δ_{wheel}^i (see [42]):

$$\alpha_s^i := \delta^i - \delta_{wheel}^i.$$

The steering angle δ^i is the angle between the vehicle longitudinal axis and the tire longitudinal axis. The wheel velocity angle δ_{wheel}^i is the angle between the vehicle longitudinal axis

and the wheel velocity vector (see [42]). The angle δ^i_{wheel} is computed with the vehicle state $s = [v_x, \ v_y, \ \dot{\psi}, \ \phi, \ \dot{\phi}]^\top$ as follows:

$$\delta^i_{wheel} \ = \ \tan^{-1}\left(\frac{v_y + \bar{l}^i\dot{\psi}}{\bar{v}^i_x}\right)$$

$$\bar{l}^i \ = \ \begin{cases} l_f & (i = fl, \ fr) \\ l_f - l & (i = rl, \ rr) \end{cases}$$

$$\bar{v}^i_x \ = \ \begin{cases} v_x - \dot{\psi} \cdot l^l_w & (i = fl, \ rl) \\ v_x + \dot{\psi}(l_w - l^l_w) & (i = fr, \ rr). \end{cases}$$

3.5.2 Tire Longitudinal Force

The engine output torque is obtained from the engine torque map, and it is transmitted through the Controller Area Network (CAN) bus. The total tire longitudinal force F_l is computed with the engine torque T_{eng}, the transmission gear ratio R_{trans}, the differential gear ratio R_{diff}, the unloaded tire radius r_{unload}, and scaling factor η:

$$F_l = \sum_{i \in \mathcal{I}} F^i_l \ = \ \frac{T_{eng}R_{trans}R_{diff}}{r_{unload}}\eta, \tag{3.26}$$

where the pure longitudinal tire slip is assumed, and the lateral tire slip is neglected. The total longitudinal force F_l is equally distributed to the driven wheels. The scaling factor η is calculated as $\eta = \frac{r_{unload}}{r_{eff}}\eta_m$, where r_{eff} is the effective tire radius and η_m indicates the mechanical efficiency [5]. Since F_l is estimated only when the lock-up occurs, the torque converter ratio is not taken into consideration.

3.5.3 Normal Force

The tire normal forces are determined by the distribution of the sprung mass and the roll dynamics. The vehicle sprung mass m_s is distributed on the front and rear tires to generate the normal forces, f^f_z and f^r_z [42]:

$$f^f_z \ = \ m_s\frac{l - l_f}{l}g - m_sh_sa_x$$

$$f^r_z \ = \ m_s\frac{l_f}{l}g + m_sh_sa_x.$$

Note that the normal forces f^f_z and f^r_z are affected by the longitudinal acceleration a_x. The forces f^f_z and f^r_z are, in turn, laterally distributed on the left and right tires. The lateral

distribution of f_z^i is calculated as:

$$
\bar{f}_z^i = \begin{cases}
\frac{l_w - l_w^l}{l_w} f_z^f & (i = fl) \\
\frac{l_w^l}{l_w} f_z^f & (i = fr) \\
\frac{l_w - l_w^l}{l_w} f_z^r & (i = rl) \\
\frac{l_w^l}{l_w} f_z^r & (i = rr),
\end{cases}
$$

where $\bar{f}_z^i$ denotes the lateral distribution of f_z^i.

The load transfer between left and right tires is caused by the roll dynamics. Therefore, the total normal force is computed as:

$$
F_z^i = \begin{cases}
\bar{f}_z^i - k_s l_w^l \phi - c_s l_w^l \dot{\phi}, & (i = fl, \ rl) \\
\bar{f}_z^i + k_s (l_w - l_w^l) \phi + c_s (l_w - l_w^l) \dot{\phi}, & (i = fr, \ rr).
\end{cases}
$$

The roll dynamics, ϕ and $\dot{\phi}$, account for the load transfer. The known suspension stiffness and damping are denoted as k_s and c_s, respectively.

3.6   Dual Unscented Kalman Filter

While the identification of the vehicle inertial parameter, $w = [m_a, \ l_f]^\top$, needs the vehicle state, $s = [v_x, \ v_y, \ \dot{\psi}, \ \phi, \ \dot{\phi}]^\top$, the estimation of the vehicle state s also needs the inertial parameter w. Therefore, a dual estimation framework is used for the estimation of s and w, as shown in Fig. 3.4. The inertial parameter $w = [m_a, \ l_f]^\top$ is identified, and then m_a and l_f are used along with (3.23) to determine I_z. The vehicle state estimator receives the identified parameters, m_a, l_f, and I_z, as a vector $w' = [m_a, \ l_f, \ I_z]^\top$, as shown in Fig. 3.4. The vehicle state estimator uses w' to estimate the vehicle state s, and the estimated s is, in turn, used for the inertial parameter estimator.

The vehicle inertial parameters, m_a and l_f, are identified separately using the *switch* block as shown in Fig. 3.4. The criteria used in the *switch* block will be listed in the *Simulation Results* and the *Experimental Results* sections. The m_a estimation is activated when the longitudinal dynamics prevail over the lateral dynamics, whereas the l_f estimation is activated when the lateral dynamics prevail over the longitudinal dynamics. The additional mass m_a can be estimated more accurately with the longitudinal dynamics than is estimated with the lateral dynamics. If m_a is estimated along with l_f in lateral dynamics maneuvers, the inaccurate m_a estimates degrade the accuracy of l_f estimates.

In the inertial parameter estimator in Fig.3.4, the tire longitudinal force F_l is estimated with the engine torque under the prevailing longitudinal dynamics and the tire lateral force F_c is estimated with the tire slip angle α_s, the normal force F_z, and the tire brush model under the prevailing lateral dynamics.
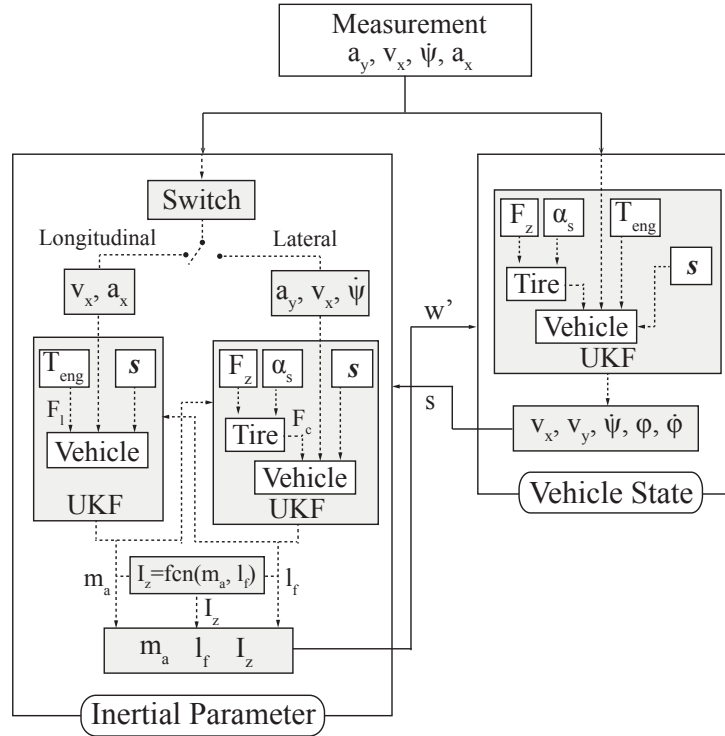
Figure 3.4: Dual Estimation Framework [30] ©2014 IEEE

3.6.1   Unscented Kalman Filter

A wide range of estimation techniques have been applied to the inertial parameter identification. For example, Recursive Least Squares (RLS) and Kalman Filter (KF) can be easily implemented and have fast convergence [58], even if they cannot be applied for nonlinear vehicle models. The KF applies a recursive Bayesian estimation algorithm to a linear state-space model with the assumption of Gaussian probability distributions [4, 21], and it produces the optimal estimate in the sense of the minimum mean squared error (MMSE).

The variants of the KF adapted for nonlinear models, e.g. Extended Kalman Filter (EKF) and Unscented Kalman Filter (UKF), have been applied to the estimation with nonlinear vehicle models [7, 32, 44, 45, 53, 54]. Hong and Smith et al. present the comparison between the estimation results of the EKF and the UKF [32].

This thesis uses the UKF proposed in [34, 52] due to it increased accuracy and robustness, as demonstrated in [32]. If the probability distribution of a random vector undergoing a nonlinear transformation could be calculated, the MMSE optimal estimate could be obtained with the nonlinear model in the KF architecture. The optimal estimate is approximated up to a second-order term in the Taylor series expansion by the UKF [26].

A recursive Bayesian estimation algorithm has a two-stage filter architecture, and hence the UKF is also executed in the two-stage architecture. The two-stage UKF algorithms

for both the vehicle inertial parameter and the vehicle state identifications are presented in Appendix A.

3.7 Simulation Results

3.7.1 Vehicle Maneuver in Simulations

In order to generate the longitudinal and lateral dynamics, acceleration and double lane change (DLC) maneuvers are simulated in the vehicle simulation software, CarSim. All

Table 3.1: Vehicle Parameters [30] ©2014 IEEE

| Parameter	Value	Parameter	Value
$m_{s,emp}$	1274.0 $[kg]$	l	2.578 $[m]$
m_t	142.0 $[kg]$	$l_{f,emp}$	1.016 $[m]$
I_x	606.1 $[kgm^2]$	l_w	1.539 $[m]$
$I_{z,emp}$	1523.0 $[kgm^2]$	h_s	0.224 $[m]$
ρ	1.206 $[kg/m^3]$	k_ϕ	42075.0 $[kgm^2/s^2]$
A_f	1.6 $[m^2]$	c_ϕ	5737.5 $[kgm^2/s]$
C_d	0.15		

Table 3.2: Switch of Vehicle Inertial Parameter Identification (Simulation) [30] ©2014 IEEE

If
- Longitudinal Acceleration $(a_x) > 0.70 \ m/s^2$
- |Lateral Acceleration $(a_y)| < 0.25 \ m/s^2$
- |Yaw Rate $(\dot{\psi})| < 1 \ deg/s$
- |Front Wheel Steering Angle $(\delta^f)| < 0.52 \ deg$
- $\Rightarrow$ Then, m_a (longitudinal) estimation

Else If
- |Lateral Acceleration $(a_y)| > 0.25 \ m/s^2$
- |Yaw Rate $(\dot{\psi})| > 1 \ deg/s$
- $0.78 \ deg \ < $ |Front Wheel Steering Angle $(\delta^f)| < 8.31 \ deg$
- $\Rightarrow$ Then, l_f (lateral) estimation

Else
- $\Rightarrow$ Pause of the inertial parameter identification algorithm

End

the vehicle parameters used for the simulation are listed in Table 3.1. The path of the vehicle
is indicated as the solid line in Fig. 3.5a. The small box in Fig. 3.5a represents a vehicle,
and it follows the path. The maneuver performed in the simulation is: acceleration $\rightarrow$ DLC
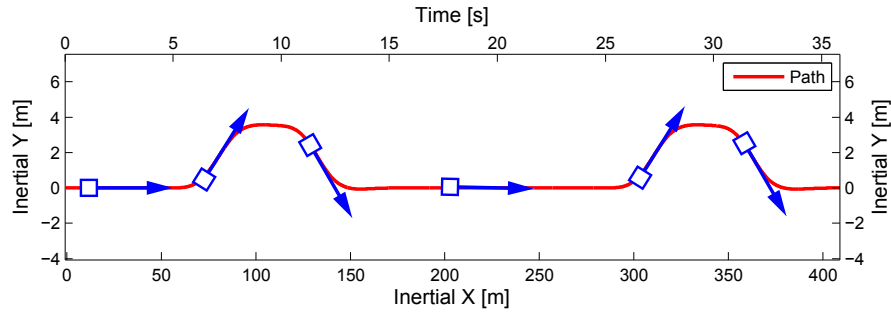
(a) Path of Vehicle
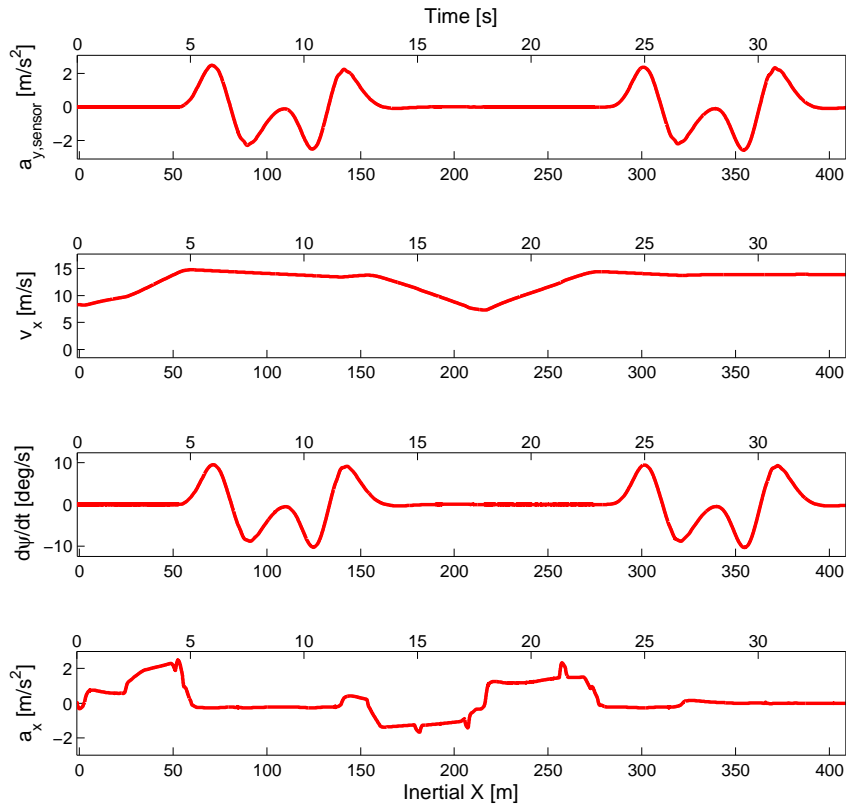
(b) Measurement d

Figure 3.5: Vehicle Maneuver in Simulation [30] ©2014 IEEE

$\rightarrow$ deceleration $\rightarrow$ acceleration $\rightarrow$ DLC on a flat road with a constant friction coefficient

0.8. The measurements during the maneuver are presented in Fig. 3.5b. The measurements $a_{y,sensor}$, v_x, $\dot{\psi}$, and a_x in Fig. 3.5b are corrupted with Gaussian noises with zero mean and variances of 0.0144, 0.0900, 0.0900, and 0.0144, respectively. The sampling time τ_s is 0.005 s.

The vehicle inertial parameter identification algorithm activates the estimation of the additional mass m_a under the prevailing longitudinal dynamics, whereas the estimation of the CoG position l_f is activated under the prevailing lateral dynamics. Otherwise, the algorithm pauses since the local observability of w is not ensured, as discussed in the *Local Observability Analysis* section. The estimation mode is switched based on the criteria presented in Table 3.2.

3.7.2 Estimation with a Point Mass

An estimation result of the inertial parameters, m_s, l_f, and I_z is presented in Fig. 3.6. In this simulation, a point mass 350 kg is added on the vehicle whose parameters are listed in Table 3.1. The point mass is located at the position of $l_a = 2.1$ m as shown in Fig. 3.6a, where l_a is the distance between the front axle and the CoG of the additional mass.
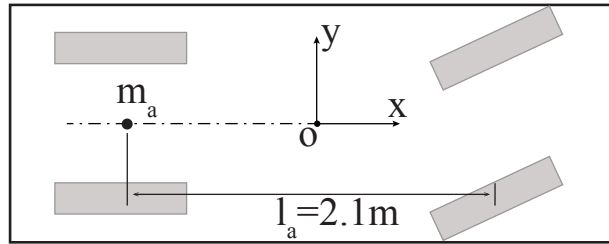
(a) Point Mass
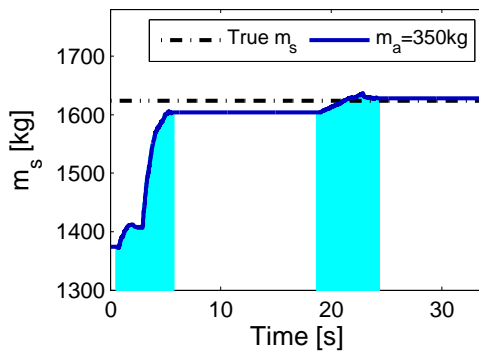
(b) Estimation of m_s
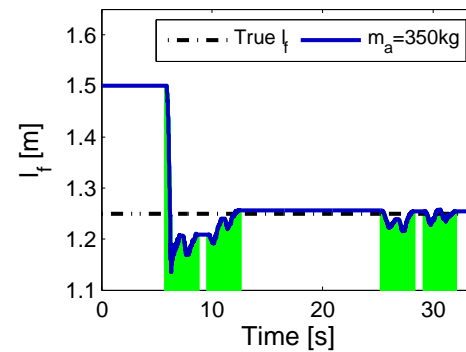
(c) Estimation of l_f

(d) Estimation of I_z

Figure 3.6: Identification with an Additional Point Mass [30] ©2014 IEEE

In Fig. 3.6b-3.6d, the horizontal dashed-dotted lines represent the true values of m_s, l_f,

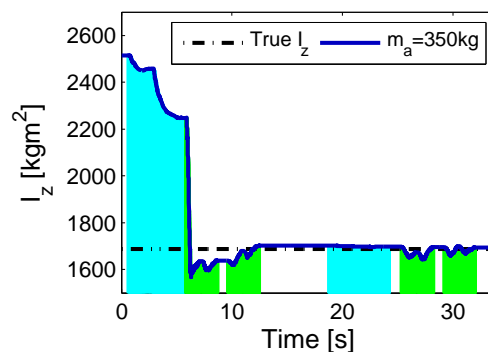and I_z, and the solid lines represent the estimations by the proposed algorithm. Once m_a is estimated, the sprung mass m_s in Fig. 3.6b is computed as $m_s = m_a + m_{s,emp}$. Note that the yaw moment of inertia I_z is calculated using the estimated m_a, l_f, and (3.23). According to the criteria in Table 3.2, the identification algorithm switches between the estimations for m_a and l_f. The shaded area in Fig. 3.6b represents the time period when the longitudinal dynamics prevail over the lateral dynamics to identify m_a, whereas that in Fig. 3.6c corresponds to the time period when the lateral dynamics predominate to identify l_f.

Monte Carlo simulations further illustrate the performance of the algorithm. The number of simulations is $N = 300$. The Gaussian noise is newly created for each trial, and is added to the measurements in Fig. 3.5b. At the end of each trial, e.g. about 34 s in Fig. 3.6, the percentage of the deviation from the true value is computed, and its statistics are presented in Fig. 3.7 with the mean value and the standard deviation σ.
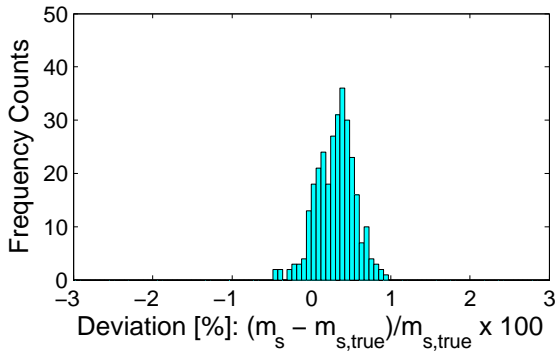
(a) m_s (mean: 0.3055%, σ: 0.2407%)
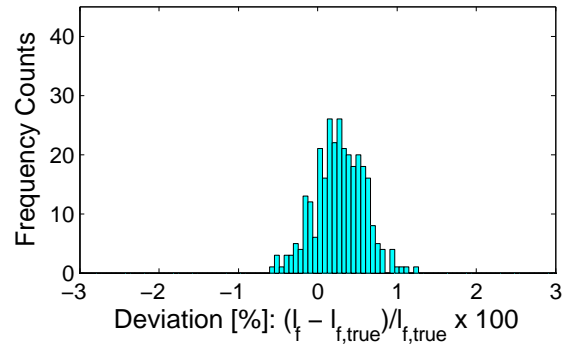
(b) l_f (mean: 0.2748%, σ: 0.3116%)
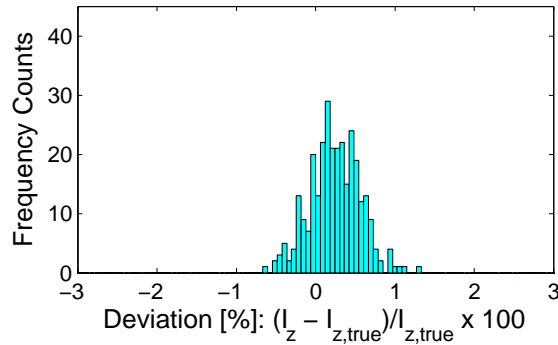
(c) I_z (mean: 0.2442%, σ: 0.3136%)

Figure 3.7: Monte Carlo Simulation ($N = 300$) with the Point Mass 350 kg [30] ©2014 IEEE

Note that there are biases of non-zero values, e.g. 0.31 % for m_s, for the mean values in Fig. 3.7. The vehicle and tire models used in the proposed algorithm do not perfectly describe

the high-fidelity vehicle and tire models in the CarSim. Therefore, the tire forces estimated
in the proposed algorithm can be different from those in the CarSim, which accounts for the
biased mean values.
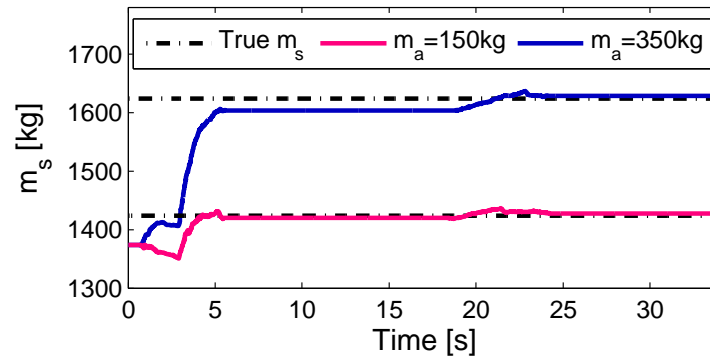
(a) Estimation of m_s
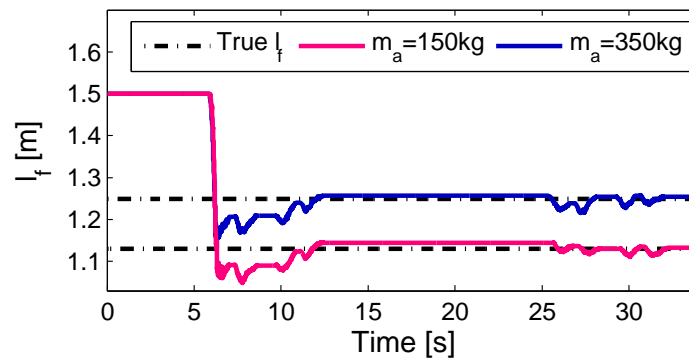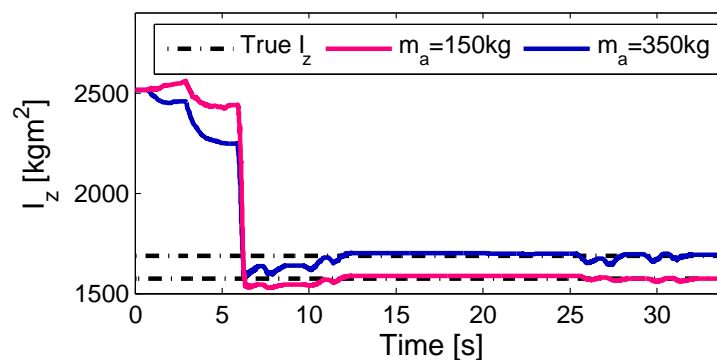
(b) Estimation of l_f

(c) Estimation of I_z

Figure 3.8: Identification with Different Point Additional Masses [30] ©2014 IEEE

The performance of the proposed identification algorithm is more clearly demonstrated

with the standard deviations. The deviation from true value is within ± 1 % with the standard deviation $\sigma = 0.24$ % for the sprung mass m_s, as shown in Fig. 3.7a. Fig. 3.7b and Fig. 3.7c also show the deviations from true values mostly within ± 1 % with small σ values, 0.31 % and 0.31 %, for l_f and I_z, respectively.

The primary goal of this research to differentiate two different m_a conditions is accomplished, as shown in Fig. 3.8. The additional mass m_a in Fig. 3.6a is changed from $350 kg$ to $150 kg$, and the location is the same, $l_a = 2.1$ m. The estimated inertial parameters, m_s, l_f, and I_z are smaller than those of the 350 kg additional mass, as shown in Fig. 3.8.

3.7.3 Estimation with a Box Mass

When deriving (3.23), an additional point mass is assumed. Acceptable estimation results,
however, are still obtained with an additional box mass by the proposed algorithm, as shown
in Fig. 3.9. The box mass (1 m × 1 m) is loaded on the empty vehicle as shown in Fig. 3.9a,
and the distance from the front axle to the CoG of the box mass is $l_a = 2.1$ m. The 350
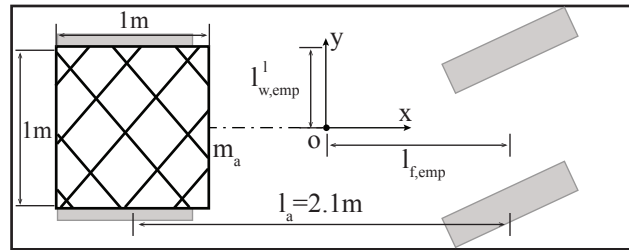
(a) Box Mass
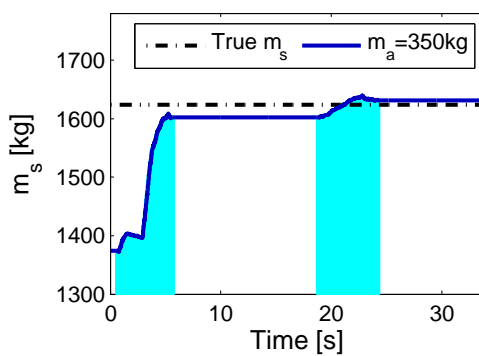
(b) Estimation of m_s
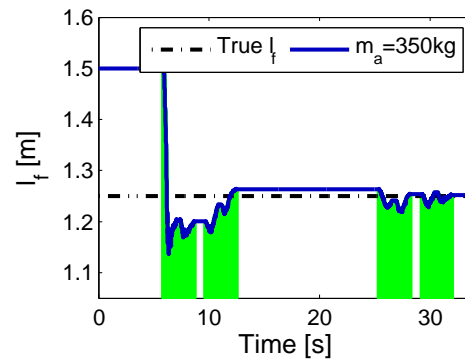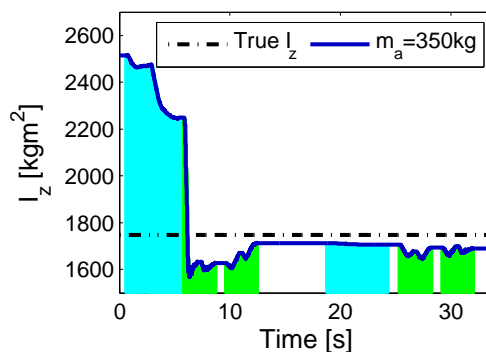
(c) Estimation of l_f

(d) Estimation of I_z

Figure 3.9: Identification with Additional Box Masses [30] ©2014 IEEE

kg box mass has the yaw moment of inertia, 58.33 kgm^2, with respect to its own centroid.

Due to the centroidal yaw moment of inertia, the estimates of I_z have discrepancies from
the true values of I_z, as shown in Fig. 3.9d. The discrepancy, however, is small, compared
to the total I_z of the vehicle.

Fig. 3.10 presents Monte Carlo simulations carried out with the 350 kg additional box
mass. The precision of the algorithm is not degraded by the additional box mass in the
$N = 300$ simulations; the standard deviations are small values, 0.25 %, 0.34 %, and 0.30
%, for m_s, l_f, and I_z, respectively. Because the additional box mass has a centroidal yaw
moment of inertia of 58.33 kgm^2, Fig. 3.10c shows more biased mean values than those of
the point mass in Fig. 3.7c. All the deviations of I_z estimates, however, are still within ± 5
%.

(a) m_s (mean: 0.4960%, σ: 0.2492%)   (b) l_f (mean: 0.4813%, σ: 0.3110%)

(c) I_z (mean: -2.9200%, σ: 0.3043%)
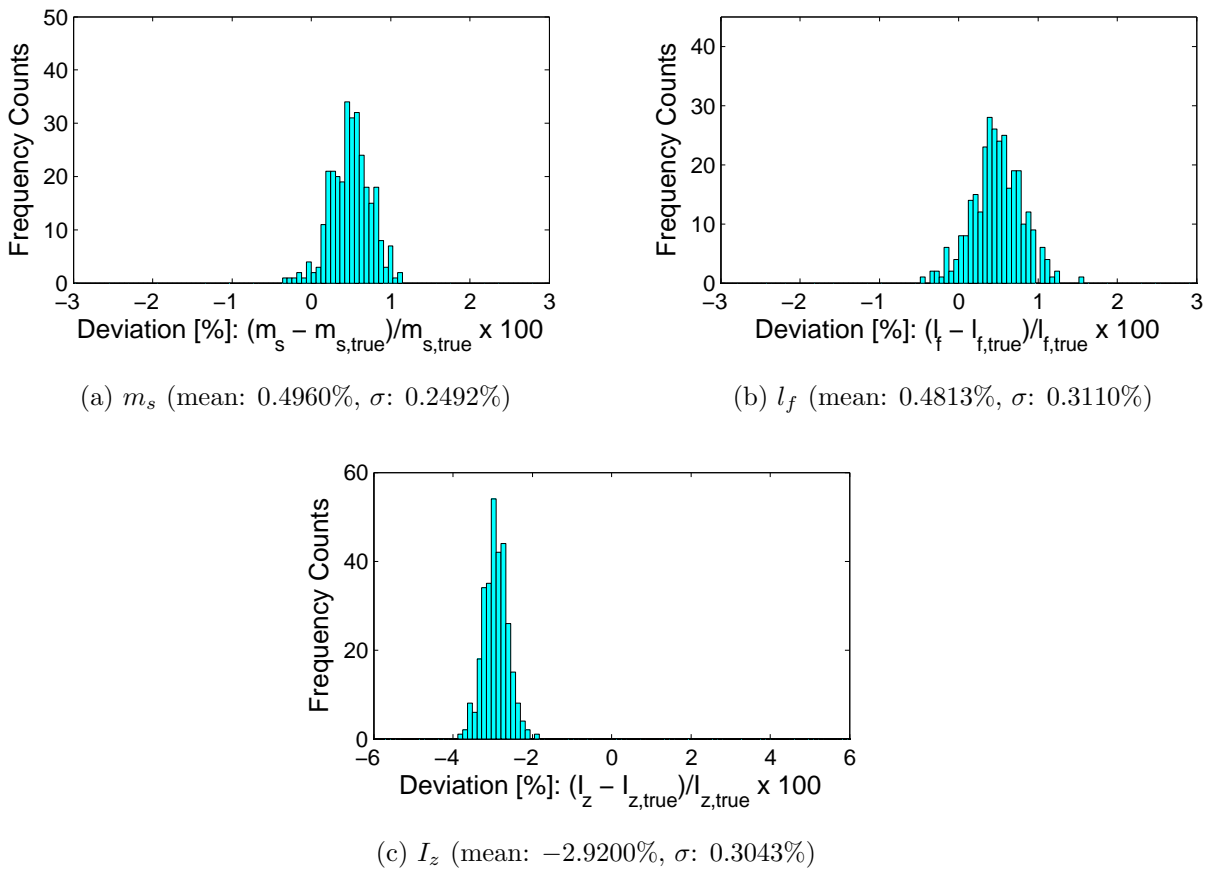
Figure 3.10: Monte Carlo Simulation ($N = 300$) with the Box(1 m $\times$ 1 m) Mass 350 kg [30]
©2014 IEEE

Different box (1 m $\times$ 1 m) additional mass conditions are differentiated with the proposed
algorithm, as shown in Fig. 3.11. The additional mass m_a in Fig. 3.9a is changed from 350
kg to 150 kg, and the location is the same, $l_a = 2.1$ m. As shown in Fig. 3.11, the estimated
inertial parameters, m_s, l_f, and I_z are smaller than those of the 350 kg additional mass. Due

to the centroidal yaw moment of inertia, Fig. 3.11c shows discrepancies between the true I_z and the estimated I_z for both 150 kg and 350 kg. However, the yaw moment of inertia I_z for 150 kg and 350 kg is still differentiated with the proposed identification algorithm.
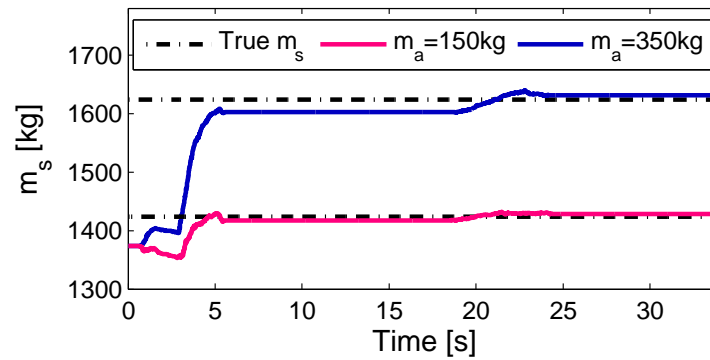
(a) Estimation of m_s
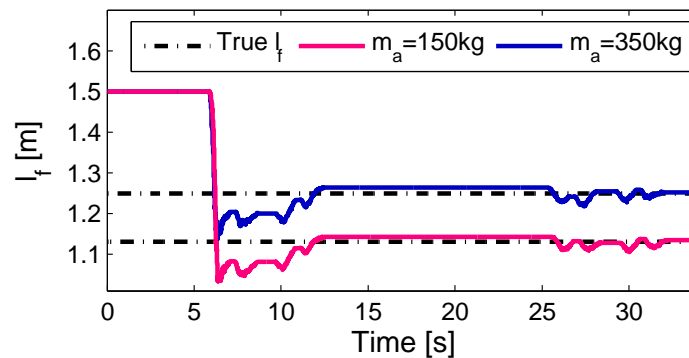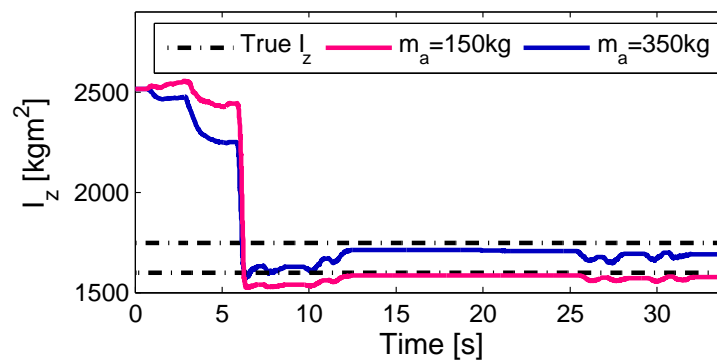
(b) Estimation of l_f

(c) Estimation of I_z

Figure 3.11: Identification with Different Box Additional Masses [30] ©2014 IEEE

3.7.4 Robustness of the Algorithm

The noise covariance matrices have influence on the identification, and it is examined with a point mass of 350 kg. In Fig. 3.12, R^r and R^e denote the covariance matrices of the process noise r in (3.16) and the measurement noise e in (3.17), respectively. While the process noise

(a) Covariance Matrix R^r (b) Covariance Matrix R^e
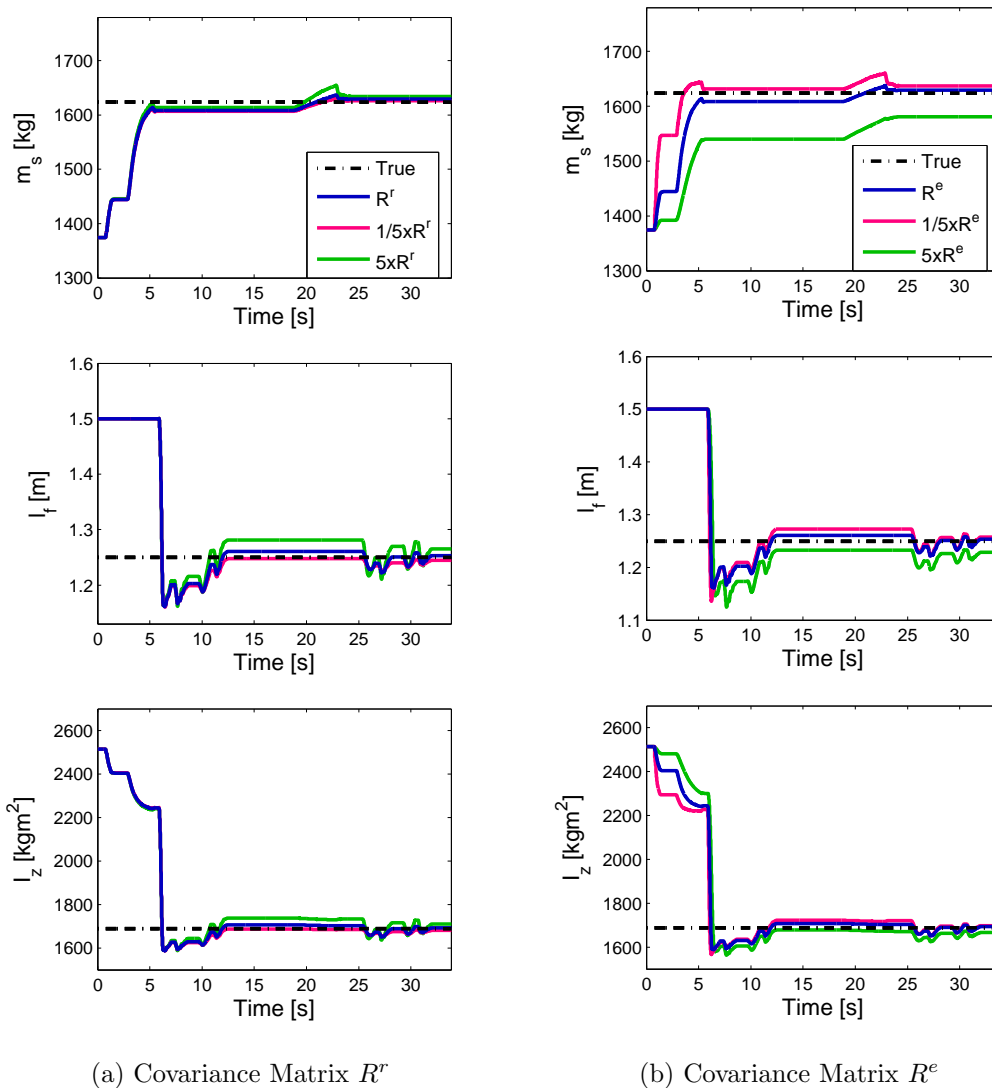
Figure 3.12: Identification with Different Covariance Matrices [30] ©2014 IEEE

covariance matrices (R^r, $1/5R^r$, and $5R^r$) are used for estimation in Fig. 3.12a, estimation results with the measurement noise covariance matrices (R^e, $1/5R^e$, and $5R^e$) are presented in Fig. 3.12b. As shown in Fig. 3.12a, the proposed algorithm converges to similar values

in all cases, although the process noise covariance matrix, R^r, affects the convergence rate and the extent of chatter [26]. In Fig. 3.12b, as R^e increases, the algorithm converges more conservatively, i.e. the corrective action is attenuated. This is because the large R^e implies that the measurements are less trustworthy.

3.8   Experimental Results

3.8.1   Experimental Setup

Experiments were conducted at the *Richmond Field Station* with the support by the *Hyundai-Kia Motor Company*. The test vehicle, an Azera V6 3.3L, is equipped with standard vehicle sensors, e.g. accelerometers, a gyroscope, a steering wheel angle sensor, and wheel speed sensors. The measurement data from the vehicle sensors are transmitted via the Controller Area Network (CAN) bus.
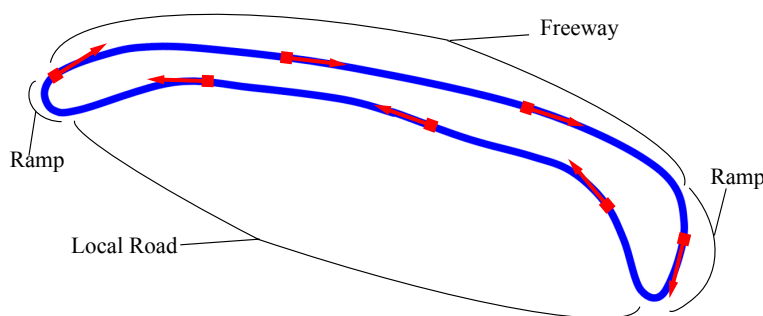
Figure 3.13: [Exp.] Experimental Course [30] ©2014 IEEE

Fig. 3.13 presents the course used for the experimental tests. The test vehicle executes acceleration and deceleration multiple times on a local road. Then, it travels on a curved ramp interconnecting the local road and a freeway. The test vehicle accelerates again on the straight section of the freeway. Both the local road and the freeway are asphalt pavements. This experimental driving was conducted for 3 laps, which lasts about 500 s. Note that the road bank and road grade angles are neglected. The 200 kg additional box mass was loaded in the trunk. The measurements during the experiment are shown in Fig. 3.14. The sampling time τ_s is 0.01 s.

The criteria presented in Table 3.3 are used to switch between the estimation of m_a and the estimation of l_f. Note that the 4th-gear is used to activate the m_a estimation. The large gear ratio by the lower gear can generate a large change in the acceleration a_x, which discourages the m_a estimation compared to the constant acceleration maneuver. Furthermore, the torque converter lockup rarely occurs if the lower gears are used.

Note that an additional signal processing is used for the experimental tests to obtain smoother identification results. The m_s estimation, dashed line in Fig. 3.15, chatters a lot due to noise and unmodeled dynamics. In Fig. 3.15, the vertical lines represent the time periods when the longitudinal dynamics prevail over the lateral dynamics to identify m_a. In order to obtain the smoother estimation results, various filtering techniques, such as a moving average filter and Recursive Least Squares (RLS) filter, can be applied.

A filter which minimizes the squared errors, such as the RLS (see [25]), is used to obtain the smoother estimation results. Note that the filter is based on the assumption that a given
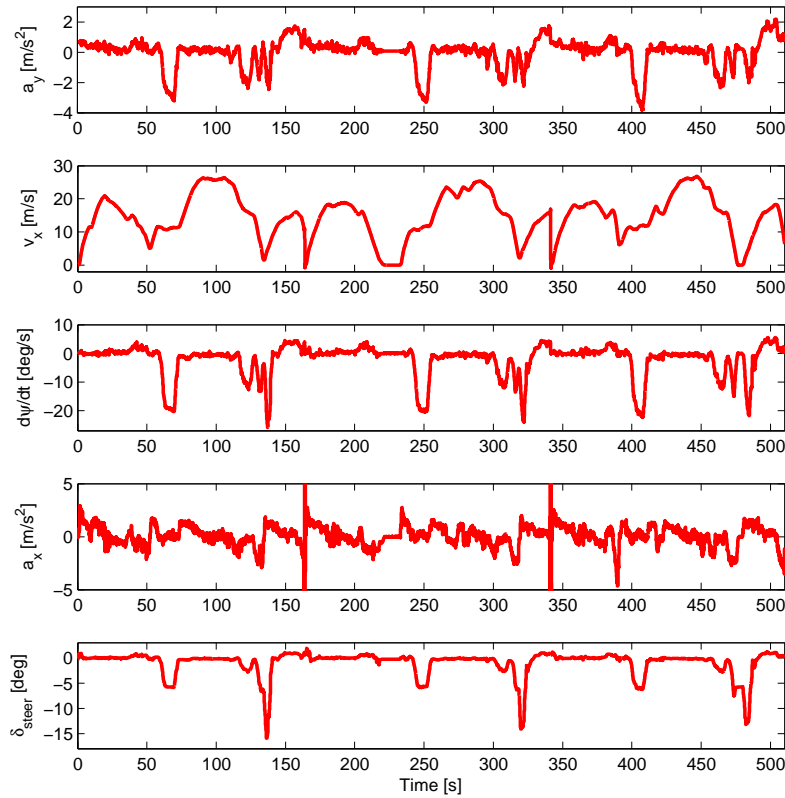
Figure 3.14: [Exp.] Measurements with Additional Mass (200 kg) [30] ©2014 IEEE

data set is normally distributed. This filter is implemented by the Kalman Filter (KF) (see
[15]) that uses the state-space model written as:

$$\bar{w}(k) = \bar{w}(k-1) \tag{3.27}$$

$$\bar{d}(k) = w_{UKF}(k) = \bar{w}(k) + \bar{e}(k). \tag{3.28}$$

The KF is a linear estimator to minimize the mean of the squared errors with normal
distribution (see [15]). Note that the identity state transition and output matrices are used
in the state-space model in (3.27)-(3.28), and the process noise is not included in the state
dynamics in (3.27). Fig. 3.15 illustrates the importance of the proposed filtering. The dashed
line in Fig. 3.15 is indicated as $w_{UKF}(k)$, which is the measurement vector for the system
in (3.27)-(3.28). The solid line in Fig. 3.15 represents the estimate of $\bar{w}(k)$ in (3.27)-(3.28)
after the proposed processing. The noise $\bar{e}$ in (3.28) is assumed to be white, stationary, and
normally distributed with zero mean.

Table 3.3: Switch of Vehicle Inertial Parameter Identification (Experiment) [30] ©2014 IEEE

If
- 4th-Gear & No Gear Change
- Lockup
- $0.70 \ m/s^2 <$ Longitudinal Acceleration $(a_x) < 1.50 \ m/s^2$
- |Lateral Acceleration $(a_y)| < 0.3 \ m/s^2$
- |Yaw Rate $(\dot{\psi})| < 1.5 \ deg/s$
- |Front Wheel Steering Angle $(\delta^f)| < 0.62 \ deg$
- $\Rightarrow$ Then, m_a (longitudinal) estimation

Else If
- No Brake
- |Lateral Acceleration $(a_y)| > 0.3 \ m/s^2$
- |Yaw Rate $(\dot{\psi})| > 1.5 \ deg/s$
- Longitudinal Acceleration $(a_x) < 0.25 \ m/s^2$
- Longitudinal Velocity $(v_x) > 8.3333 \ m/s$
- $0.9438 \ deg <$ |Front Wheel Steering Angle $(\delta^f)| < 3.1460 \ deg$
- $\Rightarrow$ Then, l_f (lateral) estimation

Else
- $\Rightarrow$ Pause of the inertial parameter identification algorithm

End
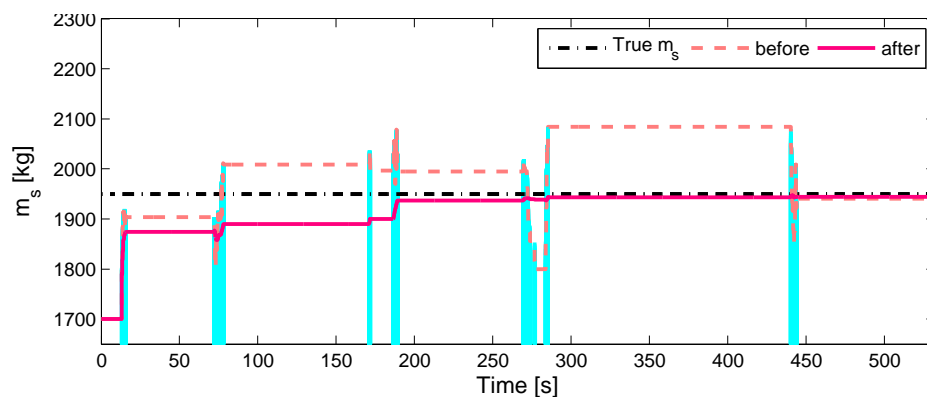
Figure 3.15: [Exp.] Estimation of m_s with Additional Mass (0 kg) [30] ©2014 IEEE

3.8.2 Estimation Results

As shown in Fig. 3.16, the measurements without the additional mass is first used for the inertial parameter identification algorithm. Due to the lack of the equipment to measure the position of the CoG and the yaw moment of inertia, the true l_f and I_z are approximately
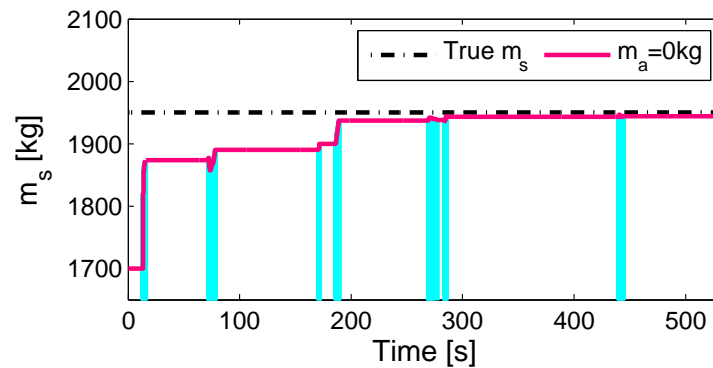
(a) Estimation of m_s
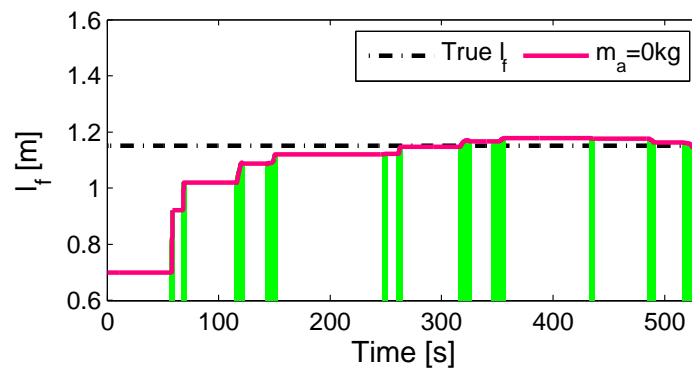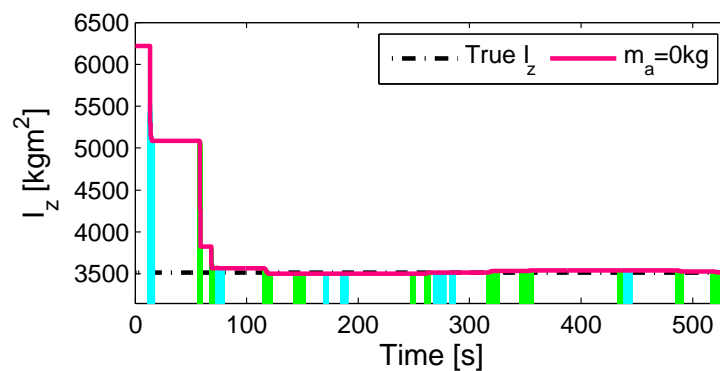
(b) Estimation of l_f

(c) Estimation of I_z

Figure 3.16: [Exp.] Identification with Additional Mass (0 kg) [30] ©2014 IEEE

calculated. The vertical lines in Fig. 3.16a represent the time periods when the longitudinal dynamics prevail over the lateral dynamics to identify m_a, whereas those in Fig. 3.16b represent the time instants when the lateral dynamics predominate to identify l_f. The m_a estimator is activated for 14.47 s in Fig. 3.16a, and the estimator for l_f is activated for 27.65
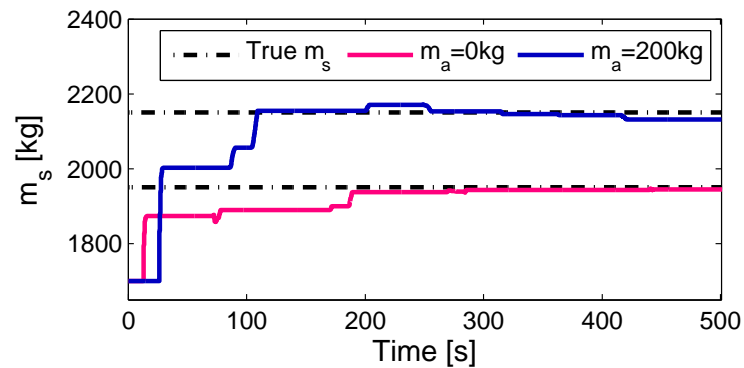
(a) Estimation of m_s
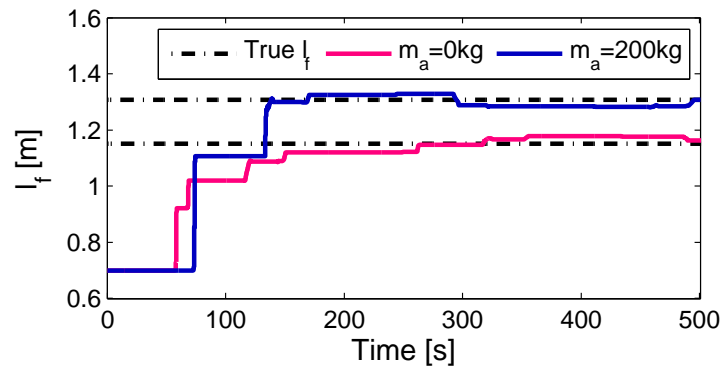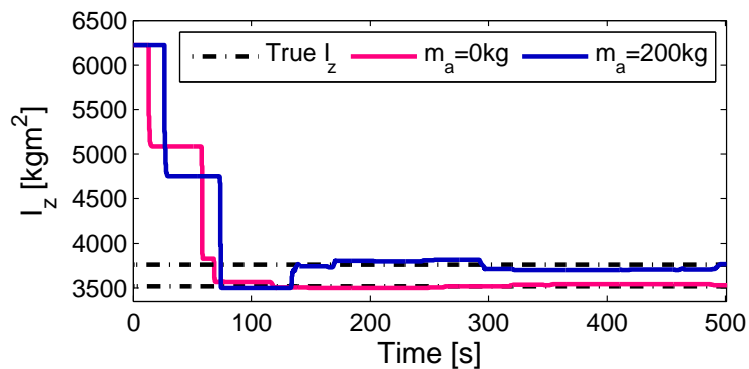
(b) Estimation of l_f

(c) Estimation of I_z

Figure 3.17: [Exp.] Identification with Different Additional Masses (0 kg and 200 kg) [30]
©2014 IEEE

s in Fig. 3.16b. Since the local observability of the inertial parameter w is not ensured, the
identification algorithm pauses for the rest of the time.

Fig. 3.17 presents the identification results with the 200 kg additional mass in the trunk. The inertial parameter estimates using the 200 kg additional mass are different from those using the 0 kg additional mass. The experimental tests are repeated three times for each value of m_a case, and Fig. 3.18 shows the overall identification results. While the upper dashed-dotted horizontal lines indicate the approximated true values for 200 kg, the lower dashed-dotted horizontal lines indicate those for 0 kg. Uncertainties in real world result in some discrepancies from the true values for both 0 kg and 200 kg. The proposed identification algorithm, however, distinguish the two cases of 0 kg and 200 kg for all the experimental tests. Particularly, the I_z estimates for 0 kg and 200 kg are clearly distinguishable in Fig. 3.18.
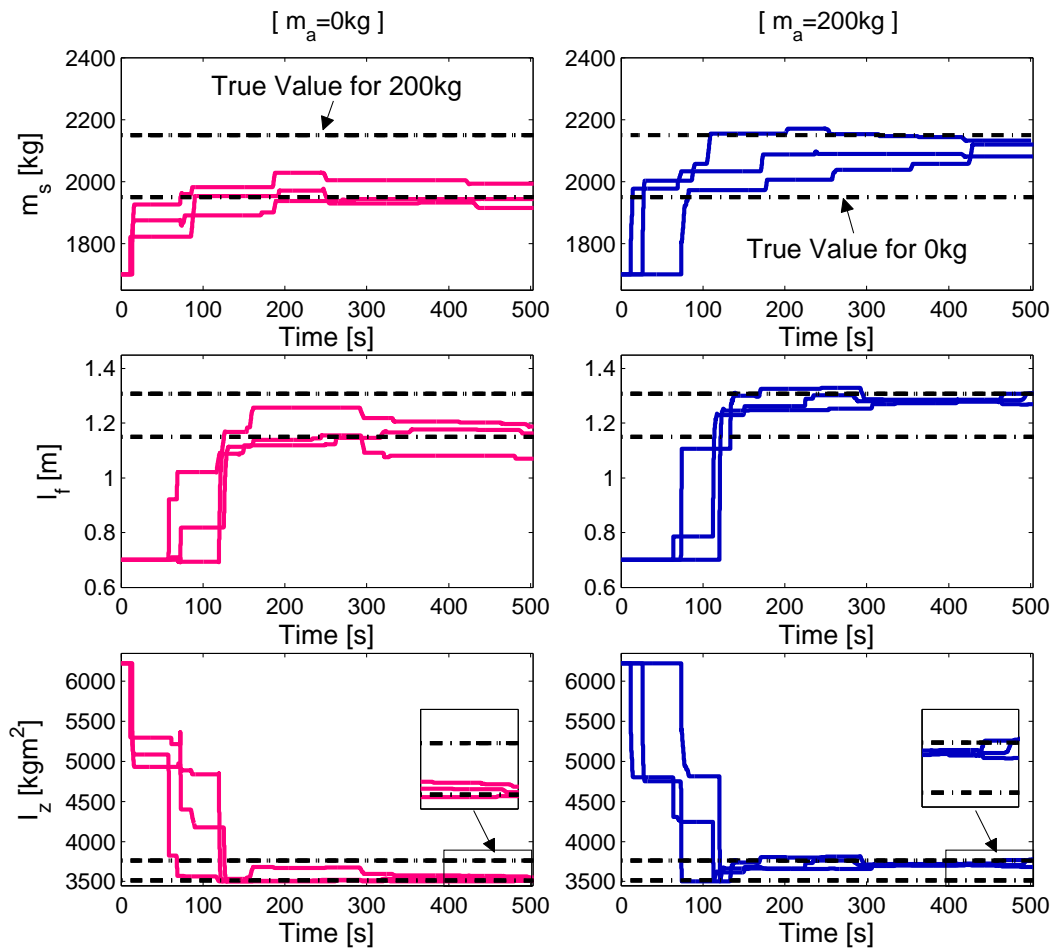
Figure 3.18: [Exp.] Repetitive Identification with Different Additional Masses (0 kg and 200 kg) [30] ©2014 IEEE

3.9   Conclusion

This chapter proposes an identification algorithm for vehicle inertial parameters: a vehicle sprung mass, longitudinal position of the CoG, and yaw moment of inertia. The proposed algorithm uses the correlation between the inertial parameters and the dual unscented Kalman filter. The extensive CarSim simulations and the experimental tests illustrate that the algorithm is capable of differentiating two additional mass conditions on a flat road with a constant friction coefficient.

Chapter 4

Optimal Control based on Roll Prediction for Safe Path Following

4.1   Introduction

This thesis develops a control algorithm to combine autonomous vehicles with rollover prevention systems. That is, the proposed controller aims to follow a curved path achieving the required yaw rate while simultaneously preventing rollover. Roll motion is minimized throughout cornering by applying a receding horizon optimal control technique. Compared to other rollover prevention controllers that only respond to imminent rollover, the proposed controller reduces possibility of rollover more aggressively.

A four-wheel vehicle model with roll dynamics is utilized to predict the roll motion during cornering, which is included in a cost function of the optimal control formulation. Using the roll motion prediction enables the controller to preemptively respond to future roll motion. If differential braking operates to prevent rollover, a vehicle cannot follow a curved path due to the counter yaw moment generated by the differential braking. Therefore, full braking is used as a control actuator. However, excessive reduction of vehicle speed should also be avoided since it can possibly cause rear-end collisions by cars following on a freeway. The proposed algorithm is incorporated with the vehicle inertial parameter estimator and the state estimator developed in Chapter 3. The performance of the proposed algorithm is verified with simulations. Note that some contents of this chapter are submitted to a conference [28].

4.2   Vehicle Model

The four-wheel vehicle model with roll dynamics is used in this chapter. This vehicle model has been presented in Chapter 3, and therefore equations for the model are briefly reviewed here; refer to Chapter 3 for details.

Four degrees of freedom are considered in the vehicle model: longitudinal (x) and lateral (y) translational motion, yaw (ψ) rotation about the z-axis, and roll (ϕ) rotation about the x-axis, as shown in Fig. 3.1. Define the state vector of the vehicle model as $s := [s_1,\ s_2,\ s_3,\ s_4,\ s_5]^\top = [v_x,\ v_y,\ \dot\psi,\ \phi,\ \dot\phi]^\top$. The state-space dynamics model is presented in (3.1)-(3.5) as follows:

$$
\begin{aligned}
\dot s_1 = \dot v_x &= a_x + v_y\dot\psi\\
\dot s_2 = \dot v_y &= a_y - v_x\dot\psi\\
\dot s_3 = \ddot\psi &= \frac{1}{I_z}\left\{l_w(F_x^{fr} + F_x^{rr}) - l_w^l F_x\right.\\
&\qquad\left. + l_f F_y - l(F_y^{rl} + F_y^{rr})\right\}\\
\dot s_4 = \dot\phi &= \dot\phi\\
\dot s_5 = \ddot\phi &= \frac{1}{I_x}\left\{m_s h_s(a_y + g\phi) - k_\phi\phi - c_\phi\dot\phi\right\}.
\end{aligned}
$$

The tire forces at the ith wheel in the vehicle longitudinal (x) and lateral (y) directions are denoted as F_x^i and F_y^i, respectively. Then, the vector u is defined as follows:

$$
u := [\{F_x^i\}_{i\in\mathcal{I}},\ \{F_y^i\}_{i\in\mathcal{I}}]^\top,
$$

where $\mathcal{I} = \{fl,\ fr,\ rl,\ rr\}$ is a set indicating front-left, front-right, rear-left, and rear-right wheels.

The vehicle longitudinal acceleration a_x in (3.1) and lateral acceleration a_y in (3.2) are:

$$
\begin{aligned}
a_x &= \frac{F_x - F_{aero}}{m}\\
a_y &= \frac{F_y}{m},
\end{aligned}
\tag{4.1}
$$

where $F_x = \sum_{i\in\mathcal{I}}\{F_x^i\}$ and $F_y = \sum_{i\in\mathcal{I}}\{F_y^i\}$ are the total vehicle longitudinal and lateral forces, respectively. The aerodynamic drag force F_{aero} is modeled as $F_{aero} = \frac{1}{2}\rho C_d A_f v_x^2$. The total vehicle mass is denoted as m, and it is the sum of the sprung mass m_s and the mass of all wheels m_t, i.e. $m = m_s + m_t$.

The measurement vector d consists of the lateral acceleration $a_{y,sensor} = a_y - h_{acc}\ddot\phi - g\phi$, the longitudinal velocity v_x, the yaw rate $\dot\psi$, and the longitudinal acceleration a_x:

$$
\begin{aligned}
d &:= \left[a_{y,sensor},\ v_x,\ \dot\psi,\ a_x\right]^\top\\
&= G(s,\ \dot s) = \begin{bmatrix} \dot s_2 + s_1 s_3 - h_{acc}\dot s_5 - g s_4\\ s_1\\ s_3\\ \dot s_1 - s_2 s_3 \end{bmatrix},
\end{aligned}
$$

where $h_{acc} = h_s$ is assumed.

The above equations are compactly written as the continuous state-space model:

$$\begin{aligned} \dot{s}(t) &= F(s(t),\ u(t)) \\ d(t) &= G(s(t),\ \dot{s}(t)). \end{aligned}$$

Using Euler forward discretization, the discretized state-space representation is:

$$\begin{aligned} s(k+1) &= s(k) + \tau_s F(s(k),\ u(k)) \\ &= T(s(k),\ u(k)) \\ d(k) &= G(s(k),\ \dot{s}(k)), \end{aligned}$$

where τ_s is the sampling time. Note that the inertial parameter vector w and the noise terms in Chapter 3 are not included in the above state-space model.

4.3 Tire Forces

The vehicle longitudinal and lateral forces at the ith wheel, F_x^i and F_y^i, are calculated with the tire longitudinal and lateral forces, F_l^i and F_c^i, as follows (see Fig. 3.2):

$$\begin{aligned} F_x^i &= F_l^i \cos \delta^i - F_c^i \sin \delta^i,\ (i \in \mathcal{I}) & (4.2) \\ F_y^i &= F_l^i \sin \delta^i + F_c^i \cos \delta^i,\ (i \in \mathcal{I}), & (4.3) \end{aligned}$$

where δ^i denotes the steering angle of the ith wheel. Note that the steering angles of the rear wheels are zero.

4.3.1 Tire Lateral Force

The tire lateral force F_c is estimated through the tire brush model. This section has also been presented in the previous chapter, and therefore equations for F_c are briefly reviewed here; refer to Chapter 3 for details.

The tire lateral force F_c^i on the ith wheel is:

$$F_c^i = \mu F_z^i \{1 - (1 - \theta_y^i |\sigma_y^i|)^3\} sgn(\alpha_s^i),$$

where F_z^i represents the normal force at the ith wheel, μ is a known tire-road friction coefficient, the composite tire model parameter is defined as $\theta_y^i := \frac{2c_{py}(a^i)^2}{3\mu F_z^i}$, and a^i is the half length of the tire-road contact patch. The half length a^i is estimated with the following relationship:

$$a^i = \sqrt{(r_{unload}^i)^2 - (r_{unload}^i - \frac{F_z^i}{c_{rad}})^2},$$

where c_{rad} is a known tire radial stiffness, and r_{unload} is an unloaded tire radius. Note that a^i of the front tire is assumed to be a constant. The lateral tire slip σ_y^i is defined as:

$$\sigma_y^i \quad := \quad \tan \alpha_s^i.$$

The tire slip angle α_s^i is computed as $\alpha_s^i = \delta^i - \delta_{wheel}^i$, where δ^i is the steering angle, and δ_{wheel}^i indicates the wheel velocity angle. The wheel velocity angle δ_{wheel}^i is estimated by using the vehicle state s as follows:

$$\delta_{wheel}^i \quad = \quad \tan^{-1} \left(\frac{v_y + \bar{l}^i \dot{\psi}}{\bar{v}_x^i} \right)$$

$$\bar{l}^i \quad = \quad \begin{cases} l_f & (i = fl, \ fr) \\ l_f - l & (i = rl, \ rr) \end{cases}$$

$$\bar{v}_x^i \quad = \quad \begin{cases} v_x - \dot{\psi} \cdot l_w^l & (i = fl, \ rl) \\ v_x + \dot{\psi}(l_w - l_w^l) & (i = fr, \ rr). \end{cases}$$

4.3.2 Tire Longitudinal Force

In the proposed control algorithm, a control actuator is full braking. Full braking is implemented by calculating a desired vehicle longitudinal acceleration a_x. The tire longitudinal force F_l is estimated by using the tire lateral force F_c and the desired a_x, as will be discussed in the *Design of Optimal Controller* section.

4.3.3 Normal Force

Again, equations for the normal force are briefly reviewed here; refer to Chapter 3 for details. The sprung mass m_s and the longitudinal acceleration a_x generate the normal force distribution on the front and rear tires as f_z^f and f_z^r:

$$f_z^f \quad = \quad m_s \frac{l - l_f}{l} g - m_s h_s a_x$$

$$f_z^r \quad = \quad m_s \frac{l_f}{l} g + m_s h_s a_x.$$

The lateral distribution of f_z^i is denoted as $\bar{f}_z^i$:

$$\bar{f}_z^i \quad = \quad \begin{cases} \frac{l_w - l_w^l}{l_w} f_z^f \ (\text{for } i = fl), & \frac{l_w^l}{l_w} f_z^f \ (\text{for } i = fr) \\ \frac{l_w - l_w^l}{l_w} f_z^r \ (\text{for } i = rl), & \frac{l_w^l}{l_w} f_z^r \ (\text{for } i = rr). \end{cases}$$

Then, the total normal forces including the load transfer are derived as follows:

$$F_z^i = \begin{cases} \bar{f}_z^i - k_s l_w^l \phi - c_s l_w^l \dot{\phi}, \ (i = fl, \ rl) \\ \bar{f}_z^i + k_s(l_w - l_w^l)\phi + c_s(l_w - l_w^l)\dot{\phi}, \ (i = fr, \ rr), \end{cases}$$

where k_s and c_s represent known suspension stiffness and damping, respectively.

4.4 Design of Optimal Controller

4.4.1 Objective of the Controller

Following a curved path while simultaneously preventing rollover is the objective of the
controller. If a controller only takes an action when rollover is imminent, then an actuator
with a very fast response speed is required. Therefore, this thesis proposes to minimize roll
motion throughout cornering, which ensures maximal safety against rollover. Full braking is
utilized as a control actuator, and it is implemented by calculating the desired longitudinal
acceleration a_x. Differential braking precludes following a curved path since it degrades
yaw rate [12]. Note that excessive reduction in the vehicle speed should be avoided since
dangerous rear-end collisions can be caused by the excessive reduction of vehicle speed.

4.4.2 Design of Controller

In the design of the controller, a receding horizon optimal control, also known as Model
Predictive Control (MPC), is used. At time step k, the roll motion is predicted using the
current vehicle state $s(k)$. In other words, $\{\phi(k+j|k)\}_{j=0}^{N}$ is computed using $s(k)$ and
the vehicle model, where $\phi(k+j|k)$ represents the roll angle $\phi(k+j)$ predicted at time k
and N represents a time horizon. This prediction is repeatedly performed afterward using
the vehicle state s at time $k+1$, $k+2$, $\cdots$. Note that the novel algorithm based on the
Unscented Kalman Filter (UKF) in Chapter 3 is used for the estimation of the vehicle state
s (see Chapter 3 for details).

The MPC solves the following constrained optimal control problem at every time step:

$$\min_{\Phi} \quad \beta_\phi \sum_{j=N_s}^{N} |\phi(k+j|k)|^2 + \beta_{a_x} \sum_{j=N_s}^{N} |a_x(j)|^2 + \beta_{v_x} |v_x(k+N|k) - v_{x,e}|^2 \tag{4.4a}$$

$$\text{subj. to} \quad \begin{bmatrix} v_x(k+j+1|k) \\ \phi(k+j+1|k) \end{bmatrix} = C \ T(s(k+j|k), \ u(k+j|k)), \tag{4.4b}$$

$$\text{where } C = \begin{bmatrix} 1\ 0\ 0\ 0\ 0 \\ 0\ 0\ 0\ 1\ 0 \end{bmatrix}$$

$$u(k+j|k) = [\{F_x^i(k+j|k)\}_{i \in \mathcal{I}}, \ \{F_y^i(k+j|k)\}_{i \in \mathcal{I}}]^\top \tag{4.4c}$$

$$a_x^{lb} \leq a_x(j) \leq a_x^{ub} \tag{4.4d}$$

$$j = 0, \ 1, \ \cdots, \ N-1$$

$$|\phi(k+N|k)| \leq \phi^b \tag{4.4e}$$

$$\Phi = [a_x(0), \cdots, a_x(N-1)]^\top \tag{4.4f}$$

$$v_{x,e} : \text{entry speed.} \tag{4.4g}$$

Note that the above problem is formulated for time step k. The prediction of roll angle $\phi(k+j|k)$ is included in the cost function (4.4a). The magnitude of longitudinal acceleration $|a_x(j)|$

in the cost function restrains abrupt braking. In addition, $v_{x,e}$ indicates the longitudinal
velocity when a vehicle enters a curved road. The criteria to be listed in the *Simulation
Results* section are used to detect when the vehicle enters the curved road. Excessive speed
reduction, which can induce dangerous rear-end collisions, is avoided with the difference
between the predicted $v_x(k + N|k)$ and the entry speed $v_{x,e}$, i.e. $|v_x(k + N|k) - v_{x,e}|$. In
the cost function, β_ϕ, β_{a_x}, and β_{v_x} represent weights. Note that the cost function includes
the prediction from the time step $j = N_s$ to $j = N$ discarding the prediction from the time
step $j = 0$ to $j = N_s - 1$. It takes some time lag to generate the roll angle ϕ after feeding
the control input a_x. Therefore, the effect of different a_x on the cost value is more clearly
observed by using the tail of prediction, $\phi(k+N_s|k)$, $\cdots$, $\phi(k+N|k)$ than all the predictions,
$\phi(k|k)$, $\cdots$, $\phi(k + N|k)$. This approach facilitates an optimization solver to converge to a
solution.

The vehicle longitudinal force $\{F_x^i(k + j|k)\}_{i\in\mathcal{I}}$ and the vehicle lateral force $\{F_y^i(k +
j|k)\}_{i\in\mathcal{I}}$ constitute the vector $u(k + j|k)$ in (4.4c). If an optimization solver assigns a value
to $a_x(j)$, which is the decision variable in the above problem, F_x^i is computed with (4.1) as
follows:

$$F_x^i(k + j|k) = \frac{1}{4}\{ma_x(j) + \frac{1}{2}\rho C_d A_f s_1(k + j|k)^2\}, \tag{4.5}$$

where $i \in \mathcal{I}$. The total vehicle longitudinal force F_x is assumed to be equally exerted on the
four wheels, and hence (4.5) includes $\frac{1}{4}$. The tire lateral force F_c^i is estimated through the
tire brush model as presented in the previous section. Therefore, (4.2) and (4.5) yield the
tire longitudinal force F_l^i corresponding to $a_x(j)$ as follows:

$$F_l^i(k + j|k) = \frac{1}{\cos \delta^i(k)}\{F_x^i(k + j|k) + F_c^i(k + j|k) \sin \delta^i(k)\}. \tag{4.6}$$

A driver model, e.g. [22], can be used to predict the steering angle on a curved road.
The proposed algorithm, however, assumes constant steering angle $\delta^i(k)$ over the prediction
horizon $j = 0$, $\cdots$, N for simplicity: $\delta^i(k) = \delta^i(k|k) = \cdots = \delta^i(k + N|k)$. Next, F_y^i in (4.4c)
is calculated using (4.3) and (4.6):

$$F_y^i(k + j|k) = F_l^i(k + j|k) \sin \delta^i(k) + F_c^i(k + j|k) \cos \delta^i(k). \tag{4.7}$$

Then, (4.5) and (4.7) comprise the vector $u(k + j|k)$ in (4.4c).

A lower bound a_x^{lb} and an upper bound a_x^{ub} constrain the longitudinal acceleration $a_x(j)$
in the above optimal control problem. Note that the constant a_x over the prediction horizon,
i.e. $a_x = a_x(0) = \cdots = a_x(N)$, is used in order to relieve computational burden. Note that
an inequality constraint is imposed on $|\phi(k + N|k)|$ as a threshold of rollover.

Once the above constrained optimal control problem yields the desired a_x, the desired
longitudinal velocity $v_x^{des}(k)$ is calculated as:

$$v_{x,des}(k) = v_x(k) + \tau_s a_x. \tag{4.8}$$

The low-level speed controller in the simulation software tracks the desired velocity $v_{x,des}$.

4.5 Simulation Results - without Parameter Identification

In this section, the performance of the proposed controller is illustrated with simulations assuming vehicle inertial parameters are known.

4.5.1 Vehicle Maneuver in Simulations

As shown in Fig. 4.1, a curved road of radius 100 m is used for simulations in the vehicle simulation software, CarSim. The vehicle starts from the inertial position of (0, 0) in Fig. 4.1 by moving straight, and finishes driving at the same position. All the vehicle parameters used for the simulation are listed in Table 4.1.

Table 4.1: Vehicle Parameters [28] ©2014 IEEE

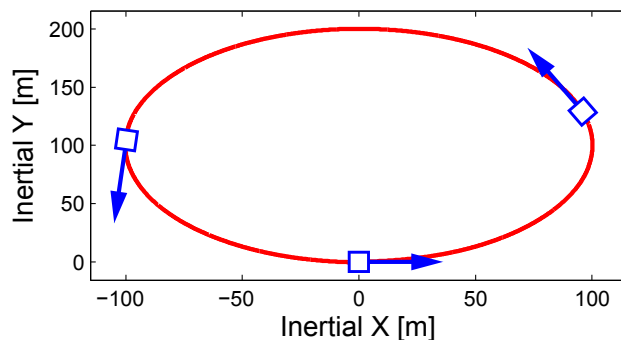| Parameter	Value	Parameter	Value
$m_{s,emp}$	1424.0 $[kg]$	l	2.578 $[m]$
m_t	142.0 $[kg]$	$l_{f,emp}$	1.016 $[m]$
I_x	606.1 $[kgm^2]$	l_w	1.539 $[m]$
$I_{z,emp}$	1523.0 $[kgm^2]$	h_s	0.224 $[m]$
ρ	1.206 $[kg/m^3]$	k_ϕ	42075.0 $[kgm^2/s^2]$
A_f	1.6 $[m^2]$	c_ϕ	5737.5 $[kgm^2/s]$
C_d	0.15		

Figure 4.1: Circular Path of Radius 100 m [28] ©2014 IEEE

Table 4.2: Activation of Vehicle Controller [28] ©2014 IEEE

If
• |Lateral Acceleration (a_y)| $> 0.25\ m/s^2$
• |Yaw Rate $(\dot{\psi})$| $> 1\ deg/s$
• $0.78\ deg\ < $ |Front Wheel Steering Angle (δ^f)|
$\Rightarrow$ Then, activate controller.
Else
$\Rightarrow$ deactivate controller.
End

Table 4.3: Controller Parameters [28] ©2014 IEEE

Parameter	Value	Parameter	Value
N_s	120	a_x^{lb}	-3 $[m/s^2]$
N	125	a_x^{ub}	0 $[m/s^2]$
τ_s	0.01 $[s]$	ϕ^b	3.5 $[^o]$
β_ϕ	510.66	β_{a_x}	0.0065
β_{v_x}	0.0094		

If the vehicle enters a curved road, the proposed controller is activated, that is, it is activated when the lateral dynamics prevail over the longitudinal dynamics. The criteria presented in Table 4.2 are used in order to activate the controller. Table 4.3 lists the parameters used for the constrained optimal control problem in (4.4).

4.5.2   Driving at 70 kph

Fig. 4.2 presents the 70 kph simulation results on the circular path of radius $R = 100$ m with the proposed controller. The dashed-dotted lines represent the simulation results when the proposed controller is turned off, whereas the solid lines represent the simulation results when the proposed controller is turned on. When the controller is turned off, the speed controller of CarSim tracks the constant $v_{x,des}$ of 70 kph as shown in Fig. 4.2a. In addition, the steering-wheel angle in Fig. 4.2b and the roll angle in Fig. 4.2c reach the steady-state values of about 47.91^o and 1.89^o, respectively.
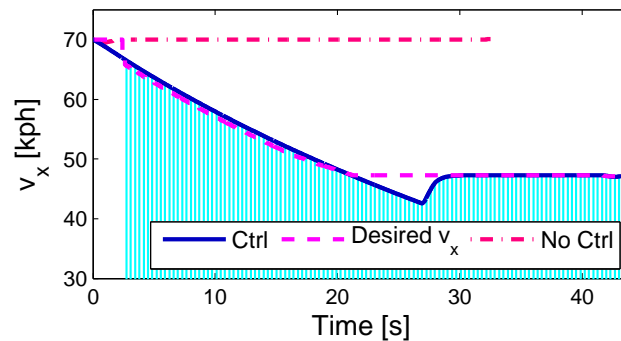
(a) Longitudinal Velocity v_x
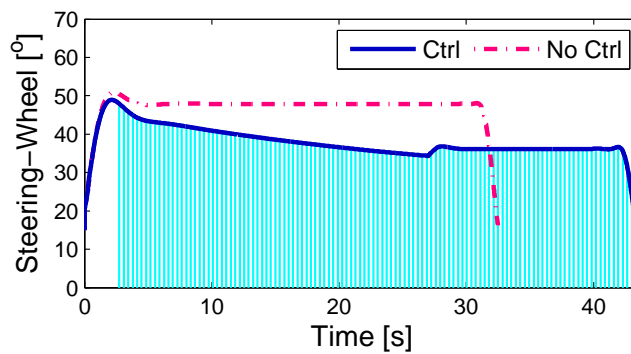
(b) Steering Wheel Angle
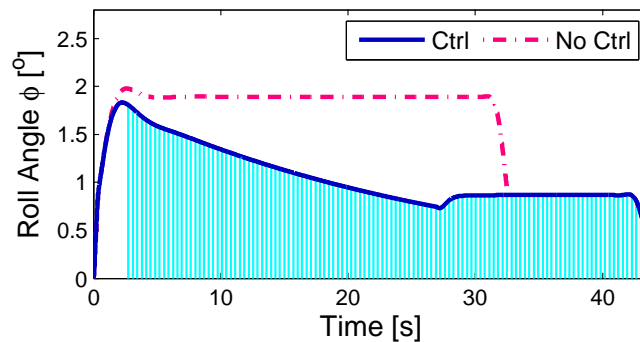
(c) Roll Angle ϕ

Figure 4.2: Comparison of Driving at 70 kph with/without the Controller [28] ©2014 IEEE

If the proposed controller is turned on, the desired velocity $v_{x,des}$, dashed line in Fig. 4.2a, is calculated by the proposed controller. Then, the vehicle slows down according to $v_{x,des}$, and converges to the optimal v_x of 46.56 kph at around 28 s, as shown in Fig. 4.2a. The region shaded by vertical lines corresponds to the time period when the controller is

activated after detecting the prevailing lateral dynamics. The roll angle is simultaneously
reduced and converges to the steady-state value 0.84^o, as shown in Fig. 4.2c. Note that a
33.5 % reduction of v_x attenuates the roll angle ϕ by about 55.6 %.

4.5.3 Driving at 105 kph

The simulations of driving at 105 kph demonstrate clearly the efficacy of the proposed control
algorithm. As shown in Fig. 4.3, the vehicle cannot follow the curved path, and strays from
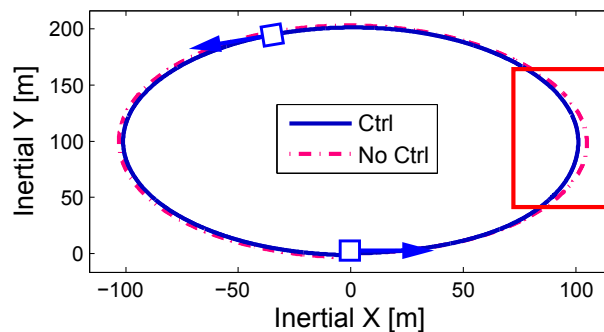
(a) Circular Path ($R = 100$ m)
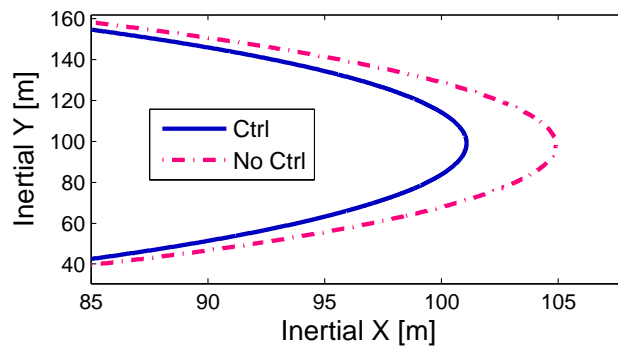
(b) Inside the Box

Figure 4.3: Trajectories When Driving at 105 kph with/without the Controller [28] ©2014
IEEE

the path when the vehicle enters the circle of the radius 100 m at 105 kph. The box in
Fig. 4.3a is magnified in Fig. 4.3b. In Fig. 4.3b, the dashed-dotted line represents the
trajectory without the proposed controller, whereas the solid line represents the trajectory
with the proposed controller. As shown in Fig. 4.3b, if the proposed controller is turned off,
the vehicle deviates in the radial direction by, at most, around 4.5 m from the trajectory
that is followed with the proposed controller. The deviation results not only from the high
speed, but also from the roll motion. The roll motion changes the grip condition between

the tires and a road. Assume an autonomous vehicle travels on a freeway and plans to follow
a circular path ($R = 100$ m) at 105 kph. Then, passengers in the autonomous vehicle can
be involved in crashes by deviating from a lane by 4.5 m.
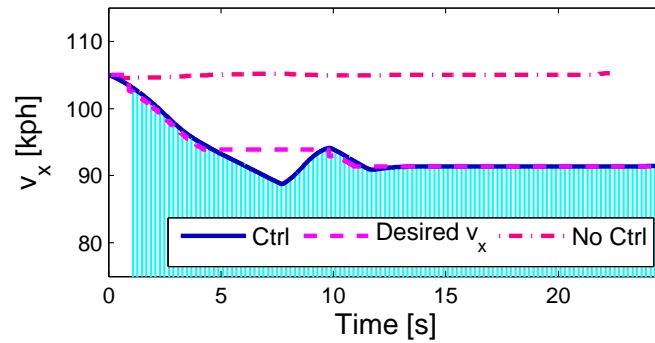
(a) Longitudinal Velocity v_x
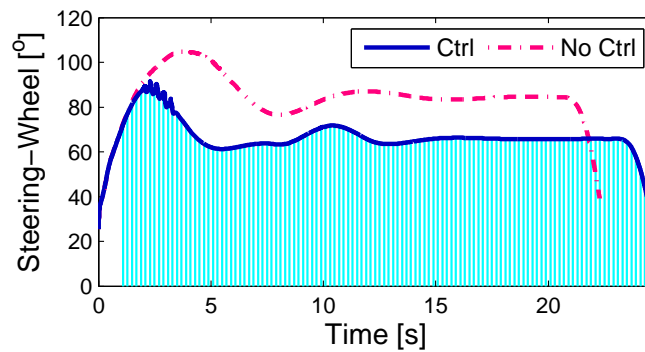
(b) Steering Wheel Angle
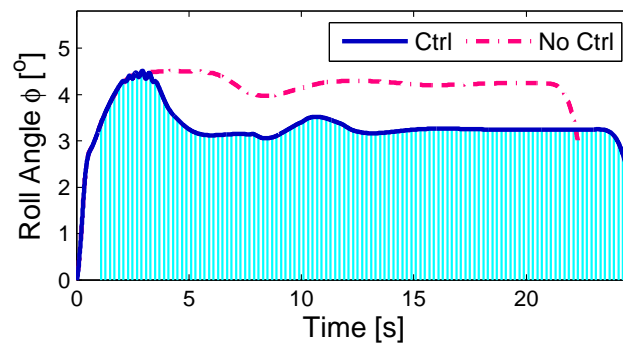
(c) Roll Angle ϕ

Figure 4.4: Comparison of Driving at 105 kph with/without the Controller [28] ©2014 IEEE

The simulation results of the velocity, the steering wheel angle, and the roll angle are

presented in Fig. 4.4. The dashed-dotted lines represent the results when the proposed
controller is not used, whereas the simulation results with the proposed controller are repre-
sented as the solid lines in Fig. 4.4. If the proposed controller is turned off, the steering-wheel
angle and the roll angle reach the steady-state values of about 84.46^o and 4.25^o, respectively,
as shown in Fig. 4.4b and Fig. 4.4c. The constant $v_{x,des}$ of 105 kph is tracked by the
speed controller of CarSim, as shown in Fig. 4.4a. If the proposed controller is turned
on, the vehicle velocity v_x decreases following the desired velocity $v_{x,des}$, the dashed line in
Fig. 4.4a, and converges to 91.39 kph at around 12.5 s, as shown in Fig. 4.4a. Note that
since driving at 105 kph is recognized to be a more dangerous maneuver than driving at 70
kph, the velocity v_x is reduced more rapidly in Fig. 4.4a than in Fig. 4.2a. While slowing
down the vehicle, the roll angle is simultaneously reduced in Fig. 4.4c, and converges to
the steady-state value 3.25^o. The results in Fig. 4.2 and Fig. 4.4 show that it is harder to
accomplish the control performance as the velocity v_x increases. Fig. 4.4c shows about 13.0
% attenuation of the roll angle ϕ by a reduction of about 23.5 % in v_x, which is a worse
result than that of driving at 70 kph. This also implies that suppressing the roll motion is
hard once the roll angle becomes large. Therefore, it is important to use the prediction of
the vehicle state for following a curved road and minimizing roll motion.

4.6 Simulation Results - with Parameter Identification

The vehicle inertial parameter identification in Chapter 3 is incorporated with the proposed controller. Note that the tire-road friction coefficient estimator in Chapter 2 is not incorporated into the controller since the acceleration data from tire cannot be obtained in the simulation software, CarSim.

4.6.1 Vehicle Maneuver in Simulations

A vehicle starts from the (0, 0) position, as shown in Fig. 4.5. The box in Fig. 4.5 magnifies the section of double lane change (DLC) which is the same as that in Fig. 3.5a in Chapter 3. The same vehicle velocity v_x in Fig. 3.5b is fed into the low-level speed controller for the DLC in Fig. 4.5, and the constant velocity of 105 kph is fed into the rest of the path in Fig. 4.5. After driving the DLC, the vehicle travels on sequential circular paths of a radius 100 m, and then it finishes driving by going straight.
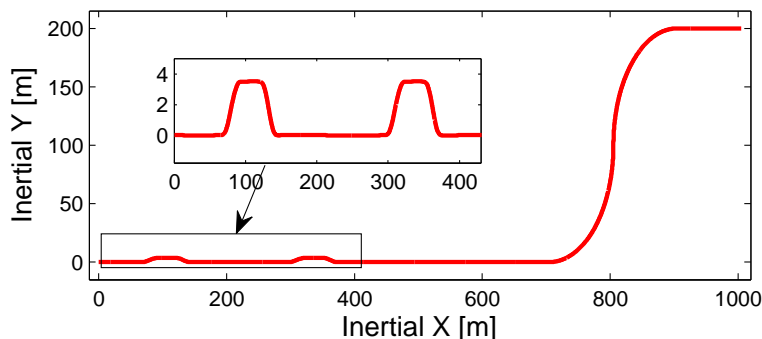
Figure 4.5: Double Lane Change (DLC) and Circular Path of Radius 100 m

The vehicle controller is activated when the vehicle enters the circular path by using the criteria presented in Table 4.2. Note that the inertial parameters are identified while driving the DLC.

4.6.2 Inertial Parameter Identification

The vehicle inertial parameters, including the additional sprung mass m_a and the longitudinal position of the CoG l_f, are identified with the algorithm developed in Chapter 3. The yaw moment of inertia I_z is calculated using the estimated m_a and l_f, as discussed in Chapter 3. The DLC maneuver in Fig. 4.5 is used for the identification of m_a and l_f.

Once the inertial parameters are identified during the DLC, the identification algorithm is turned off, and the controller uses the latest parameter values while computing control inputs

on the circular paths. On the circular paths, full braking control signals are fed into the vehicle, which results in the combined tire slip. This provokes a high level of nonlinearity in vehicle dynamics and tire forces, which degrades the inertial parameter identification. Then, the closed-loop behavior of the controller also degrades.
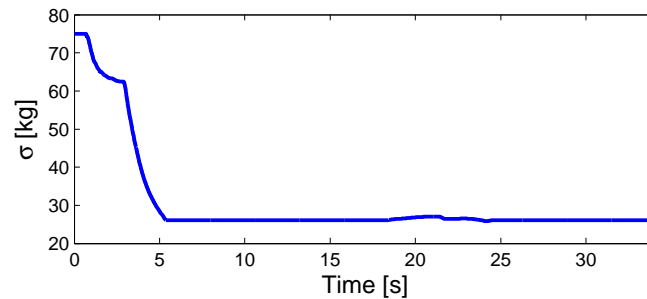
(a) Standard Deviation for m_a
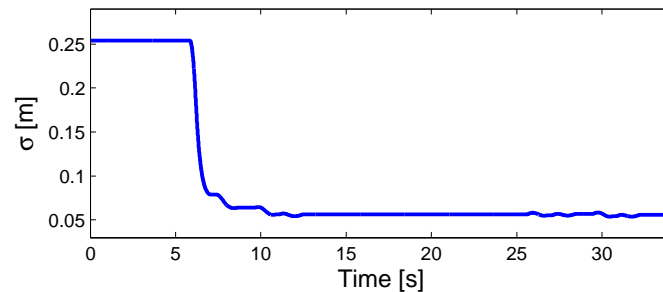
(b) Standard Deviation for l_f

Figure 4.6: Standard Deviation from Identification Algorithm

In order to judge when the identification algorithm is turned off, the covariance matrices computed with the unscented Kalman filter in Chapter 3 are used. For example, Fig. 4.6 presents the standard deviations for the estimates of m_a and l_f while running the identification algorithm. As m_a and l_f converge to true values, the standard deviation σ decreases and stays below some constant. Therefore, the identification algorithm is turned off if σ is lower than a threshold, as listed in Table 4.4.

4.6.3 Effect of Inertial Parameters

In this section, the effect of the inertial parameters on the control performance is investigated before running the controller combined with the inertial parameter estimator in the next section.

The control algorithm is applied to the maneuver in Fig. 4.5 assuming that the inertial parameters, m_a and l_f, are given. If the true values of m_a and l_f are known, the control

Table 4.4: Stop Identification Algorithm

If

- σ for $m_a \leq 27$
- σ for $l_f \leq 0.06$

Then

$\Rightarrow$ stop the identification algorithm.

End
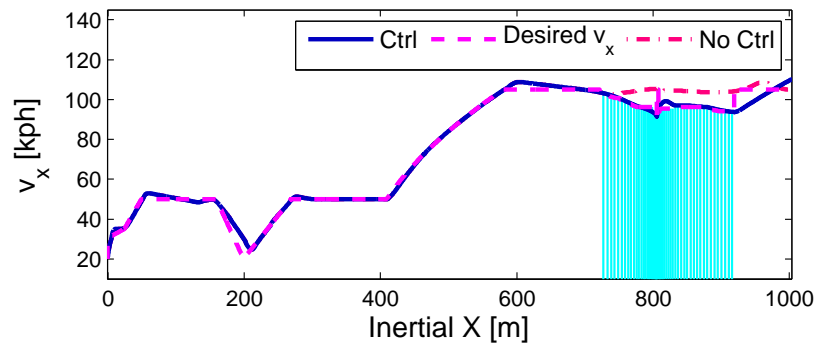
Figure 4.7: Longitudinal Velocity for Controller with Fixed Inertial Parameters

simulation results are presented as shown in Fig. 4.7 and Fig. 4.8. The proposed controller
is activated and reduces the velocity v_x within the shaded region in Fig. 4.7 by feeding
the desired velocity $v_{x,des}$. Without the proposed controller, the vehicle deviates from the
reference path by around 10 m as shown in Fig. 4.8c. The large steering angle is required
to compensate for the deviation as shown in Fig. 4.8a. Next, the effect of m_a and l_f on the
control performance is studied by changing m_a and l_f.
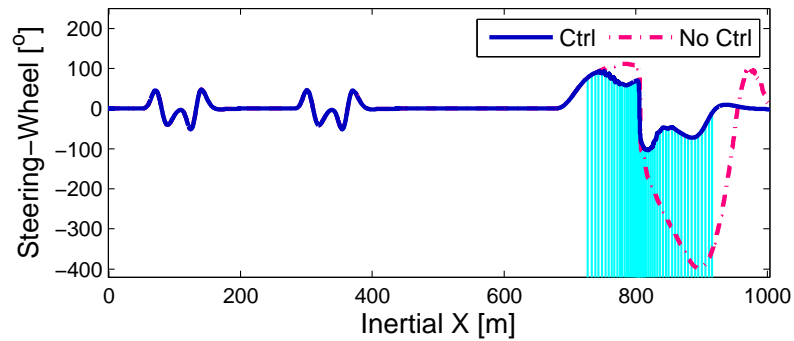
(a) Steering Wheel Angle
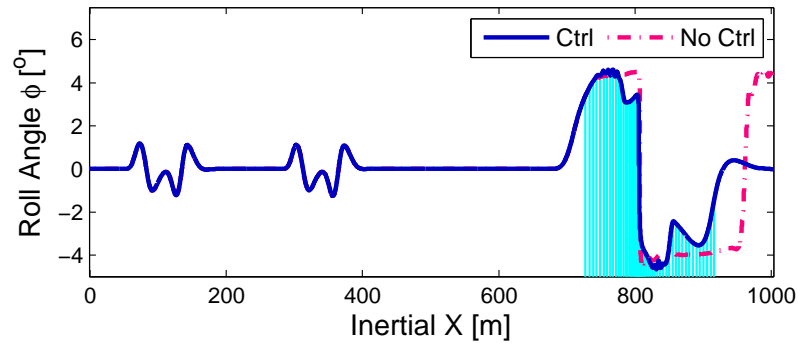
(b) Roll Angle
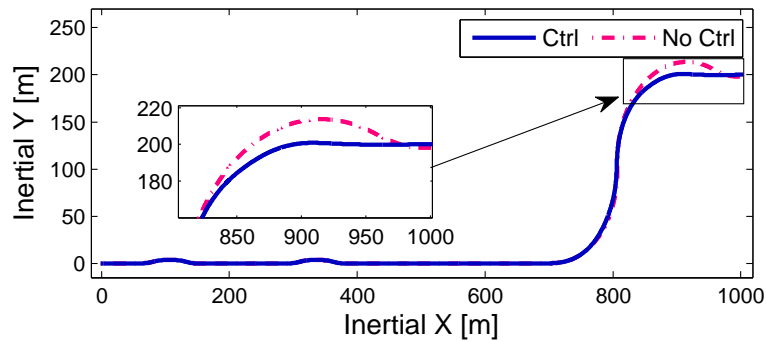
(c) Longitudinal Velocity

Figure 4.8: Controller Simulation

4.6.3.1   Additional Sprung Mass m_a

If m_a is changed by $\pm 50\%$, the controlled vehicle velocity is presented in Fig. 4.9. The
velocity v_x has little discrepancy between $m_a \times 1.0$ and $m_a \times 1.5$. However, the cost function

value in (4.4a) is underestimated with $m_a \times 0.5$, and therefore v_x is not reduced as much as in other m_a cases. This results in the loss of vehicle stability, as shown in Fig. 4.10.
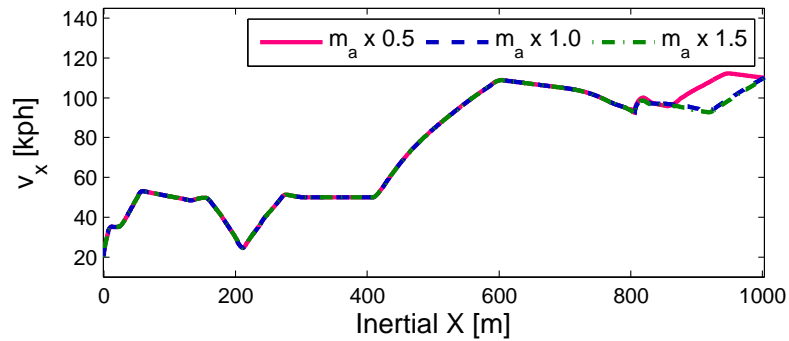
Figure 4.9: Longitudinal Velocity for $\pm 50\%$ of m_a

If $m_a \times 0.5$ is used for the control algorithm, the vehicle deviates from the reference path by about 3 m as shown in Fig. 4.10c even if the proposed controller is still running. In order to compensate for the deviation, the steering wheel is rapidly turned to both the left and the right, as shown in Fig. 4.10a. As a result, the roll angle in Fig. 4.10b also changes rapidly.

The above simulation results imply that the underestimate of m_a has more effect on the control performance than the overestimate of m_a does.
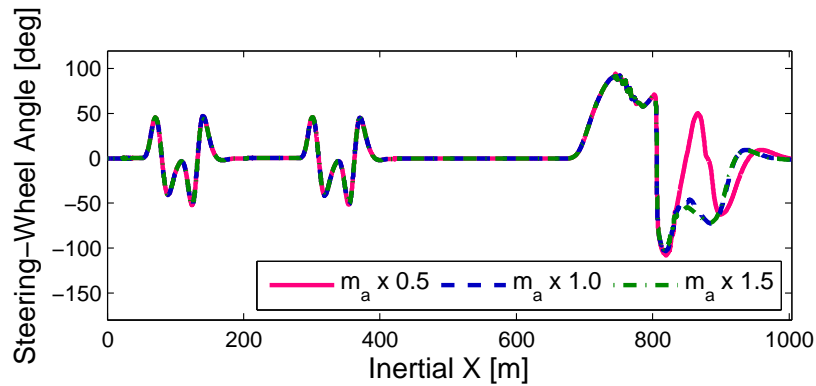
(a) Steering Wheel Angle
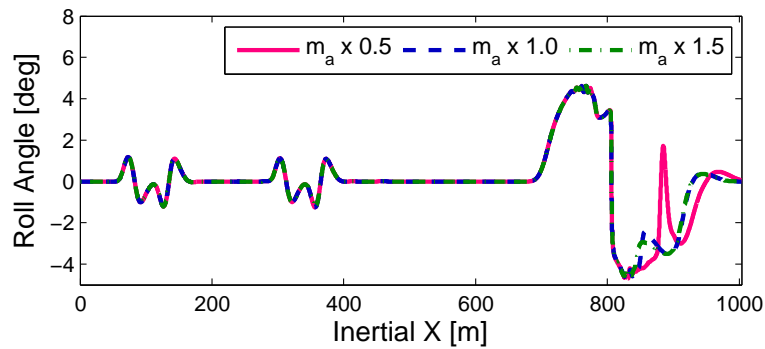
(b) Roll Angle
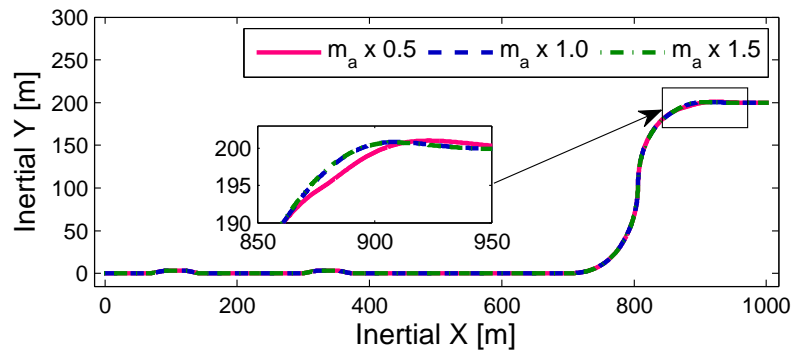
(c) Trajectory

Figure 4.10: Effect of $\pm 50\%$ of m_a

4.6.3.2   Longitudinal Position of the CoG l_f

If l_f is changed by $\pm 50\%$, the controlled vehicle velocity is presented in Fig. 4.11. The controlled velocity v_x is different for all three cases: $l_f \times 0.5$, $l_f \times 1.0$, and $l_f \times 1.5$. The cost

function value in (4.4a) is underestimated with $l_f \times 0.5$, and therefore v_x is not reduced as much as that of $l_f \times 1.0$ case. However, the cost function value in (4.4a) is overestimated with $l_f \times 1.5$, and therefore v_x is overly reduced compared to that of $l_f \times 1.0$ case.
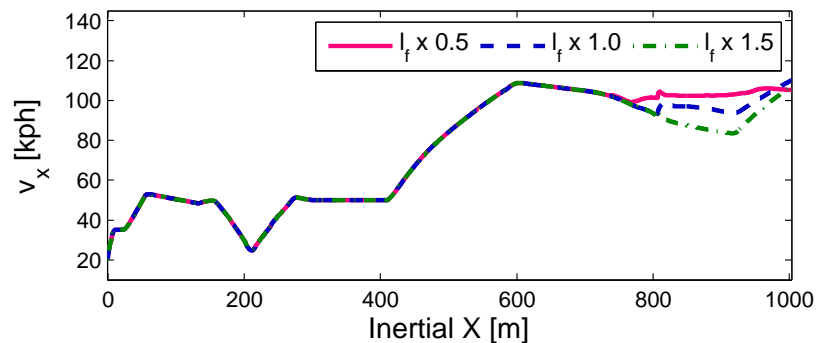
Figure 4.11: Longitudinal Velocity for $\pm 50\%$ of l_f

The effect of different l_f values on the control performance is clearly shown in Fig. 4.12. If $l_f \times 0.5$ is used for the controller, the vehicle strays from the reference path by around 6 m due to the less severe reduction of v_x, as shown in Fig. 4.12c, which leads to the large steering angle and the magnitude of roll angle greater than 4°, as shown in Fig. 4.12a and Fig. 4.12b, respectively. If $l_f \times 1.5$ is used for the control algorithm, the vehicle stays in a stable state, while the steering wheel angle and the roll angle are decreased more than those of $l_f \times 1.0$ case due to the overly reduced v_x.
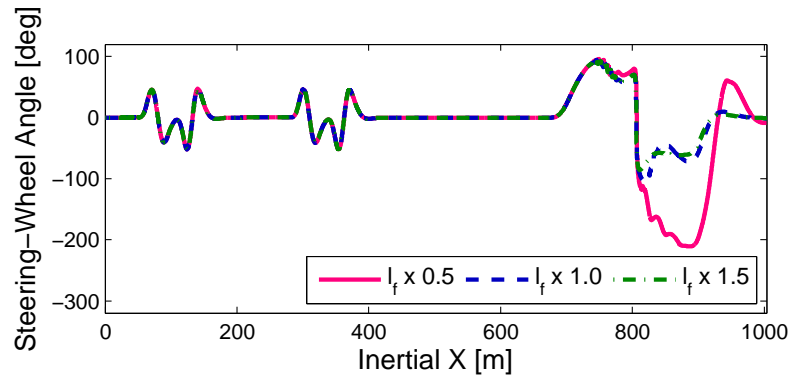
(a) Steering Wheel Angle
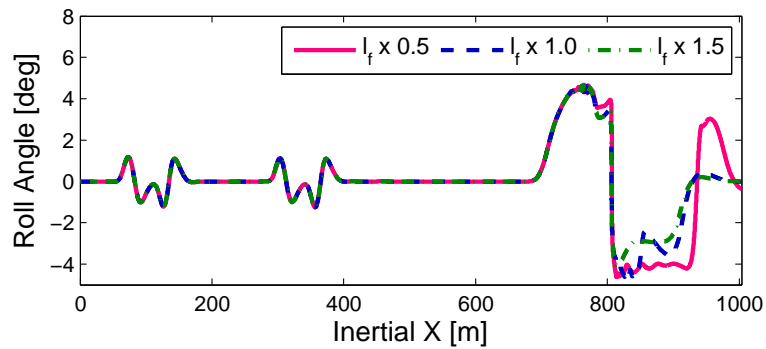
(b) Roll Angle
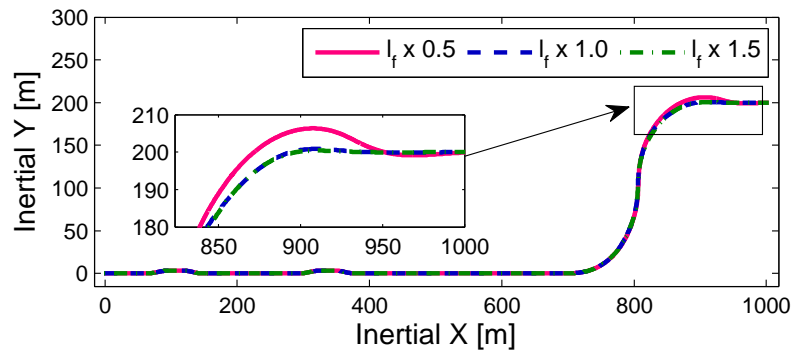
(c) Trajectory

Figure 4.12: Effect of $\pm 50\%$ of l_f

4.6.4 Controller with Inertial Parameter Identification

In this section, the proposed controller and the inertial parameter estimator run simultaneously on the path in Fig. 4.5. As the vehicle performs the DLC maneuver, the inertial

parameters are identified, and then the identification algorithm fixes the inertial parameter
estimates if the criteria in Table 4.4 are satisfied, as shown in Fig. 4.13. Although the ve-
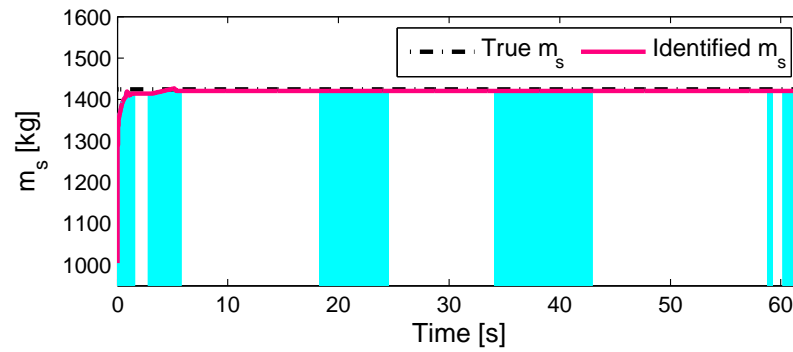
(a) Estimation of m_s
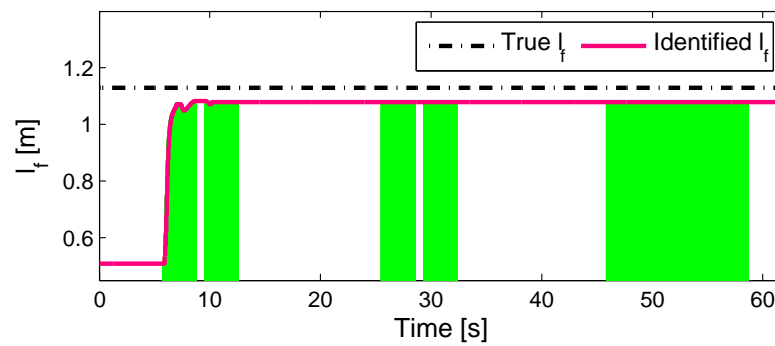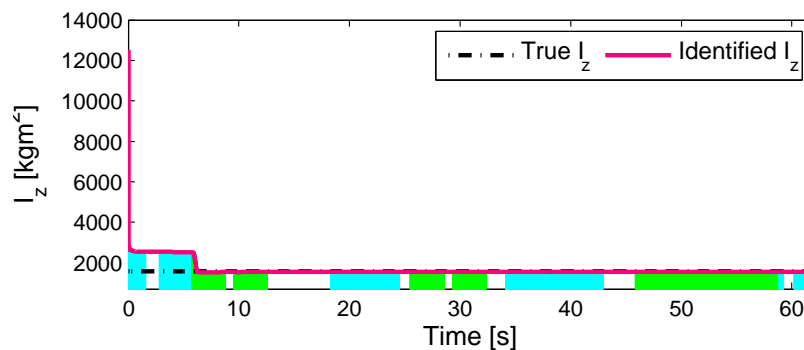
(b) Estimation of l_f

(c) Estimation of I_z

Figure 4.13: Inertial Parameter Identification (Initial Guess: $m_a \times 0.1$ and $l_f \times 0.5$)

hicle is in the midst of the maneuver for which m_a or l_f can be identified, the identification

algorithm does not update the inertial parameter values after about 14 s in Fig. 4.13. An initial guess of the inertial parameters in Fig. 4.13 is: $m_a \times 0.1$ and $l_f \times 0.5$.

The proposed controller creates the desired velocity $v_{x,des}$ with the identified parameters, m_a and l_f as shown in Fig. 4.14. The dashed-dotted line in Fig. 4.14 represents the case in which neither the identification algorithm nor the proposed controller are operated. The solid line in Fig. 4.14 represents the case in which both the identification algorithm and the proposed controller are operated.
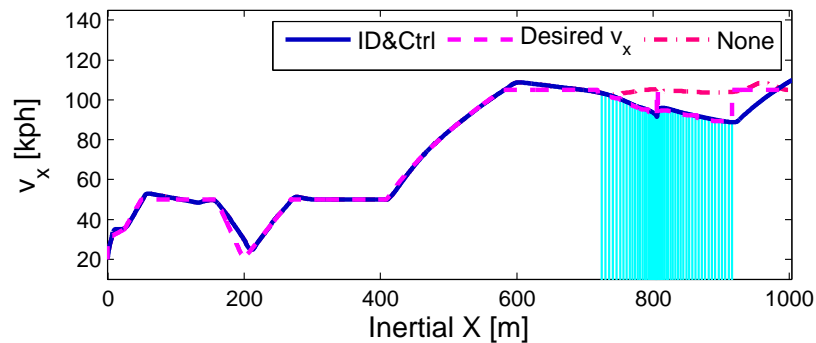
Figure 4.14: Combination of Identification and Controller (Velocity v_x)

The efficacy of the combined system is further demonstrated with Fig. 4.15. If neither the parameter estimator nor the controller operates, the vehicle strays from the reference path by about 13 m, as shown in Fig. 4.15c. The dashed line in Fig. 4.15 represents the case in which the controller operates with the inertial parameter guess: $m_a \times 0.1$ and $l_f \times 0.5$. In this case, the vehicle cannot follow the reference path. This implies that accurate inertial parameter values are of great importance to the control performance. If the controller operates along with the identification algorithm, the vehicle follows the reference path while maintaining the roll angle below about 3.5^o, as the dashed-dotted lines represent in Fig. 4.15. Note that the vehicle achieves the safe state by reducing just around 15 kph, as shown in Fig. 4.14 and Fig. 4.15.
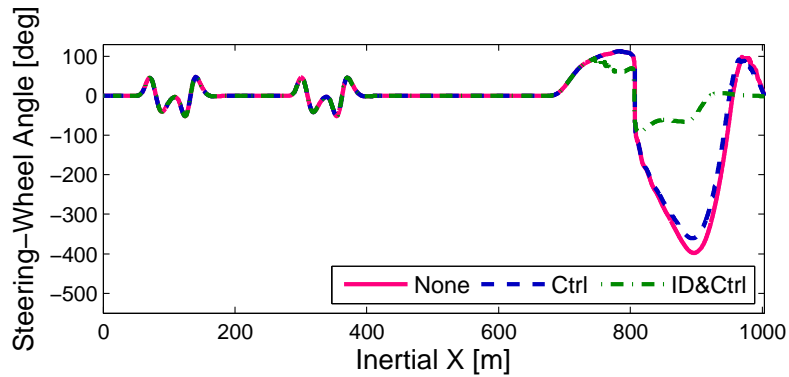
(a) Steering Wheel Angle
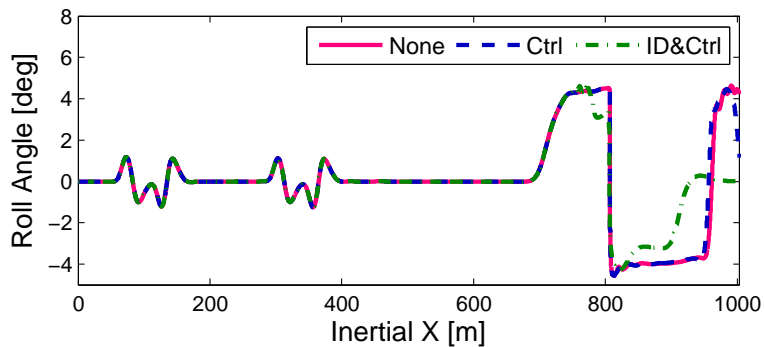
(b) Roll Angle
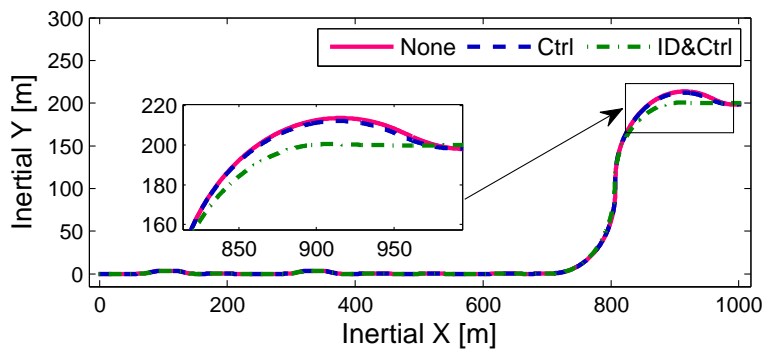
(c) Trajectory

Figure 4.15: Importance of Inertial Parameter Identification

4.7 Conclusion

This chapter designs a controller to follow a curved path while simultaneously preventing rollover. Excessive reduction of vehicle speed is circumvented to avoid dangerous rear-end

collisions on a freeway. The vehicle parameter estimator and state estimator in Chapter 2 are incorporated with the controller. Simulations illustrate the efficacy of the proposed control algorithm and the importance of the accurate parameter estimates.

Chapter 5

Conclusions and Future Work

This thesis developed new algorithms for identification of vehicle parameters: a tire-road friction coefficient and vehicle inertial parameters. In addition, a control scheme was designed for safe path following as well as roll mitigation. The proposed controller incorporates the inertial parameter identification algorithm, which shows the importance of accurate parameter estimates.

5.1   Conclusions

In Chapter 2, two tire-road friction coefficient estimation algorithms were developed based on an in-tire sensor which has not been used in most existing algorithms. The proposed algorithms utilize the lateral deflection and the change of lateral velocity, which are obtained from the tire lateral acceleration that is directly measured by a 3D wireless accelerometer attached on the inner center line of the tire.

The main challenge in using an in-tire accelerometer is that the orientation of the accelerometer body frame continues to change while the tire rotates. Inside the tire-road contact patch, the orientation-variation has negligible influence on the lateral acceleration, whereas the lateral acceleration measurements outside the contact patch is not trustworthy. Therefore, a method to determine the contact patch has been proposed and is used to extract the lateral acceleration only inside the contact patch. This approach ensures robustness to the orientation-variation of the accelerometer body frame.

Since only lateral acceleration inside the contact patch is used, its double integration profile cannot be described by the existing tire lateral deflection model. Therefore, a new form of mathematical models is derived with zero boundary conditions. They describe the lateral deflection and the change of lateral velocity profiles which are produced from the lateral acceleration only inside the contact patch. Furthermore, the models account for the random bias in the lateral acceleration profile, which further enhances robustness of the proposed algorithm.

The estimation algorithms were experimentally validated based on three different ma-

neuvers, each of which was executed on icy, snowy, and asphalt roads. Although the first
proposed algorithm does not take vehicle steering into account, it differentiates road surface
conditions in small steering maneuvers. In large steering maneuvers, the second proposed
algorithm yields better estimation results than the first algorithm since it involves the vehicle
steering in the estimation of the friction coefficient.

In Chapter 3, the vehicle inertial parameters, including the vehicle sprung mass, the center
of gravity (CoG) longitudinal position, and the yaw moment of inertia, were identified with
a novel approach.

The key idea is to utilize the correlation of the inertial parameters. Using the *Parallel-
Axis Theorem*, the yaw moment of inertia is expressed as a function of the additional sprung
mass and the CoG longitudinal position. Therefore, once the additional sprung mass and
the CoG longitudinal position are identified, the yaw moment of inertia is simply calculated
based on the correlation. This enables more accurate identification with less complexity
when compared to other existing algorithms.

The observability of the inertial parameters has not been analyzed in existing algorithms.
This thesis performs the local observability analysis based on a nonlinear vehicle model with
roll dynamics. According to the local observability analysis, the identification algorithm
switches between the different identification modes in order to separately identify the addi-
tional sprung mass and the longitudinal position of the CoG.

The dual unscented Kalman filter is applied to simultaneously estimate the inertial pa-
rameters and the vehicle states. In addition, the proposed algorithm uses the measurements
from commonly used vehicle sensors rather than costly equipment, such as a GPS and sus-
pension displacement sensors.

Extensive CarSim simulations and experimental tests illustrate that the proposed algo-
rithm yields acceptable estimates with small standard deviation values in the statistics and
has the capability to distinguish between two additional mass conditions.

In Chapter 4, a control algorithm to achieve yaw rate required to follow a curved path while
simultaneously mitigating roll motion was proposed.

The motivation is to enhance safety by traking the optimal balance in the trade-off
between vehicle speed and roll motion when an autonomous vehicle corners. In order to
reduce possibility of rollover, the receding horizon optimal control technique is utilized to
minimize roll motion throughout cornering. The roll motion is predicted with the four-wheel
vehicle model with roll dynamics and the tire brush model.

Since differential braking hinders a vehicle from following a curved path, full braking
is used as a control input. However, the proposed controller avoids excessive reduction of
vehicle speed since it can result in dangerous rear-end collisions on a freeway.

The proposed controller was simulated with a vehicle simulation software, CarSim. On a
circular path, the simulation results illustrate the efficacy of the proposed control algorithm.
In addition, the influence of the additional sprung mass and the CoG longitudinal position
on control performance is presented. The previously developed vehicle parameter estimator

and state estimator were incorporated with the controller in the simulation. The simulation results with the combined system demonstrate the importance of accurate parameter estimates in accomplishing high vehicle control performance.

5.2 Future Work

The proposed algorithm for a tire-road friction coefficient estimation could distinguish road surface conditions in experimental tests. However, the type of the test vehicle is a Sport Utility Vehicle (SUV) whose tires have thick sidewalls; the sidewall is the side part of pneumatic tires. Since the thick sidewall of a tire facilitates generating the tire lateral deflection, the proposed algorithm needs more tests with sedan cars which have thinner sidewalls than SUVs. Furthermore, influence of the in-tire accelerometer position on the estimation results should be studied since the in-tire accelerometer may not be positioned on the center line. The proposed algorithm could not be incorporated into the controller designed in this thesis since the vehicle simulation software does not provide tire acceleration data. For the compatibility with controllers using standard vehicle sensors, a different approach will be studied based on a dual unscented Kalman filter as used in this thesis.

Road grade and bank angles are not taken into consideration in the vehicle inertial parameter identification algorithm. These angles affect the additional sprung mass identification, and, in turn, degrade the identification results of the longitudinal position of the CoG. Therefore, more research should be conducted to obtain consistent identification results with varying road grade and bank angles. In addition, tires have severe nonlinearity in generating tire forces. Consequently, the order of magnitude of the identification results would be scaled up or down if the vehicle travels on different test tracks than that used in this thesis. A methodology to handle the tire model mismatch is important to advance the proposed identification algorithm further.

The proposed control algorithm unifies controllers for path following, roll mitigation, and avoidance of rear-end collisions. Even if the proposed controller assumes autonomous path following systems, the same approach can be applied to the commercialized adaptive cruise control (ACC) systems. If the proposed approach is combined with the ACC system, it can ensure additional safety compared to just maintaining a safe distance to preceding vehicles. Therefore, the proposed controller will be tested experimentally using a test vehicle with standard vehicle sensors, by which the efficacy of the proposed controller and the potential of application to current ACC systems can be demonstrated.

Bibliography

[1]   National Highway Trafic Safety Administration (NHTSA). *Trafic Safety Facts 2011: A Compilation of Motor Vehicle Crash Data from the Fatality Analysis Reporting System and the General Estimates System*. 2013.

[2]   S.J. Anderson et al. "A unified approach to semi-autonomous control of passenger vehicles in hazard avoidance scenarios". In: *IEEE International Conference on Systems, Man and Cybernetics, 2009. SMC 2009*. 2009, pp. 2032–2037. DOI: 10.1109/ICSMC.2009.5346330.

[3]   Sterling J. Anderson et al. "An optimal-control-based framework for trajectory planning, threat assessment, and semi-autonomous control of passenger vehicles in hazard avoidance scenarios". In: *International Journal of Vehicle Autonomous Systems* 8.2/3/4 (2010), p. 190. ISSN: 1471-0226, 1741-5306. DOI: 10.1504/IJVAS.2010.035796. URL: http://www.inderscience.com/info/inarticle.php?artid=35796 (visited on 01/27/2014).

[4]   M.S. Arulampalam et al. "A tutorial on particle filters for online nonlinear/non-Gaussian Bayesian tracking". In: *IEEE Transactions on Signal Processing* 50.2 (Feb. 2002), pp. 174 –188. ISSN: 1053-587X. DOI: 10.1109/78.978374.

[5]   Hong S. Bae, Jihan Ryu, and J. Christian Gerdes. "Road Grade and Vehicle Parameter Estimation for Longitudinal Control Using GPS". In: *IEEE Intelligent Transportation Systems Conference Proceedings*. Oakland (CA), USA, Aug. 2001.

[6]   Ferdinand Beer et al. *Vector Mechanics for Engineers: Dynamics*. en. McGraw-Hill Companies,Incorporated, Feb. 2009. ISBN: 9780078085093.

[7]   M. C. Best, A. P. Newton, and S. Tuplin. "The identifying extended Kalman filter: Parametric system identification of a vehicle handling model". en. In: *Proceedings of the Institution of Mechanical Engineers, Part K: Journal of Multi-body Dynamics* 221.1 (Mar. 2007), pp. 87–98. ISSN: 1464-4193, 2041-3068. DOI: 10.1243/14644193JMBD68. URL: http://pik.sagepub.com/content/221/1/87 (visited on 10/16/2013).

[8]   F. Braghin et al. "Measurement of contact forces and patch features by means of accelerometers fixed inside the tire to improve future car active control". In: *Vehicle System Dynamics* 44.sup1 (2006), pp. 3–13. ISSN: 0042-3114. DOI: 10.1080/

00423110600867101. URL: http://www.tandfonline.com/doi/abs/10.1080/
00423110600867101 (visited on 03/19/2013).

[9]   Christopher R. Carlson and J. Christian Gerdes. "Optimal Rollover Prevention With
       Steer by Wire and Differential Braking". In: *Proceedings of IMECE03*. Washington,
       D.C., Jan. 2003, pp. 345–354. DOI: 10.1115/IMECE2003-41825. URL: http://dx.
       doi.org/10.1115/IMECE2003-41825 (visited on 01/15/2014).

[10]   Federico Cheli et al. *Cyber Tyre: A Novel Sensor to Improve Vehicle's Safety*. SAE
       Technical Paper 2011-01-0990. Warrendale, PA: SAE International, Apr. 2011. URL:
       http://papers.sae.org/2011-01-0990/ (visited on 03/03/2014).

[11]   Federico Cheli et al. *Enhancement of ABS Performance through On-Board Estimation
       of the Tires' Response by Means of Smart Tires*. Tech. rep. 2011-01-0991. Warrendale,
       PA: SAE International, Apr. 2011. URL: http://papers.sae.org/2011-01-0991/
       (visited on 01/05/2013).

[12]   Bo-Chiuan Chen and Huei Peng. "Differential-Braking-Based Rollover Prevention for
       Sport Utility Vehicles with Human-in-the-loop Evaluations". In: *Vehicle System Dy-
       namics* 36.4-5 (2001), pp. 359–389. ISSN: 0042-3114. DOI: 10.1076/vesd.36.4.359.
       3546. URL: http://www.tandfonline.com/doi/abs/10.1076/vesd.36.4.359.3546
       (visited on 01/16/2014).

[13]   J. Christian Gerdes, Eric J. Rossetter, and Ursina Saur. "Combining Lanekeeping and
       Vehicle Following with Hazard Maps". In: *Vehicle System Dynamics* 36.4-5 (2001),
       pp. 391–411. ISSN: 0042-3114. DOI: 10.1076/vesd.36.4.391.3548. URL: http:
       //www.tandfonline.com/doi/abs/10.1076/vesd.36.4.391.3548 (visited on
       01/16/2014).

[14]   S. De Bruyne et al. "Online Estimation of Vehicle Inertial Parameters for Improving
       Chassis Control Systems". In: *IFAC World Congress, 2011*. Aug. 2011, pp. 1814–1819.

[15]   Hugh F. Durrant-Whyte. *Introdunction to Estimation and the Kalman Filter*. URL:
       www.isip40.it/resources/Dispense/DataFusionSIIT/Estimation_KF.pdf.

[16]   G. Erdogan, L. Alexander, and R. Rajamani. "Estimation of Tire-Road Friction Co-
       efficient Using a Novel Wireless Piezoelectric Tire Sensor". In: *IEEE Sensors Journal*
       11.2 (Feb. 2011), pp. 267–279. ISSN: 1530-437X. DOI: 10.1109/JSEN.2010.2053198.

[17]   Gurkan Erdogan et al. "Development of a New Lateral Stability Control System En-
       hanced With Accelerometer Based Tire Sensors". In: (Jan. 2010), pp. 841–848. DOI:
       10.1115/DSCC2010-4181. URL: http://dx.doi.org/10.1115/DSCC2010-4181
       (visited on 03/19/2013).

[18]   Gurkan Erdogan et al. "Tire Sensors for the Measurement of Slip Angle and Friction
       Coefficient and Their Use in Stability Control Systems". en. In: *SAE International
       Journal of Passenger Cars - Mechanical Systems* 4.1 (June 2011), pp. 44–58. ISSN:
       1946-3995, 1946-4002. DOI: 10.4271/2011-01-0095. URL: http://saepcmech.
       saejournals.org/content/4/1/44 (visited on 11/29/2012).

[19] P. Falcone et al. "Predictive Active Steering Control for Autonomous Vehicle Systems".
      In: *IEEE Transactions on Control Systems Technology* 15.3 (2007), pp. 566–580. ISSN:
      1063-6536. DOI: 10.1109/TCST.2007.894653.

[20] H.K. Fathy, Dongsoo Kang, and J.L. Stein. "Online vehicle mass estimation using
      recursive least squares and supervisory data extraction". In: *American Control Con-
      ference, 2008*. June 2008, pp. 1842 –1848. DOI: 10.1109/ACC.2008.4586760.

[21] N.J. Gordon, D.J. Salmond, and A.F.M. Smith. "Novel approach to nonlinear/non-
      Gaussian Bayesian state estimation". In: *Radar and Signal Processing, IEE Proceedings
      F* 140.2 (Apr. 1993), pp. 107 –113. ISSN: 0956-375X.

[22] A. Gray et al. "A Unified Approach to Threat Assessment and Control for Automo-
      tive Active Safety". In: *IEEE Transactions on Intelligent Transportation Systems* 14.3
      (2013), pp. 1490–1499. ISSN: 1524-9050. DOI: 10.1109/TITS.2013.2262097.

[23] Fredrik Gustafsson. "Slip-based tire-road friction estimation". In: *Automatica* 33.6
      (June 1997), pp. 1087–1099. ISSN: 0005-1098. DOI: 10.1016/S0005-1098(97)00003-4.
      URL: http://www.sciencedirect.com/science/article/pii/S0005109897000034
      (visited on 03/19/2013).

[24] Jin-Oh Hahn, R. Rajamani, and L. Alexander. "GPS-based real-time identification of
      tire-road friction coefficient". In: *IEEE Transactions on Control Systems Technology*
      10.3 (May 2002), pp. 331–343. ISSN: 1063-6536. DOI: 10.1109/87.998016.

[25] Monson H. Hayes. *Statistical digital signal processing and modeling.* en. John Wiley &
      Sons, Apr. 1996. ISBN: 9780471594314.

[26] Simon Haykin. *Kalman Filtering and Neural Networks.* en. John Wiley & Sons, Apr.
      2004. ISBN: 9780471464211.

[27] R. Hermann and Arthur J. Krener. "Nonlinear controllability and observability". In:
      IEEE Transactions on Automatic Control 22.5 (1977), pp. 728–740. ISSN: 0018-9286.
      DOI: 10.1109/TAC.1977.1101601.

[28] Sanghyun Hong and J. Karl Hedrick. "Roll Prediction-based Optimal Control for Safe
      Path Following". In: *2014 IEEE Conference on Control and Decision*. Dec. 2014, sub-
      mitted.

[29] Sanghyun Hong and J. Karl Hedrick. "Tire-Road Friction Coefficient Estimation with
      Vehicle Steering". In: *2013 IEEE Intelligent Vehicle Symposium*. GoldCoast, Australia,
      June 2013.

[30] Sanghyun Hong et al. "A Novel Approach for Vehicle Inertial Parameter Identification
      using a Dual Kalman Filter". In: *IEEE Transactions on Intelligent Transportation
      Systems (submitted)* (Jan. 2014).

[31]   Sanghyun Hong et al. "Tyre-road friction coefficient estimation based on tyre sensors and lateral tyre deflection: modelling, simulations and experiments". In: *Vehicle System Dynamics* 51.5 (2013), pp. 627–647. ISSN: 0042-3114. DOI: 10.1080/00423114.2012.758859. URL: http://www.tandfonline.com/doi/abs/10.1080/00423114.2012.758859 (visited on 03/04/2013).

[32]   Sanghyun Hong et al. "Vehicle Inertial Parameter Identification using Extended and Unscented Kalman Filters". In: *2013 IEEE Conference on Intelligent Transport Systems*. The Hague, The Netherlands, Oct. 2013.

[33]   Reza N. Jazar. *Vehicle Dynamics: Theory and Application*. en. Springer, Mar. 2008. ISBN: 9780387742434.

[34]   S. J. Julier, J. K. Uhlmann, and H. Durrant-Whyte. "A new approach for filtering nonlinear systems". In: *American Control Conference, 1995*. June 1995, pp. 1628–1632.

[35]   K. Li, J. A. Misener, and K. Hedrick. "On-board road condition monitoring system using slip-based tyre-road friction estimation and wheel speed signal analysis". en. In: *Proceedings of the Institution of Mechanical Engineers, Part K: Journal of Multi-body Dynamics* 221.1 (Mar. 2007), pp. 129–146. ISSN: 1464-4193, 2041-3068. DOI: 10.1243/1464419JMBD60. URL: http://pik.sagepub.com/content/221/1/129 (visited on 03/19/2013).

[36]   Jing-Fu Liu, Jui-Hung Wu, and Yi-Feng Su. "Development of an Interactive Lane Keeping Control System for Vehicle". In: *IEEE Vehicle Power and Propulsion Conference, 2007. VPPC 2007*. 2007, pp. 702–706. DOI: 10.1109/VPPC.2007.4544214.

[37]   K. Macek, R. Philippsen, and R. Siegwart. "Path following for autonomous vehicle navigation with inherent safety and dynamics margin". In: *2008 IEEE Intelligent Vehicles Symposium*. 2008, pp. 108–113. DOI: 10.1109/IVS.2008.4621276.

[38]   Steffen Muller, Michael Uchanski, and Karl Hedrick. "Estimation of the Maximum Tire-Road Friction Coefficient". In: *Journal of Dynamic Systems, Measurement, and Control* 125.4 (Jan. 2004), pp. 607–617. ISSN: 0022-0434. DOI: 10.1115/1.1636773. URL: http://dx.doi.org/10.1115/1.1636773 (visited on 03/19/2013).

[39]   H. Nijmeijer. "Observability of autonomous discrete time non-linear systems: a geometric approach". In: *International Journal of Control* 36.5 (1982), pp. 867–874. ISSN: 0020-7179. DOI: 10.1080/00207178208932936. URL: http://www.tandfonline.com/doi/abs/10.1080/00207178208932936 (visited on 02/09/2013).

[40]   H. B. Pacejka. *Tyre and Vehicle Dynamics*. en. Butterworth-Heinemann, 2006. ISBN: 9780750669184.

[41]   R. Rajamani and J.K. Hedrick. "Adaptive observers for active automotive suspensions: theory and experiment". In: *IEEE Transactions on Control Systems Technology* 3.1 (1995), pp. 86–93. ISSN: 1063-6536. DOI: 10.1109/87.370713.

[42] Rajesh Rajamani. *Vehicle Dynamics And Control*. en. Springer Verlag, 2006. ISBN: 9780387263960.

[43] Laura R. Ray. "Nonlinear Tire Force Estimation and Road Friction Identification: Simulation and Experiments," in: *Automatica* 33.10 (Oct. 1997), pp. 1819–1833. ISSN: 0005-1098. DOI: `10.1016/S0005-1098(97)00093-9`. URL: `http://www.sciencedirect.com/science/article/pii/S0005109897000939` (visited on 03/19/2013).

[44] Ayyoub Rezaeian et al. *Cascaded Dual Extended Kalman Filter for Combined Vehicle State Estimation and Parameter Identification*. SAE Technical Paper 2013-01-0691. Warrendale, PA: SAE International, Apr. 2013. URL: `http://papers.sae.org/2013-01-0691/` (visited on 03/10/2014).

[45] Ayyoub Rezaeian et al. "Joint Unscented Kalman Filter for Combined Estimation of Vehicle States and Parameters". In: Seoul, South Korea, Sept. 2012.

[46] S.M. Savaresi et al. "New Regressors for the Direct Identification of Tire Deformation in Road Vehicles Via #x201C;In-Tire #x201D; Accelerometers". In: *IEEE Transactions on Control Systems Technology* 16.4 (July 2008), pp. 769–780. ISSN: 1063-6536. DOI: `10.1109/TCST.2007.912245`.

[47] Kanwar Bharat Singh, Mustafa Ali Arat, and Saied Taheri. "Enhancement of Collision Mitigation Braking System Performance Through Real-Time Estimation of Tire-road Friction Coefficient by Means of Smart Tires". en. In: *SAE International Journal of Passenger Cars - Electronic and Electrical Systems* 5.2 (Sept. 2012), pp. 607–624. ISSN: 1946-4614, 1946-4622. DOI: `10.4271/2012-01-2014`. URL: `http://saepcelec.saejournals.org/content/5/2/607` (visited on 01/05/2013).

[48] S. Solmaz, M. Corless, and R. Shorten. "A methodology for the design of robust rollover prevention controllers for automotive vehicles: Part 1-Differential braking". In: *2006 45th IEEE Conference on Decision and Control*. 2006, pp. 1739–1744. DOI: `10.1109/CDC.2006.377179`.

[49] S. Solmaz, M. Corless, and R. Shorten. "A methodology for the design of robust rollover prevention controllers for automotive vehicles: Part 2-Active steering". In: *American Control Conference, 2007. ACC '07*. 2007, pp. 1606–1611. DOI: `10.1109/ACC.2007.4282618`.

[50] Selim Solmaz, Mehmet Akar, and Robert Shorten. "Adaptive Rollover Prevention for Automotive Vehicles with Differential Braking". In: *Proceedings of the 17th IFAC World Congress*. July 2008, pp. 4695–4700. DOI: `10.3182/20080706-5-KR-1001.00790`. URL: `http://www.ifac-papersonline.net/Detailed/36503.html` (visited on 01/15/2014).

[51] A. Vahidi, A. Stefanopoulou, and H. Peng. "Recursive least squares with forgetting for online estimation of vehicle mass and road grade: theory and experiments". In: *Vehicle System Dynamics* 43.1 (2005), pp. 31–55. ISSN: 0042-3114. DOI: 10.1080/00423110412331290446. URL: http://www.tandfonline.com/doi/abs/10.1080/00423110412331290446 (visited on 03/11/2013).

[52] E. A. Wan, R. van der Merwe, and A. T. Nelson. "Dual estimation and the unscented transformation". In: *Advances in Neural Information Processing Systems*. July 2000, pp. 666–672.

[53] T. A. Wenzel et al. "Dual extended Kalman filter for vehicle state and parameter estimation". In: *Vehicle System Dynamics* 44.2 (2006), pp. 153–171. ISSN: 0042-3114. DOI: 10.1080/00423110500385949. URL: http://www.tandfonline.com/doi/abs/10.1080/00423110500385949 (visited on 01/21/2013).

[54] V. Winstead and I.V. Kolmanovsky. "Estimation of road grade and vehicle mass via model predictive control". In: *Proceedings of 2005 IEEE Conference on Control Applications, 2005. CCA 2005.* 2005, pp. 1588–1593. DOI: 10.1109/CCA.2005.1507359.

[55] Kyongsu Yi, Karl Hedrick, and Seong-Chul Lee. "Estimation of Tire-Road Friction Using Observer Based Identifiers". In: *Vehicle System Dynamics* 31.4 (1999), pp. 233–261. ISSN: 0042-3114. DOI: 10.1076/vesd.31.4.233.4231. URL: http://www.tandfonline.com/doi/abs/10.1076/vesd.31.4.233.4231 (visited on 01/05/2013).

[56] Seongjin Yim. "Design of a robust controller for rollover prevention with active suspension and differential braking". en. In: *Journal of Mechanical Science and Technology* 26.1 (Jan. 2012), pp. 213–222. ISSN: 1738-494X, 1976-3824. DOI: 10.1007/s12206-011-0915-9. URL: http://link.springer.com/article/10.1007/s12206-011-0915-9 (visited on 02/18/2014).

[57] Jangyeol Yoon et al. "Unified Chassis Control for Rollover Prevention and Lateral Stability". In: *IEEE Transactions on Vehicular Technology* 58.2 (Feb. 2009), pp. 596–609. ISSN: 0018-9545. DOI: 10.1109/TVT.2008.927724.

[58] R. Zarringhalam et al. "A comparative study on identification of vehicle inertial parameters". In: *American Control Conference (ACC), 2012*. June 2012, pp. 3599–3604.

[59] Yuhong Zheng and Danny Milot. "Real-time signal processing for vehicle tire load monitoring". Pat. US6980925 B2. U.S. Classification 702/175, 702/142, 702/174, 702/43, 702/173, 702/148, 340/679, 702/141, 702/140, 702/145, 702/138, 702/98, 702/42, 702/139, 702/41; International Classification B60C23/06; Cooperative Classification B60C23/064, B60C23/0488; European Classification B60C23/04D1, B60C23/06C. Dec. 2005.

Appendix   A

Recursive Algorithm of the UKF

The main advantages of the Unscented Kalman Filter (UKF), e.g. the second-order accuracy and the simple implementation, result from the use of the Unscented Transformation (UT). The UT captures the statistics of a random vector undergoing a nonlinear transformation

Table A.1: Scaling Factors & Weights [30] ©2014 IEEE

$$\lambda := \alpha^2(L + \kappa) - L$$
$$W_0^{(m)} = \frac{\lambda}{L+\lambda}$$
$$W_0^{(c)} = \frac{\lambda}{L+\lambda} + 1 - \alpha^2 + \beta$$
$$W_i^{(m)} = W_i^{(c)} = \frac{1}{2(L+\lambda)}, \quad i = 1, ..., 2L$$

[26]. Let x be an L-dimensional random vector with the mean $\hat{x}$ and the covariance P_x, which is propagated through the nonlinear function $y = f(x)$. By using $\hat{x}$ and P_x, $2L + 1$ discrete sample points $\mathcal{X}_i$, called *sigma points*, are determined: $\{\mathcal{X}_i\}_{i=0}^{2L} = \{\hat{x}, \ \hat{x} \pm \sigma_j, j = 1, \ldots, L\}$, where σ_i is the ith column of the matrix $\sqrt{(L + \lambda)P_x}$. The scaling factor λ is obtained in Table A.1, where the scaling factor α relates to the spread of sigma points about the mean $\hat{x}$, and κ is generally set to $3-L$. The sigma points $\{\mathcal{X}_i\}_{i=0}^{2L}$ are propagated through the nonlinear transformation $y = f(x)$ to produce $\mathcal{Y}_i$: $\{\mathcal{Y}_i\}_{i=2}^{2L} = \{f(\mathcal{X}_i)\}_{i=2}^{2L}$. The UT approximates the mean $\hat{y}$ and the covariance P_y with the weighted summation of $\{\mathcal{Y}_i\}_{i=0}^{2L}$: $\hat{y} \simeq \sum_{i=0}^{2L} W_i^{(m)} \mathcal{Y}_i$ and $P_y \simeq \sum_{i=0}^{2L} W_i^{(c)}(\mathcal{Y}_i - \hat{y})(\mathcal{Y}_i - \hat{y})^\top$. The weights, $W_i^{(m)}$ and $W_i^{(c)}$, are computed in Table A.1, where β is determined to incorporate prior knowledge of the x distribution, and $\beta = 2$ is optimal for Gaussian distributions [26] (this paper uses $\alpha = 0.01$, $\kappa = 1$, $\beta = 2$).

The UKF has the two estimation stages: prediction before the measurement and update after the measurement. All equations in the two stages are extracted from [26], and adapted for the state-space model in (3.15)-(3.17) as presented in Table A.2 and A.3 for the vehicle inertial parameter and the vehicle state identification, respectively. Consider random vectors i and j, e.g. w and s in Table A.2 and A.3. The expectation value of a vector i is denoted as $\hat{i}$.

Table A.2: Vehicle Inertial Parameter Identification [30] ©2014 IEEE

1: Initialize $\hat{w}_0^+$, $P_{w_0}^+$:
$\quad \hat{w}_0^+ = E[w(0)]$
$\quad P_{w_0}^+ = E[(w(0) - \hat{w}_0^+)(w(0) - \hat{w}_0^+)^\top]$
$\quad \gamma := \sqrt{L + \lambda}$
2: Prediction before the measurement of $d(k)$:
$\quad \hat{w}_k^- = \hat{w}_{k-1}^+$
$\quad P_{w_k}^- = P_{w_{k-1}}^+ + R_{k-1}^r$
$\quad \mathcal{W}_{k|k-1} = [\hat{w}_k^- \quad \hat{w}_k^- + \gamma\sqrt{P_{w_k}^-} \quad \hat{w}_k^- - \gamma\sqrt{P_{w_k}^-}]$
$\quad \mathcal{S}_{k|k-1} = T(\mathcal{W}_{k|k-1}, \hat{s}_{k-1}^+, u(k-1))$
$\quad \dot{\mathcal{S}}_{k|k-1} = F(\mathcal{W}_{k|k-1}, \hat{s}_{k-1}^+, u(k-1))$
$\quad \mathcal{D}_{k|k-1} = G(\mathcal{S}_{k|k-1}, \dot{\mathcal{S}}_{k|k-1})$
$\quad \hat{d}_k^- = \sum_{i=0}^{2L} W_i^{(m)} \mathcal{D}_{i,k|k-1}$
3: Update after the measurement of $d(k)$:
$\quad P_{d_k}^- = \sum_{i=0}^{2L} W_i^{(c)}(\mathcal{D}_{i,k|k-1} - \hat{d}_k^-)(\mathcal{D}_{i,k|k-1} - \hat{d}_k^-)^\top + R_k^e$
$\quad P_{w_k d_k}^- = \sum_{i=0}^{2L} W_i^{(c)}(\mathcal{W}_{i,k|k-1} - \hat{w}_k^-)(\mathcal{D}_{i,k|k-1} - \hat{d}_k^-)^\top$
$\quad \mathcal{K}_k = P_{w_k d_k}^- (P_{d_k}^-)^{-1}$
$\quad \hat{w}_k^+ = \hat{w}_k^- + \mathcal{K}_k[d(k) - \hat{d}_k^-]$
$\quad P_{w_k}^+ = P_{w_k}^- - \mathcal{K}_k P_{d_k}^- \mathcal{K}_k^\top$

The superscript $(-)$ indicates *a-priori*, and $(+)$ indicates *a-posteriori*. The cross covariance matrix of random vectors i and j is denoted as P_{ij}. The covariance matrix of noise i at time k is denoted as R_k^i. The dimension of w and s is denoted as L in Table A.2 and A.3. The scaling factor λ and the weights, $W_i^{(m)}$ and $W_i^{(c)}$, are obtained in Table A.1.

In Table A.2, the state-space model in (3.16) and (3.17) is used for the vehicle inertial parameter, w, identification. The UT is applied in calculating $\hat{d}_k^-$, $P_{d_k}^-$, and $P_{w_k d_k}^-$. The UKF for the vehicle state vector s in Table A.3 uses the system in (3.15) and (3.17). The UT is applied in calculating $\hat{s}_k^-$, $P_{s_k}^-$, $\hat{d}_k^-$, $P_{d_k}^-$, and $P_{s_k d_k}^-$. The difference of Table A.3 from Table A.2 is that the UT is used to estimate the a-priori state vector at time k, $\hat{s}_k^-$, since the state $s(k+1)$ is calculated through the state transition function in (3.15), whereas the state transition matrix for $w(k+1)$ in (3.16) is the identity matrix: $w(k+1) = w(k)$.

Table A.3: Vehicle State Estimation [30] ©2014 IEEE

1: Initialize $\hat{s}_0^+$, $P_{s_0}^+$:
  $\hat{s}_0^+ = E[s(0)]$
  $P_{s_0}^+ = E[(s(0) - \hat{s}_0^+)(s(0) - \hat{s}_0^+)^\top]$
  $\gamma := \sqrt{L + \lambda}$

2: Prediction before the measurement of $d(k)$:
  $\mathcal{S}_{k-1} = [\hat{s}_{k-1}^+ \quad \hat{s}_{k-1}^+ + \gamma\sqrt{P_{s_{k-1}}^+} \quad \hat{s}_{k-1}^+ - \gamma\sqrt{P_{s_{k-1}}^+}]$
  $\mathcal{S}_{k|k-1}^* = T(\hat{w}_{k-1}^+, \ \mathcal{S}_{k-1}, \ u_{k-1})$
  $\hat{s}_k^- = \sum_{i=0}^{2L} W_i^{(m)} \mathcal{S}_{i,k|k-1}^*$
  $P_{s_k}^- = \sum_{i=0}^{2L} W_i^{(c)} (\mathcal{S}_{i,k|k-1}^* - \hat{s}_k^-)(\mathcal{S}_{i,k|k-1}^* - \hat{s}_k^-)^\top + R_{k-1}^v$
  $\mathcal{S}_{k|k-1} = [\hat{s}_k^- \quad \hat{s}_k^- + \gamma\sqrt{P_{s_k}^-} \quad \hat{s}_k^- - \gamma\sqrt{P_{s_k}^-}]$
  $\dot{\mathcal{S}}_{k|k-1} = F(\hat{w}_{k-1}^+, \ \mathcal{S}_{k|k-1}, \ u(k-1))$
  $\mathcal{D}_{k|k-1} = G(\mathcal{S}_{k|k-1}, \ \dot{\mathcal{S}}_{k|k-1})$
  $\hat{d}_k^- = \sum_{i=0}^{2L} W_i^{(m)} \mathcal{D}_{i,k|k-1}$

3: Update after the measurement of $d(k)$:
  $P_{d_k}^- = \sum_{i=0}^{2L} W_i^{(c)} (\mathcal{D}_{i,k|k-1} - \hat{d}_k^-)(\mathcal{D}_{i,k|k-1} - \hat{d}_k^-)^\top + R_k^e$
  $P_{s_k d_k}^- = \sum_{i=0}^{2L} W_i^{(c)} (\mathcal{S}_{i,k|k-1} - \hat{s}_k^-)(\mathcal{D}_{i,k|k-1} - \hat{d}_k^-)^\top$
  $\mathcal{K}_k = P_{s_k d_k}^- (P_{d_k}^-)^{-1}$
  $\hat{s}_k^+ = \hat{s}_k^- + \mathcal{K}_k[d(k) - \hat{d}_k^-]$
  $P_{s_k}^+ = P_{s_k}^- - \mathcal{K}_k P_{d_k}^- \mathcal{K}_k^\top$